ABSTRACT

Title of Dissertation: Particle Attachment and Entrainment in Marine Substrates Using Numerical Modeling and Laboratory Experiments

Mahdi Khademishamami
Doctor of Philosophy, 2025

Dissertation directed by: William Nardin, Lawrence Sanford

This thesis investigates the interaction of sediment particles with flow, and marine and riverine substrates, focusing on particle attachment to emergent vegetation stems and fine sand winnowing from immobile rough substrates. Using a CFD-DEM (Computational Fluid Dynamics–Discrete Element Method) approach, it explores particle capture mechanisms within a patch of emergent vegetation, represented by cylindrical collectors, and assesses flow dynamics

and fine sand movement threshold entrapped in large immobile roughness elements such as gravel beds, or Oyster beds.

Particle attachment to a single vegetation stem was investigated in CFD-DEM model framework with varying adhesive forces on the vegetation stems formed by biofilms, and the effect of this surface energy was explored in attachment efficiency of the stem or collector (Chapter 2). The CFD-DEM model was also applied to study the suspended particle attachment to group of stems resembling a saltmarsh vegetation patch in regular and random arrangements, and the effect of density of vegetation patch (solid volume fraction of stems) on particle capture efficiency was explored (Chapter 3). Findings reveal that patch-averaged capture efficiency increases with vegetation density with part of the suspended load deposited at the rear of the collectors or stems. In chapter 4, sand entrainment from the interstices of immobile rough substrates was observed through laboratory experiments, relevant to applications like oyster bed restoration and gravel bed flushing in rivers. This work identifies hydrodynamic conditions for entrainment of fine sand, aiding in designing flow rates for habitat restoration by removing excess fine sediment.

The results of this research offer insights into designing wetlands and bioretention zones for sediment capture and maintaining habitat health in marine in riverine environments.

PARTICLE ATTACHMENT AND ENTRAINMENT IN MARINE SUBSTRATES
USING NUMERICAL MODELIGN AND LABORATORY EXPERIMENTS

by

Mahdi Khademishamami

Dissertation submitted to the Faculty of the Graduate School of the
University of Maryland, College Park, in partial fulfillment
of the requirements for the degree of
[Doctor of Philosophy]
[2025]

Advisory Committee:
Doctor William Nardin, Chair
Professor Lawrence Sanford
Professor Elizabeth North
Doctor Johan Larsson
Doctor Jacob Wenegrat

Acknowledgements

I would like to express my deepest gratitude to my advisors, Dr. William Nardin and Professor Larry Sanford, for their unwavering support, guidance, and encouragement throughout my doctoral journey. I am also deeply thankful to Professor Elizabeth North for her weekly meetings and thoughtful feedback, which greatly enriched this work. I appreciate Dr. Johan Larsson and Dr. Jacob Wenegrat for their invaluable insights as members of my thesis committee.

I sincerely thank the Horn Point Education Committee, particularly Dr. Raleigh Hood, and current and former HPL directors Professor Mike Sieracki, and Professor Mike Roman for supporting my fellowship and teaching assistantship. Special thanks to Professor Larry Sanford for the opportunity to serve as his teaching assistant. I also appreciate Amy Griffin's flexibility and encouragement during my part-time administrative role.

I extend my appreciation to the IT staff at the University of Maryland, particularly the Department of Mechanical Engineering and the Zaratan supercomputer team, for their assistance. I am grateful to Ashley Hollins, Lorie Staver, Jeff Cornwell of the Poplar Island team for accommodating field trips and very helpful discussions about saltmarsh dynamics, and also the maintenance staff at Horn Point Laboratory, for their constant support. My heartfelt thanks go to my friends Nabi Allahdadi, Iman Salehi, Limin Sun, Tesfaye Tarekegn, Navid Maroofi, Fabio Addona, and Iacopo Vona for their friendship and constant encouragement.

My journey in academia has been shaped by the guidance and support of exceptional advisors, colleagues, and friends from around the world. I am especially grateful to Professor Sandro Longo and Doctor Luca Chiapponi of the University of Parma for their mentorship during my six-month research visit, Professor Luigi Fraccarollo of Trento University, Professor Jochen Aberle of Braunschweig Institute of Technology, Professor Geraldine Wharton of Queen Mary University of London, and Mohammad Hossein Omid from the University of Tehran.

Finally, to my family, thank you for your unconditional love and belief in me. This accomplishment would not have been possible without your unwavering support.

Table of Contents

List of Tables

List of Figures

Figure 2.5 Comparison of the drag coefficient C_D from the current numerical model (open red circles) and experiments of Tritton (1959) (blue stars) and Wen et al. (2004) (blue cross), and numerical model of Henderson (1995) (red dots).

Figure 2.6. Particle capture efficiency (η, %) using CFD-DPM model (red filled circles) compared to laboratory results of Palmer et al. (2004) (empty rectangles) for particle relative sizes of 0.03, 0.015, and 0.008. The error bars are for Palmer et al. (2004) experiments.

Figure 2.7. Snapshot of final particle distribution (a, c) on the collector (20 sec of simulation time) in the DEM model with perfect attachment (left images) and total particle attachment over time (right panels) for (a, b) $Re_c = 115$, $r_p = 0.031$, $\gamma = 5\, mJ/m^2$ and (c, d) $Re_c = 149$, $r_p = 0.008$, $\gamma = 5\, mJ/m^2$. Particles are colored by their residence time from the shortest (blue) to longest (red).

Fig. 2.8. a) Total particle attachment over time in terms of number of deposited particles on the collector for Rec=115 and $r_p = 0.031$ for different dimensionless surface energy values ϕ (Table 3, experiment set 7-9) and perfect attachment (Table 2, experiment set 3). Final configuration of particles on the collector from downstream wake viewpoint are shown for ϕ =20700 (b) and ϕ =51.8 (c). Particles are colored by their residence time from the shortest (blue) to longest (red).

Figure 2.9. The variation of attachment efficiency η with respect to the perfect attachment efficiency, $\eta_{perfect}$ (Table 3, column 6) versus the dimensionless surface

collectors were fixed as 48 collectors, similar to the regular arrangement. The lateral size of each domain was 3 mm with only one cell. The mesh consisted of 750,000 Hex-dominated elements with refinement near the wall regions. The domain size containing vegetation elements changes for reaching the desire volume fraction.

Figure 3.13. The back efficiency of the collectors in the regular arrangement. The back efficiency is here defined as the total number of particles deposited in the back of collectors across the patch divided by the total number of particles captured by the collectors. Results are for different vegetation densities L=25mm (λ =0.15) , L=35mm (λ =0.075) and, L=50mm (λ =0.035).

Figure 3.14. Variation of patch capture efficiency for random arrangement of collectors for density of λ =0.15 (Orange), λ =0.075 (Yellow), and λ =0.035 (Blue) with collector Reynolds number (Re_c).

Fig. 3.15. Flow field (a), spatial variation of collector attachment efficiency represented by the contour plot of particle count on collectors (b), and time variation of particle attachment to selected collectors (c). The vegetation density is λ =0.035, and the Reynolds number is $Re_c = 279$. In plot (b), numbers indicate collector positions within the domain, while the legend in (c) corresponds to these collector numbers.

Figure 3.16. Flow field (a), spatial variation of collector attachment efficiency represented by the contour plot of particle count on collectors (b), and time variation of particle attachment to selected collectors (c). The vegetation density is λ =0.15, and the Reynolds is $Re_c = 279$. In plot (b), numbers indicate collector positions within the domain, while the legend in (c) corresponds to these collector numbers.

List of Abbreviations

$r_p = R_p/R_c$ particle relative size

R_p particle radius

R_c collector radius

$\rho^+ = \rho_p/\rho$ particle density ratio or specific density

ρ_p particle density

ρ fluid density

$Re_c = (\rho U_\infty D_c)/\mu$ collector Reynolds number

U_∞ approaching velocity in far upstream of collector

D_c collector diameter

μ fluid dynamic viscosity

$Pe = U_\infty D_c/\Gamma_p$ peclet number

Γ_p particle diffusivity coefficient

u_i local flow velocity in the i direction

p dynamic pressure

$\overline{u'_\imath u'_\jmath}$ Reynolds stress term

δ_{ij} Kronecler delta function

$\mathbf{U}_p$ particle velocity vector

$\mathbf{F}_{f\to p}$ forces from fluid on particles

$\mathbf{F}_{s\to p}$ forces exerted from wall surface on particles.

$\mathbf{F}_{p\to p}$ forces from a particle exerted on the other particles.

$\mathbf{F}_{ext}$ external forces on a particle such as gravitational forces and electromagnetic forces

I_p moment of inertia on a particle

$\mathbf{\Omega}_p$ particle rotational velocity

$\mathbf{M}_{f\to p}$ hydrodynamic through from fluid on particle

$\mathbf{M}_{s\to p}$ torque from surface on the particle.

$\mathbf{M}_{p\to p}$ the torque induced by the particle on another particle.

$\mathbf{M}_{ext}$ the torque by external forces on the particle

$\mathbf{F}_{\mathrm{drag}}$ the drag force on the particle

$\mathbf{F}_{\mathrm{lift}}$ the lift force on the particle

$\mathbf{F}_{\mathrm{added\ mass}}$ added mass force on the particle.

$\mathbf{F}_{\mathrm{Basset}}$ basset force on the particle.

C_D the drag coefficient

γ surface energy of the collector expressed in

$\phi = \gamma/\left(\rho_p {U_0}^2 R\right)$ dimensionless surface energy

$1/R = 1/r_p + 1/r_c$ dimensionless contact radius

Chapter 1: Introduction

Marine and riverine substrates are essential habitats for numerous organisms, yet they are increasingly threatened by degradation due to Sea level rise and human activities. Substrates like saltmarshes and submerged aquatic vegetation (SAV) beds provide a wide range of ecosystem services, including the generation of raw materials and food for coastal habitats, coastal protection through wave attenuation, erosion control by stabilizing the bed with root systems, water purification through nutrient uptake and suspended particle retention, support for fisheries by acting as nursery grounds, carbon sequestration, and aesthetic and recreational value (Koch, 2001; Agawin and Duarte, 2002; Barbier et al., 2011; Stratigaki et al., 2011; Donatelli et al., 2019). These roughness elements play a critical role in scalar transport within these natural environments. For example, saltmarsh stems reduce flow velocity, facilitating the deposition of suspended particles. Similarly, SAV beds create a shear layer at the interface with the overlying flow, promoting the exchange of momentum and mixing of pollutants, nutrients, and sediment particles across layers. However, these vital habitats are under increasing threat due to sea-level rise and human activities, highlighting the urgent need for conservation and restoration efforts.

Oyster beds in marine environments and large boulders in rivers are other significant roughness elements that provide valuable ecosystem services. Their interaction with the surrounding flow plays a crucial role in determining the fate of habitats that develop around them, such as spawning grounds for salmonids in gravel-bed rivers, or in supporting their own survival, as in the case of oyster beds. Different substrates have varying sediment needs to maintain their function and health. Saltmarsh platforms, for example, rely on sediment input for land accretion and countering sea level rise. Conversely, excessive sediment deposition threatens habitats like oyster beds, where oysters can be buried, and SAV beds, which may lose the light needed for photosynthesis.

This thesis investigates two key processes: the suspension dynamics and attachment of particles to emergent vegetation stems, and the entrainment of sediment particles trapped within the interstices of large immobile elements, such as oysters and large gravel particles. Suspended particle transport and attachment to vegetation stems are examined through numerical simulations, combining computational fluid dynamics (CFD) to model the flow field and the Discrete Element Model (DEM) to capture sediment particle behavior. This research is motivated by field observations indicating that vegetation stems can capture a noticeable part of suspended sediment load, a process crucial for sediment budget analysis in saltmarsh restoration efforts. Field studies suggest that vegetation can remove up to 50% of the sediment entering a saltmarsh platform (Stump, 1983), while some have estimated this to be 5-10% of the total suspended load (Li and Yang, 2009).

In the two chapters of this thesis, the applicability of CFD-DEM techniques for quantifying suspended sediment capture is addressed, along with an evaluation of the advantages of this approach over previous models and the influence of vegetation spacing and configuration. Also, Laboratory experiments are reported to address the entrainment of sand particles from the interstices of large, immobile elements.

The chapters of the thesis are organized as follows:

Chapter 2 focuses on the numerical modeling of suspension dynamics and particle attachment to a single saltmarsh stem, represented by a cylindrical vegetation model. This model combines computational fluid dynamics (CFD) with a discrete element model (DEM), incorporating adhesive forces on the stem surface. The chapter begins by applying an Eulerian-Lagrangian approach, using Reynolds-averaged Navier-Stokes (RANS) equations to quantify the attachment efficiency of a cylindrical collector under a "perfect attachment" condition, where particles are assumed to attach upon first collision with the collector. Subsequently, the assumption of perfect attachment is lifted, allowing the collector surface to exhibit varying degrees of adhesion. Here, the DEM model employs the Johnson-Kendall-Roberts (JKR) approach to simulate the effects of adhesive forces on particle attachment.

Chapter 3 extends the CFD-DEM technique used in chapter 2 from a single collector to a group of collectors, simulating a patch of saltmarsh stems. This approach recognizes that saltmarsh vegetation typically grows in groups, where interactions among stems, as well as their spacing and density, can significantly influence particle attachment dynamics—an effect noted in the experimental work of Purich (2006). Numerical modeling was conducted for two stem arrangements, regular and random distributions—and three vegetation densities: low, intermediate, and high. The results are presented in terms of patch-averaged attachment efficiency, providing insights into how stem arrangement and planting density affect the capture efficiency of suspended particles within a patch of vegetation.

Chapter 4 investigates a threshold criterion for the mobilization of sand particles entrapped within the interstices of larger, immobile roughness elements through laboratory experiments. These roughness elements can be analogous to oyster beds, or gravel beds in rivers, where excessive sedimentation may impede restoration efforts. Establishing a criterion for the flow conditions required to entrain these particles is crucial for designing restoration sites with hydrodynamically favorable conditions. Additionally, the findings contribute to the design of flushing flows in gravel-bed rivers, aiding in the removal of sediment from spawning grounds to protect salmonid embryos.

Chapter 5 summarizes the findings from the previous chapters and explores their practical applications, particularly in the restoration of saltmarsh ecosystems and the quantification of the suspended load captured by vegetation stems. This chapter discusses the potential of CFD-DEM techniques to be extended to various scenarios commonly encountered in marine environments, including the effects of waves, stratification, salinity, vegetation stem flexibility, grain size distribution, and particle shape. Additionally, insights are provided into applying CFD-DEM methods to quantify fine sand entrainment from large roughness elements, as well as the potential for developing reduced-order models based on the CFD-DEM methodology.

Chapter 2: Direct interception of particles by a vegetation stem with varying adhesive forces

Abstract

The direct interception of particles by vegetation stems has been reported in field studies of saltmarsh platforms as a major cause for removing suspended particles and pollutants. Laboratory observations and numerical models reported in the literature have computed the attachment efficiency under the assumption that particles stick and do not move when they collide with the surface of the collector (i.e., perfect attachment). This study was aimed at lifting this assumption using a Discrete Element Model (DEM) with varying adhesive contact forces coupled with Computational Fluid Dynamics (CFD). The CFD-DEM model considers the stickiness of the collector through a surface energy parameter. Model predictions showed good agreement with laboratory observations. The final configuration of particles on the collector's surface and the attachment efficiency changed when the collector's surface energy varied. The attachment efficiency could be twice that under the perfect attachment assumption, indicating that modeling studies with perfect attachment may underestimate suspended particle removal. As biofilms are considered the main cause of the adhesiveness of stems, our study shows that any

biofilm formation that could create a surface energy as low as 0.01 mJ/m^2 could lead to attachment of particles on a single saltmarsh stem.

Introduction

Saltmarshes are recognized for their invaluable ecosystem services. Benefits of these ecosystem engineers include: protection of coastline through attenuation of waves (Morris et al., 2018) and controlling of erosion by stabilizing bed through their roots (Donatelli et al., 2019), generating raw materials and food for coastal habitats, purifying water through uptake of nutrients and retention of suspended particles, maintaining fisheries by providing nursery grounds, carbon sequestration, and providing aesthetic experiences for tourism and recreation (Barbier et al., 2011) . Human activities have put saltmarshes under threat leading to a 50 percent reduction around the world (Barbier et al., 2011). Sea level rise is also predicted to result in more than a 60 percent loss of saltmarshes areal coverage soon (Giuliani and Belluci, 2019). Therefore, saltmarshes are the subject of numerous restoration efforts because of their critical role in maintaining coastal ecosystems.

Understanding of the role of vegetation in sediment trapping is important for restoration of salt marshes. A successful design of a restoration project for saltmarshes requires an estimate of the sediment budget because the vertical accretion of the saltmarsh platform should outpace the sea level rise for a successful restoration plan (Fagharezzi et al., 2020). Salt marshes are also very useful for removing pollutants entering from the land to ocean via their sediment trapping ability. Sediment particles entering a marsh can contain between 20 and 43 percent of the total

Phosphorous and as much as 12 percent of the total Nitrogen (Noe and Harvey 2007). As a buffer zone, saltmarshes can trap these contaminants carrying particles by reducing the flow velocity by increasing the roughness (Elliot, 2000). This research contributes to our understanding of the role of saltmarsh in trapping suspended sediment particles.

The flow hydrodynamics, associated dispersal of pollutants, and vegetation species change from the edge to the interior of the salt marsh. While gravitational settling towards the bed is a major process of sedimentation in saltmarsh platform, the stems and leaves of saltmarsh species also increase the surface area available for the settling of suspended particles (Elliot, 2000). In Delaware Bay, 50% of the total loss of the sediment was shown to be attributed to direct capture by the leaves and shoots of *Spartina alterniflora* vegetation over several consecutive tidal cycles (Stump, 1983). In the Yangtze River delta in China, the contribution of direct capturing by plants to the total sedimentation could be estimated to amount more than 10 percent for *S. alterniflora*, less than 10 percent for *S. mariquter*, and less or more than 10 percent for P. australis (Li and Yang 2009). Li and Yang (2009) found three significant factors that influence adherence: suspended sediment concentration (SSC), which becomes essential in forming sediment clumps and sediment availability; platform elevation, which determines the frequency of flooding into the body of saltmarsh; and properties of the species such as vegetation biomass.

The exact quantification of the attachment efficiency of particles to saltmarsh stems due to direct interception is not possible in the field due to uncertainties about the availability of measurement instruments, deployment of the instruments, numerous flow variables that are hard to control, sediment size gradation and content, etc. Instead, laboratory and modeling experiments have been used to identify the flow, particle, and stem shape variables that influence attachment efficiency in a controlled environment (e.g., Palmer et al., 2004; Purich, 2006; and Fauria et al., 2015).

Considering a saltmarsh stem as a cylinder, various flow and shape variables have been identified that influence the fraction of suspended particles that impact and attach to the cylinder or “collector". As shown in Figure 2.1, particles in a flow stream approach the collector and, depending on the characteristics of the flow, sediment, and collector shape, the particles either follow the streamlines to find contact with the collector and attach there (direct interception) or deviate from streamlines and impact directly to the collector due to excessive momentum (inertial impaction). The particle attachment efficiency η, i.e., the number of particles intercepted by the collector divided by the total number of the particles released from a window of width equal to the diameter of the collector have been shown to be dependent on some dimensionless variables such as particle size ratio $r_p = R_p/R_c$, particle density ratio $\rho^+ = \rho_p/\rho$, Collector Reynolds number $Re_c = (\rho U_\infty D_c)/\mu$, and Peclet number $Pe = U_\infty D_c/\Gamma_p$, where R_p is the particle radius, R_c is the collector radius, ρ_p is the particle density, ρ is the fluid density, U_∞ is the approaching flow velocity far upstream of the collector, D_c is the diameter of the collector, and Γ_p is the diffusivity of the particles (Palmer et al., 2004).

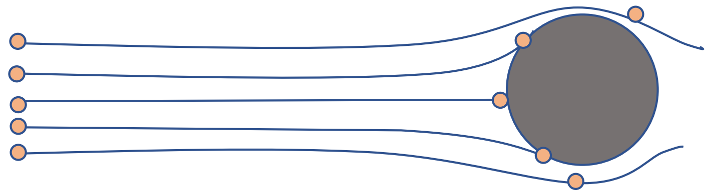

Figure 2.1 The schematic of a collector as an idealized stem (dark gray circle) and direct interception of particles (orange circles) on the collector surface (after Palmer et al. 2004).

The flow hydrodynamics around a cylindrical collector in an infinite domain is mainly determined by the collector Reynolds number $Re_c = (\rho U_\infty D_c)/\mu$. The flow regimes can be categorized as (Sumer and Fredsoe, 2006):

- For $Re_c < 5$ there is a creeping flow over the collector with no separation of the boundary layer.
- For $5 < Re_c < 40$ there is a fixed pair of symmetric vortices behind the cylinder.
- For $40 < Re_c < 200$ is the vortex shedding regime. The wake becomes unstable around $Re_c = 40$. The vortices are two dimensional. The vortex street is completely laminar in this case.
- For $200 < Re_c < 300$ the vortex street is in a transition to turbulence in the wake of the cylinder. The vortices are distinctly three dimensional in this range.
- For $300 < Re_c < 3 \times 10^5$ the wake becomes completely turbulent. However, the boundary layer on the cylinder remains laminar.

The collector Reynolds number in aquatic saltmarsh environment is usually up to 1000, and this range of Reynolds numbers has been the focus of study on particle attachment on a single cylinder in aquatic environments. Palmer et al. (2004) studied the capture efficiency of a single collector through laboratory experiments in a water flume with focus on particle attachment on saltmarsh stems. Their experiments were in the range of collector Reynolds number of $Re_c = 50 - 500$. Particle capture efficiency for three relative particle sizes $r_p = 0.008, 0.015, 0.031$ and one specific density ρ^+ of 1.03 were measured in their experiment for multiple Re_c values. Greasing the surface of the collector, they assumed that particles remained attached once they encountered the surface of the collector (perfect attachment assumption). Their experiments showed that particle capture efficiency increased with both collector Reynolds number Re_c, and particle size ratio $r_p = R_p/R_c$ expressing with:

$$\eta = 0.224(Re_c)^{0.718}{r_p}^{2.08} \tag{2.1}$$

in which Re_c is the collector Reynolds number, and r_p is the particle relative size i.e., diameter of the particle divided by the diameter of the collector. Equation 2.1, obtained by regression analysis for the range of Reynolds numbers tested shows the pronounced effect of the relative size as being more influencing factor than the collector Reynolds number. Also, it shows the positive correlation of the attachment efficiency with both collector Reynolds number and particle relative size.

Haugen and Kragset (2010) used direct numerical simulation to study the capture efficiency as a function of collector Reynolds number and Stokes number. The Stokes number St is defined as the ratio of particle relaxation time $\hat{\tau}_p = \rho^+ D_p^2/18\nu$ to a fluid time scale $\hat{\tau}_f = D_c/2U_\infty$ where

D_p is the particle diameter (Haugen and Kragset, 2010; Michaleides, et al. 2023). For $St \ll 1$, the particle has enough time to respond to changes in fluid velocity and follow the streamlines, but for $St \gg 1$ the particles deviate from the streamlines due to their additional inertia relative to the flow (Michaelides, et al. 2023). The results of Haugen and Kragset (2010) also showed that for $St < 0.1$, the main mechanism of capturing was through direct interaction with the boundary while for $St > 0.1$ the main mechanism was inertial impaction. There was also an intermediate regime in which there was a steep increase in capture efficiency with Stokes number. In all regimes, there was a continuous increase of capture efficiency as Stokes number increased.

Using direct numerical simulation (DNS), Spinosa et al. (2012, 2013) extended studies of Palmer et al. (2004) up to $Re_c = 1000$ in aquatic environments with very small particle Stokes number. They also assumed that particle would remain on the surface of the collector upon first contact, namely perfect attachment assumption. Their results showed a great similarity with data of Palmer et al. (2004) and confirmed that capture efficiency is directly correlated with collector Reynolds number, and particle relative size as observed by Palmer et al. (2004).

The investigations presented by Palmer et al. (2004), Haugen and Kragset (2010), and Spinosa et al. (2012,2013) delineate important features of particle attachment to a single cylindrical collector that could be used for sediment transport budget analysis of saltmarsh environment. However, the assumption of perfect attachment might not always be valid in the natural environment, and these assumptions must be tackled using a sediment transport perspective. The numerical model of Spinosa et al. (2012,2013) was based on calculating capture efficiency based on limiting streamlines around the collector, and part of their model that used particles was based on considering particles as point masses rather than finite size particles. This paper utilizes computational fluid dynamics (CFD) coupled with Discrete Element Model (CFD) with inclusion of adhesive forces on the cylinder and contact forces resulting from collision of particles with the collector surface to study the particle attachment efficiency in a more systematic way.

The most notable study using the CFD-DEM technique to study micron size particles on very thin fibers was conducted by Li and Marshal (2007) in aerosol industry. Their study therefore was for very low collector Reynolds number on the order of one, and for inertial impaction phenomenon (large Stokes number). Besides Stokes number, they introduced an adhesion parameter for colloidal particles $\phi = \gamma / \rho_p U_0^2 R^*$ where γ is the surface energy of the collector, ρ_p is the mass density of the particle, U_0 is the incoming velocity far upstream of the collector, and R^* is an effective radius whose inverse is calculated as the sum of reciprocal of radius of the two surfaces in contact. Their numerical model which was limited to collector Reynolds number of around one ($Re_c = 1$) and in the absence of turbulence, revealed interesting features of particle deposition and erosion of particles at the order of 1 micron. Their numerical model showed the extent of deposition on the surface of the collector was dependent on shear stress distribution on the collector and formation of a "shadow region" behind which incoming particles could not deposit. After formation of the first layer, the incoming particles were attached to already deposited particles at the same area forming a "chain deposition". The chain deposition led to the formation of larger shadow regions and formation of aggregates or “dendrites” at the front position. The size of this dendrite structure was regulated by consecutive formation and breakage by the flow hydrodynamics.

Although these investigations significantly advanced our knowledge regarding the particle attachment to a single collector, the factors that affect attachment without the assumption of perfect attachment, and in the presence of turbulence and higher collector Reynolds numbers still need to be investigated in aquatic environments. In this research, we aim to investigate the particle attachment to a cylindrical stem vegetation using computational fluid dynamics (CFD) combined with a discrete element model (DEM) for tracking of the particles. The current work extends the research of Li and Marshal (2007) to aquatic environments where a collector Reynolds number is large enough that vortex shedding forms behind the collector and effect of flow turbulence cannot be ignored in bringing the particles to the near surface of the collector. First, the Eulerian-Lagrangian framework is elucidated in terms of equations of the continuum flow field and forces on individual particles. Second, the applicability of the two versions of the Eulerian-Lagrangian model is tested for calculation of the particle attachment efficiency with perfect attachment assumption. These two models are named Discrete Phase Model (DPM) in which particles are assumed as point masses and particle-particle and particle-collector interactions are neglected. The second Eulerian-Lagrangian model is the Discrete Element Model (DEM) which implements particle-particle and particle-collector contact forces, and adhesive forces on the collector through Johnson-Kendall-Robert (1971) (JKR) theory. Finally, the DEM model is used as the main framework to consider the effect of stickiness of the collector in modulation of attachment efficiency and particle dynamics on the surface of collector.

Methods and Materials

The framework for the numerical model here is an Eulerian-Lagrangian method which both CFD-DPM and CFD-DEM are based on. The Eulerian flow field is solved using Reynolds Averaged Navier Stokes (RANS):

$$\frac{\partial \rho}{\partial t} + \frac{\partial}{\partial x_i}(\rho u_i) = 0 \tag{2.2}$$

$$\frac{\partial}{\partial t}(\rho u_i) + \frac{\partial}{\partial x_j}(\rho u_i u_j) = -\frac{\partial p}{\partial x_i} + \frac{\partial}{\partial x_j}\left[\mu\left(\frac{\partial u_i}{\partial x_j} + \frac{\partial u_j}{\partial x_i} - \frac{2}{3}\delta_{ij}\frac{\partial u_l}{\partial x_l}\right)\right] + \frac{\partial}{\partial x_j}\left(-\rho\overline{u'_i u'_j}\right) \tag{2.3}$$

where ρ is fluid density, u is the local flow velocity, p is the dynamic pressure, δ_{ij} is the Kronecker delta, $\overline{u'_i u'_j}$ is the Reynolds stress term which must be modeled and appears after time averaging of the instantaneous Navier Stokes equations. Hence, closure equations will be needed to model the turbulence. Several models have been developed for such a purpose. In two equation turbulence models including $k - \omega\ SST$ model which have been used here, the Boussinesq hypothesis relates the Reynolds stress term to velocity gradient through (Ansys21.2):

$$-\rho\overline{u'_i u'_j} = \mu_t\left(\frac{\partial u_i}{\partial x_j} + \frac{\partial u_j}{\partial x_i}\right) - \frac{2}{3}\left(\rho k + \mu_t\frac{\partial u_l}{\partial x_l}\right)\delta_{ij} \tag{2.4}$$

Figure 2.2 shows the computational domain, and the mesh used here. A 2D domain was used here for the CFD-DPM model. The structured mesh was created using ICEM-CFD software using a multiblock and O-grid approach. CFD-DEM technique needs a three-dimensional domain, therefore the 2D mesh was extended in the lateral direction to create the 3D mesh and geometry. A single cylinder with a fixed diameter of 10mm was inserted in the domain. The lateral boundaries (upper and lower in the figure) were selected far enough from the cylinder to avoid their disturbance on the flow in the vicinity of the cylinder. The inlet and outlet boundaries (left and right in the figure) were put far aside for a uniform entrance flow on the left and a minimum returning flow on the right or exit boundary.

The numerical experiments were conducted using mainly the same variables as in experiments of Palmer et al. (2004). Three particle size ratios r_p equal to 0.008, 0.015, and 0.03 for various collector Reynolds numbers Re_c between 38 and 486 were used to validate the numerical model. The particle specific density $\rho^+ = \rho_p/\rho$ of 1.03 was also used here like that used in experiments of Palmer et al. (2004). Velocity profile measurements by Neumeier and Ciavola (2004) in a saltmarsh of *Spartina maritima* species showed a maximum velocity of 5 cm/s which justifies the chosen Reynolds number range of current numerical model and experiments of Palmer et al. (2004). Measuring suspended sediments in natural systems, such as estuaries and rivers, typically range from clay (less than 0.06 mm) to fine sand (up to 0.5 mm) which encompasses the selected size of the particles chosen. The particle sizes are also in the range typical for microplastics which are defined as particles less than 5mm in size (McIlwraight et al., 2024). Inorganic mineral sediments typically have density of 2600, but they are enriched with organic contents found as flocs (Droppo, 2001), which can lead to a reduced density. Microplastics also typically have a density in the range of 900 kg/m^3 to 1500 kg/m^3 (McIlwraight et al., 2024). The Stokes number St value lies within range of 0.001 to 0.003 which ensures direct interception as the predominant mechanism of attachment of the particles on the collector.

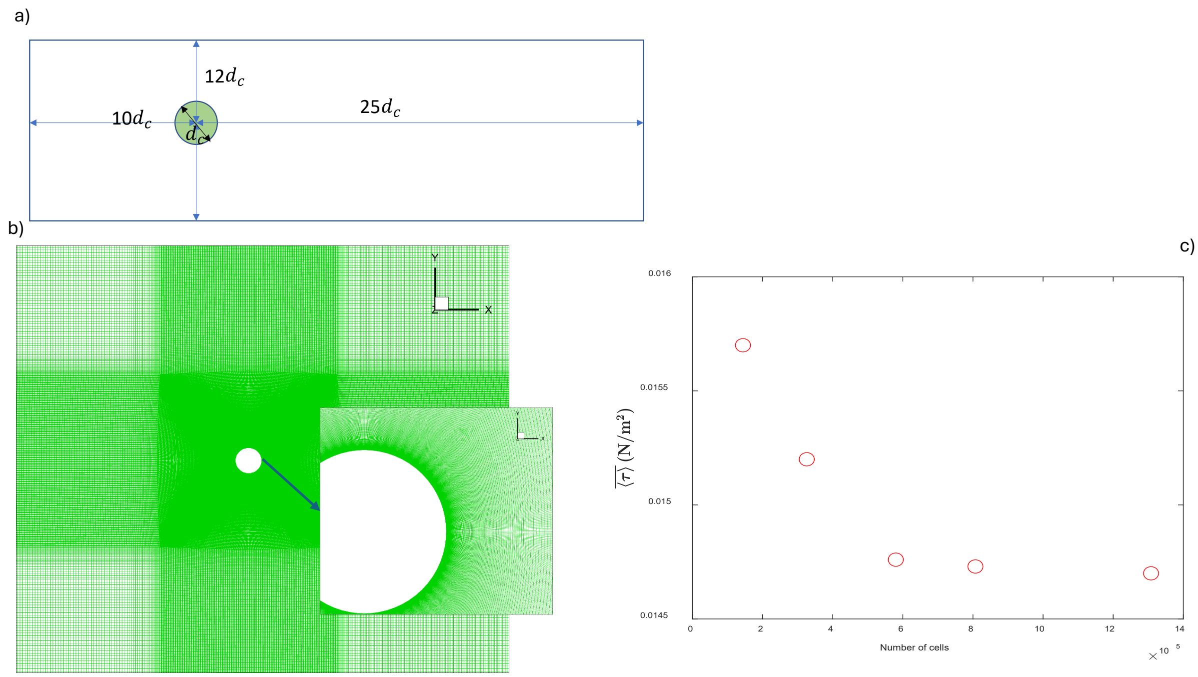

Fig 2.2 (a) The 2D computational domain with dimensions in terms of collector diameter d_c and (b) The 2D structured mesh used in the CFD-DPM approach with an O-grid refinement block around the cylinder, and c) the variation of time and area-averaged shear stress on the cylinder with number of computational cells for $Re_c = 149$. The same mesh was extended 2.4 mm spanwise with one cell in the lateral direction to be used at 3D model of CFD-DEM.

A mesh sensitivity analysis was performed to determine an optimum number of cells in the domain for preserving the solution accuracy while reducing the computational cost. Four mesh sizes of approximately 144,000, 326,000, 580,000, 807,000, and 1,308,000 cells were examined for this purpose, and the shear stress was averaged in time and over the surface of the cylinder for an intermediate Reynolds number of $Re_c = 149$. As shown in Figure 2.2c, it was concluded that refining the mesh above 580000 cells did not change the estimation of shear stress significantly. Therefore, the computations were all performed with 580,000 cells in the domain.

A full lagrangian model in a turbulent wall bounded flow should consider the forces exerted by the fluid, other particles, any surface in the solution domain the particle may get into contact with, and external forces due to gravitation or magnetic fields. The effect of different parameters can be described using classical mechanics for particle trajectory using the balance of forces and moments on particles in a carrying fluid (Henry et al., 2014):

$$\frac{d\mathbf{x}_p}{dt} = \mathbf{U}_p \tag{2.5}$$

$$m_p \frac{d\mathbf{U}_p}{dt} = \mathbf{F}_{f\to p} + \mathbf{F}_{s\to p} + \mathbf{F}_{p\to p} + \mathbf{F}_{ext} \tag{2.6}$$

$$I_p \frac{d\mathbf{\Omega}_p}{dt} = \mathbf{M}_{f\to p} + \mathbf{M}_{s\to p} + \mathbf{M}_{p\to p} + \mathbf{M}_{ext} \tag{2.7}$$

$\mathbf{x}_p$ is the particle position, $\mathbf{U}_p$ the particle translational velocity, $\mathbf{\Omega}_p$ particle rotational velocity, m_p its mass, I_p its moment of inertia, $\mathbf{F}_{f\to p}$ and $\mathbf{M}_{f\to p}$ are the hydrodynamic forces and torques acting on the particle, $\mathbf{F}_{s\to p}$ and $\mathbf{M}_{s\to p}$ are forces and torques exerted by surfaces, $\mathbf{F}_{p\to p}$ and $\mathbf{M}_{p\to p}$ are forces and torques resulting from particle-particle interactions, and $\mathbf{F}_{ext}$ and $\mathbf{M}_{ext}$ are the external forces and torques due to for example magnetic fields. Fluid-particle forces $\mathbf{F}_{f\to p}$ include drag, lift, added mass, Basset force, and Brownian force (Henry et al., 2014):

$$\mathbf{F}_{f\to p} = \mathbf{F}_{\text{drag}} + \mathbf{F}_{\text{lift}} + \mathbf{F}_{\text{added mass}} + \mathbf{F}_{\text{Basset}} + \text{Brownian} \tag{2.8}$$

CFD-DPM model setup

The DPM model used here is a built-in multiphase flow model in Ansys Fluent that applies balance of forces on individual particles using equations (2.5) to (2.7) except that the forces and torques are only from fluid exerted on particles i.e. only $\mathbf{F}_{f\to p}$ and $\mathbf{M}_{f\to p}$ are included. The particles can interact with the continuous phase in two ways. In the first approach, the particles are only influenced by the fluid flow but not vice versa (one-way coupling). In the second approach, both particles and fluid flow affect each other (Two-way coupling). The first approach can be utilized when the concentration of particles is low in the solution domain, typically less than 10 percent occupying a grid cell (Michaelides et al., 2022). On the other hand, a two-way coupling approach can be used when the concentration of the second phase or the lagrangian phase is large enough that it impacts the flow momentum through a sink term (Michaelides et al., 2022). A Two-way coupling approach of DPM model has been used here to ensure that the accumulation of the particles near the collector could be considered on dynamics of flow in that close region.

The effect of turbulence on dispersion of particles in the DPM model was calculated by a discrete random walk model (Ansys Fluent, 2021). In this model, instantaneous fluid velocity seen by the particle is decomposed into a time-averaged plus a fluctuating velocity component. In the discrete random walk (DRW) model, the fluctuating velocity components are discrete piecewise constant functions of time (Ansys Fluent, 2021). Their random value is kept constant over an interval of time given by the characteristic lifetime of the eddies.

As mentioned before, the particles in the DPM model of Ansys Fluent are considered as point masses. There are some pros and cons regarding selection of this model to find the capture efficiency of particles on a collector. The main advantage is that neglecting the interaction of particles with each other can save computational time. In suspension flow when particles in the flow domain do not interact together due to low particles loading, the time step for integration of equation can be large at the order of time step size for the simulation of the flow field. This can also help with releasing large numbers of particles to get statistically meaningful results. Neglecting the finite radius of the particles prevents the correct identification of particles that collide with the surface of the collector though. A particle in a typical lagrangian simulation is considered attached when its center lies within a radius of the particle from the collector surface (Figure 2.3). However, in the DPM mode of Fluent, a particle is assumed trapped when its center coincides with the surface of the collector which gives incorrect results regarding calculation of capture efficiency of particles. Hence, in the DPM model used here, the particle positions were recorded during the simulation in a close region around the collector, and then imported into a MATLAB program. The MATLAB code identified the particles as attached when they reside a distance equal to or less that $R_p + R_c$ from the collector center (R_p is the particle radius and R_c is the collector radius) (Figure 2.3). Hence, using the DPM model, the perfect attachment assumption can be valid, and the results could be compared with the experiments in the literature to observe the sufficiency of the CFD-DPM model for a perfect attachment scenario or “capture efficiency” calculation.

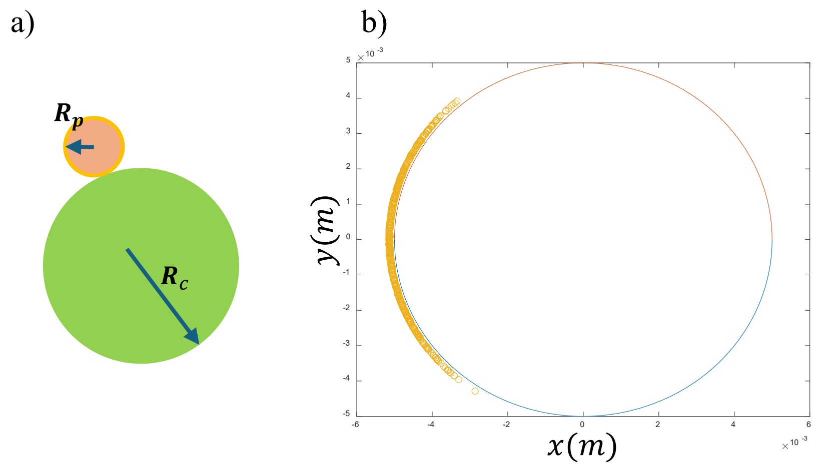

Figure 2.3. (a) A schematic of the particle attachment criteria used in the current CFD-DPM model where the particle is considered attached when the distance between center of the particle and center of collector is equal to the radius of the particle (R_p) plus the radius of the collector (R_c). (b) particles intercepted in front of the collector because of perfect attachment assumption in the CFD-DPM model.

The particles were injected from a plane 40 mm upstream of the collector, The flow was initialized from rest. Starting an unsteady solution, flow got established, and then the particles were injected into the domain from an upstream window with a width equal to the width of the cylinder diameter. The injection rate of the particles was selected such as for each experiment 90,000-150,000 particles were released in the domain. and the perfect attachment efficiency was calculated as the number of particles captured by collector with their first contact divided by the total number of particles released from the upstream window. In the framework of CFD-DPM, the capture efficiency is functionally described as

$$\eta = f\left(\frac{\rho_p}{\rho}, Re_c, \frac{R_p}{R_c}\right) \qquad (2.9)$$

Totally, nine numerical experiments were performed which encompass all the experimental results of Palmer et al. (2004) for a smooth cylindrical surface.

CFD_DEM model setup

The Discrete element model (DEM) is more comprehensive than the DPM model, and the second and third terms in equations 2.6 and 2.7 resulting from particle-collector and particle-particle interactions can be directly involved in the simulations. To implement the CFD-DEM method, the CFD model from Ansys Fluent was coupled with the DEM model of Ansys Rocky.

Particle surface forces $\mathbf{F}_{s\to p}$ are related to the interaction between two bodies in contact. Two approaches have been used in the literature to include the effect of adhesive forces in contact forces (Henry, 2017): those based on van der Waals attractive forces named adhesion mechanics approaches such as Hamaker approach, and those based on contact mechanics theories such as Johnson-Kendall-Robert (1971) theory, abbreviated as JKR theory. The JKR model which is used here has been implemented in aerosol industry by Marshall and Li (2007) for attachment of particles on a fiber as mentioned in previous sections and has been recently used by Yu et al. (2022) to study the flocculation of cohesive sediment particles in a turbulent water flow using Direct Numerical Simulation (DNS).

The attractive van der Waals forces in the JKR model is represented by a surface potential energy γ which equals half the energy per unit area needed to separate two particles from in contact to infinity (Marshall and Li, 2007) and can be related to Hamaker adhesion through (Marshall and Li, 2007)

$$\gamma = \frac{1}{2}\int_{\delta}^{\infty} \frac{A}{6\pi h^3}\, dh = \frac{A}{24\pi {\delta_m}^2} \tag{2.10}$$

where A is the effective Hamaker constant, and δ_m is characteristic minimum seperation distance of the two particle surfaces in contact region which is estimated by $\delta_m \approx \left(\mu U_0 {d_p}^{3/2}/2\pi E^*\right)^{2/5}$ (Marshall and Li, 2007).

The properties of two contacting particles such as radius, modulus of elasticity, and mass are expressed as their corresponding effective values to be used in the DEM modeling framework (Marshall and Li, 2007):

$$\frac{1}{E^*} = \frac{1-{\nu_{p1}}^2}{E_{p1}} + \frac{1-{\nu_{p2}}^2}{E_{p2}} \tag{2.11}$$

$$\frac{1}{R^*} = \begin{cases} \frac{1}{R_{p1}} + \frac{1}{R_{p2}} & \text{for particle particle collision} \\ \frac{1}{R_p} & \text{for particle boundary collision} \end{cases} \tag{2.12}$$

$$\frac{1}{m^*} = \begin{cases} \frac{1}{m_{p1}} + \frac{1}{m_{p2}} & \text{for particle particle collision} \\ \frac{2}{m_p} & \text{for particle boundary collision} \end{cases} \tag{2.13}$$

In these formulas, E^* are effective modulus of elasticity, E_{p1} and E_{p2} are Young modulus of the two particles in contact, m_{p1} and m_{p2} are masses of two contacting particles, m_p is the mass of particle contacting boundary, R_{p1} and R_{p2} are radiuses of two contacting particles, R_p is the radius of the particle contacting the boundary, and ν_{p1} and ν_{p2} are Poisson rations.

The normal and tangential contact force components act on a contact plane. A contact plane is a plane perpendicular to the line connecting centers of two particles, or a line connecting center of particle and closest point on a triangle making the boundary of a wall (Ansys Rocky, 2023). Here, a Hertzian Spring Dashpot model was used for calculation of the normal force component, $\boldsymbol{F}_n$ with an extra term due to the JKR model for inclusion of adhesion (Ansys Rocky, 2023):

$$F_n = \widehat{K}_H {s_n}^{3/2} + \hat{C}_H {s_n}^{1/4} \dot{s}_n + \sqrt{8\pi\gamma E^* a^3} \tag{2.14}$$

In which $\widehat{K}_H$ is the stiffness coefficient defined as $\widehat{K}_H = \frac{4}{3} E^* \sqrt{R^*}$, $\hat{C}_H$ is a damping coefficient which is related to stiff coefficient via $\hat{C}_H = 2\eta_H \sqrt{m^* \widehat{K}_H}$, $s_n = \frac{a^2}{R^*} - \left(\frac{2\pi\gamma a}{E^*}\right)^{1/2}$ is the normal overlap distance between two particles after deformation, and $\dot{s}_n$ is the time rate of overlap distance. In the expressions for $\hat{C}_H$ and s_n, η_H is the damping ratio in hertzian spring dashpot model that is evaluated as a function of coefficient of restitution ϵ of particles, and a is the contact radius between the particle-particle or particle-wall respectively.

The tangential component of the contact force $\boldsymbol{F}_t$ was calculated using linear Spring Columb limit model. The tangential force is considered elastic and its value at time t is linearly related to its value at previous time step with (Ansys Rocky, 2023)

$$F_{\tau,e}^{t} = F_{\tau}^{t-\Delta t} - K_{\tau}\Delta s_{\tau} \tag{2.15}$$

where $F_{\tau,e}^{t}$ is value of the tangential force at time $t - \Delta t$, Δs_{τ} is the tangential relative displacement of the particle during the time step, and K_{τ} is the tangential stiffness which is related to loading normal stiffness through (Ansys Rocky, 2023).

$$K_{\tau} = r_K K_{nl} \qquad \frac{1}{K_{nl}} = \begin{cases} \frac{1}{K_{nl,p_1}} + \frac{1}{K_{nl,p_2}} & \text{for particle particle collision} \\ \frac{1}{K_{nl,p}} + \frac{1}{K_{nl,b}} & \text{for particle boundary collision} \end{cases}$$

(2.16)

Where r_K is a user defined constant, $K_{nl,p} = E_p d_p$, and $K_{nl,b} = E_b d_p$. Here, E_p and E_b are bulk modulus of elasticity of the particle and boundary respectively.

The time step for integration of the particles in the DEM model was usually on the order of $10^{-6} - 10^{-7}s$. The attachment efficiency in the CFD-DEM framework can be described as

$$\eta = f\left(\frac{\rho_p}{\rho}, Re_c, \frac{R_p}{R_c}, \gamma/\left(\rho_p {U_0}^2 R^*\right), E/\left(\rho_p {U_0}^2\right)\right) \tag{2.17}$$

For CFD-DEM simulations, three surface energy parameters $\phi = \gamma/(\rho_p {U_0}^2 R^*)$ were selected with the same nine variables of the CFD-DPM model (totally 27 experiments). The three ϕ values were equal to 51.8, 21800, and 51800. These three values were selected based on a preliminary test for the finest particle $r_p = 0.008$ in a flow with the highest Reynolds number i.e. $Re_c = 486$. The highest value of $\phi = 51800$ corresponded to a perfect attachment experiment where the particles remained in their place upon first contact. The lowest value of $\phi = 52$ eroded a high percentage of the particles in the same experiment. An intermediate value of ϕ was also used to study the behavior of particles on the collector and to observe how reduction of surface energy changes the attachment efficiency for such average values of surface energy.

A one-way coupling approach was used in the CFD-DEM model here i.e. it was assumed that only flow field affected the particle motion, and any effect from particles on flow momentum was neglected. After extending the mesh in the lateral direction, the flow field was calculated and after being established, the unsteady flow field in the entire domain was recorded in 0.02s intervals to be used by the Ansys Rocky DEM software. A discrete random walk model was used here again to consider the effect of turbulence on dispersion of particles.

Results and Discussion

Fluid flow verification

Before exploring the attachment efficiency of particles, hydrodynamic flow field from the numerical model was verified with the drag coefficient on a single cylinder in an infinite environment. All the experiments performed here were in the range of vortex shedding regime except at Re_c = 38. Hence, it was expected that there would only be a single wake at the rear of the cylinder when Re_c = 38, as was seen in model predictions (Fig. 2.4a). However, for Re_c > 38, vortex shedding was visible, as seen in Fig. 2.4b (Figure 2.4b for Re_c = 137).

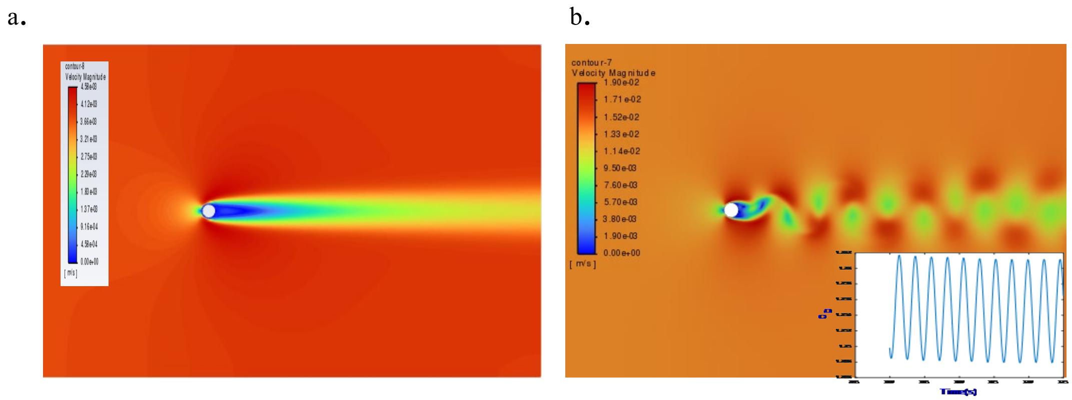

Fig. 2.4. Model predictions of fluid flow showing the wake pattern at two different Reynolds numbers a) $Re_c = 38$ and b) $Re_c = 137$. The fluctuations in the drag coefficient for the latter Reynolds number are also shown in the right inset of panel b.

Model predictions of the drag coefficient for a single cylinder from the numerical simulation were compared with laboratory measurements of Tritton (1957) and Wen et al. (2004) (Table 2.1, Fig. 2.5) and numerical results of Henderson (1995) (Fig. 2.5). Tritton's experiments were in in low Reynolds number ranges between 3 and 115, and Wen et al. (2004) did measurements up to Reynolds number of 1000. The predicted drag coefficients compared favorably with laboratory experiments at all simulated Reynolds numbers, except for $Re_c = 279$ which agreed with numerical modeling results of Henderson (1995).

Table 2.1- Drag coefficient C_D results from the 2D model and experiments of Tritton (1959) and Wen et al. (2004)

Re_c	C_D(Tritton, 1959)	C_D(Wen et al. 2004)	C_D(Current model)
38.5	1.69		1.61
35.0		1.60	1.67
76.0	1.27		1.32
115.0	1.24		1.25
149.0		1.37	1.34

CFD-DPM and perfect attachment efficiency results

The 2D numerical results from the CFD-DPM model with perfect attachment efficiency were compared with experimental results of Palmer et al. (2004) to determine the viability of the current Eulerian Lagrangian model in predicting the particle direct interception on a single collector. Palmer et al. (2004) performed laboratory flume experiments with a cylinder as a collector. They used a fixed particle size of 0.194 mm and varied the diameter of the collector. The experiments were performed for Reynolds numbers between 38 and 486. In eight out of nine cases, model predictions were within the confidence interval of the laboratory data, except for $Re_c = 38$ which overpredicted the laboratory observation (Fig. 2.6). Like laboratory data of Palmer et al. (2004), the CFD-DPM model showed an increase of the capture efficiency with Reynolds number for all tested particle sizes.

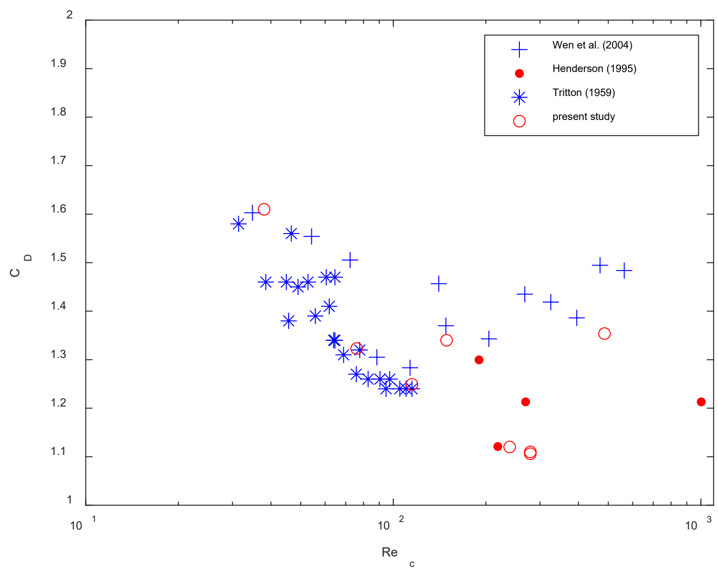

Fig. 2.5. Comparison of the drag coefficient C_D from the current numerical model (open red circles) and experiments of Tritton (1959) (blue stars) and Wen et al. (2004) (blue cross), and numerical model of Henderson (1995) (red dots).

CFD DEM results with collector stickiness

Although the results from the DPM model predict the capture efficiency with perfect attachment assumption satisfactorily, the DEM model with inclusion of collector stickiness as adhesive forces gives a more realistic viewpoint due to mechanistic analysis of the problem. Furthermore, forces from collision of particle to other particles and collector surface are considered as well. The main hypothesis driving this research is that the surface energy of the collector affects the attachment efficiency of the suspending particles. When the surface energy of the collector γ is reduced, it is expected that the movement pattern of the particles, and their attachment efficiency, will change too.

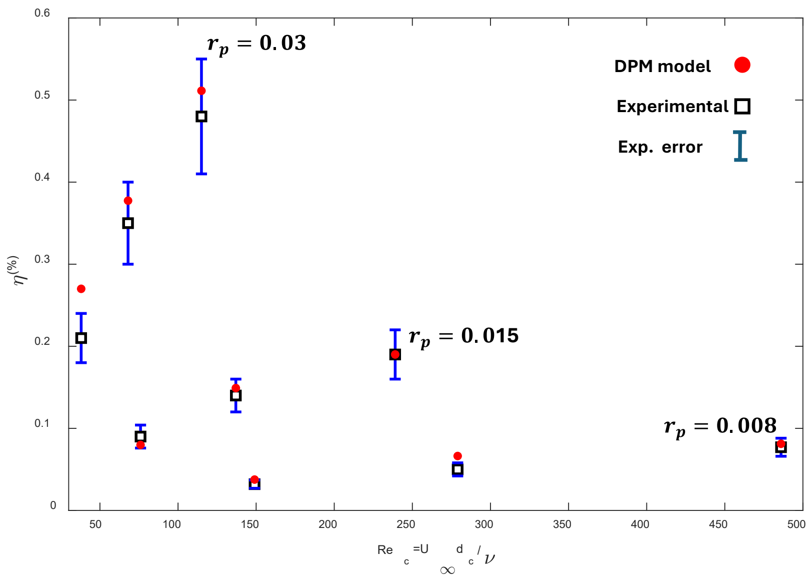

Fig. 2.6. Particle capture efficiency (η, %) using CFD-DPM model (red filled circles) compared to laboratory results of Palmer et al. (2004) (empty rectangles) for particle relative sizes of 0.03, 0.015, and 0.008. The error bars are for Palmer et al. (2004) experiments.

To find the range of γ for the aquatic environments, a preliminary test was performed for the highest Reynolds number tested i.e. for $Re_c = 486$. A surface energy of $\gamma = 5$ gave similar results for the capture efficiency observed in experiments of Palmer et al. (2004) i.e. 0.084%. Assuming that the results from this this surface energy would be the prefect attachment efficiency for lower Reynolds numbers using the DEM approach, further calculations were made and compared to DPM model and experiments of Palmer et al. (2004). The results are shown in table 2.2. The performance of the DEM method was within the range of observations of Palmer et al. (2004) and compared reasonably with the DPM for perfect capturing assumption except in low Reynolds number flows on order of $Re_c = 68$ and $Re_c = 76$.

Table 2.2 Comparison of the results from the DEM model with perfect attachment, the DEM model with collector stickiness, and the Palmer et al. (2004) laboratory studies for the same Reynolds numbers Re_c, and particle relative size R. The surface energy was assumed $\gamma = 5\,mJ/m^2$ for all CFD-DEM experiments.

Experiment set.	$\boldsymbol{Re_c}$	$\boldsymbol{R}$	**Palmer et al. (2004) (%)**	**Numerical DPM (%)**	**Numerical DEM (%) with $\boldsymbol{\gamma = 5\,mJ/m^2}$**
1	38	0.031	0.21 ∓ 0.03	0.27	0.27
2	68	0.031	0.35 ∓ 0.05	0.38	0.31
3	115	0.031	0.48 ∓ 0.07	0.518	0.49
4	76	0.015	0.094 ∓ 0.014	0.0798	0.12
5	137	0.015	0.14 ∓ 0.02	0.15	0.16
6	239	0.015	0.19 ∓ 0.03	0.19	0.21
7	149	0.008	0.032 ∓ 0.005	0.038	0.052
8	279	0.008	0.050? $\mp$0.008	0.066	0.071
9	486	0.008	0.077 ∓ 0.011	0.081	0.084

Several explanations may exist for discrepancies between DPM and DEM model results in Table 2.2. First, the drag formulation in the DEM software (Morsi and Alexander drag law) was different from the Stokes drag with Cunningham correction factor which was used in the DPM model. The performance of drag laws could be different for low Reynolds number flows especially near the collector region where the local Reynolds number of the particles are lower. Second, the time interval for exporting the flow field data may affect the results for the DEM model. Here we used a 0.02s intervals for exporting of data, and some particles on this interval may not follow the same path when smaller time steps are used for integration of their trajectory. Third, one-way coupling may not be adequate for smaller Reynolds numbers as the flow momentum may be influenced by the particles' momentum near the collector region. Nevertheless, the results from the DEM model showed major observations from the experiments in Palmer et al., and in the same order of the results from both DPM model and the experiments.

The DEM model results with $\gamma = 5\, mJ/m^2$ that was comparable to perfect attachment results showed that for all the experiments, the particles were attached to the front side of the collector. Figure 2.6 shows the attachment of particles on the collector for two particle sizes of $r_p = 0.031$ (fig. 6a) and $r_p = 0.008$. The attached particles are those that remained on the surface of the collector at the end of experiments, and they have been colored by their residence time. The right panel curves at each figure also show the time rate of number of particles deposited. A visual inspection of the particle attachment behavior showed that there were usually two or three rates of attachment to the collector, an initial higher rate followed by a slower rate (slope of lines in Fig. 2.7). For larger particles (Fig. 2.7a), the accumulation of particles on the surface of the collector started from particles making contact in the stagnation region on the front side and from particles that contacted the collector from the upper and lower sides of the collector. This mostly constituted the first stage of attachment with a rapid increase in particles' attachment. After this stage, the particles arriving from the stagnation region rolled on the surface of the collector and filled the voids between attached particles until the maximum capacity of the surface collector was reached, after which particles could not deposit further due to unavailable surface area. For finer particles (Fig. 2.7b), in contrast, the attachment was more random, and mostly the interaction of the incoming particles was with the collector surface rather than already deposited particles.

Surface energy influenced the particle distribution on the collector relative to the perfect attachment case as shown in Table 2.3 which shows the results of the experiments for different Reynolds numbers Re_c, relative particle sizes r_p, and the three values of dimensionless surface energies. As the last column of Table 2.3 shows, for all the tested Reynolds numbers and particle sizes, the lowest value of the surface energy i.e. $\phi = 51.8$ reduced the attachment efficiency, and this degree of reduction was higher for higher Reynolds number flows. This was typically due to higher shear stress on the collector that induced erosion of the particles from the surface of the collector due to smaller resisting adhesive forces against erosive ones.

In further exploring the influence of surface energy on attachment on the collector (Table 2.3), additional simulations were performed to create a more detailed curve for attachment efficiency as a function of surface energy for three Reynolds numbers of Re_c=76, 137, and 239 and particle relative size of $r_p = 0.015$ (Fig. 2.9). Fig. 2.9 shows that in aquatic environments, a slight increase in collector surface adhesiveness is sufficient for direct interception of particles, and the resultant attachment efficiency may even surpass that obtained under perfect attachment assumption.

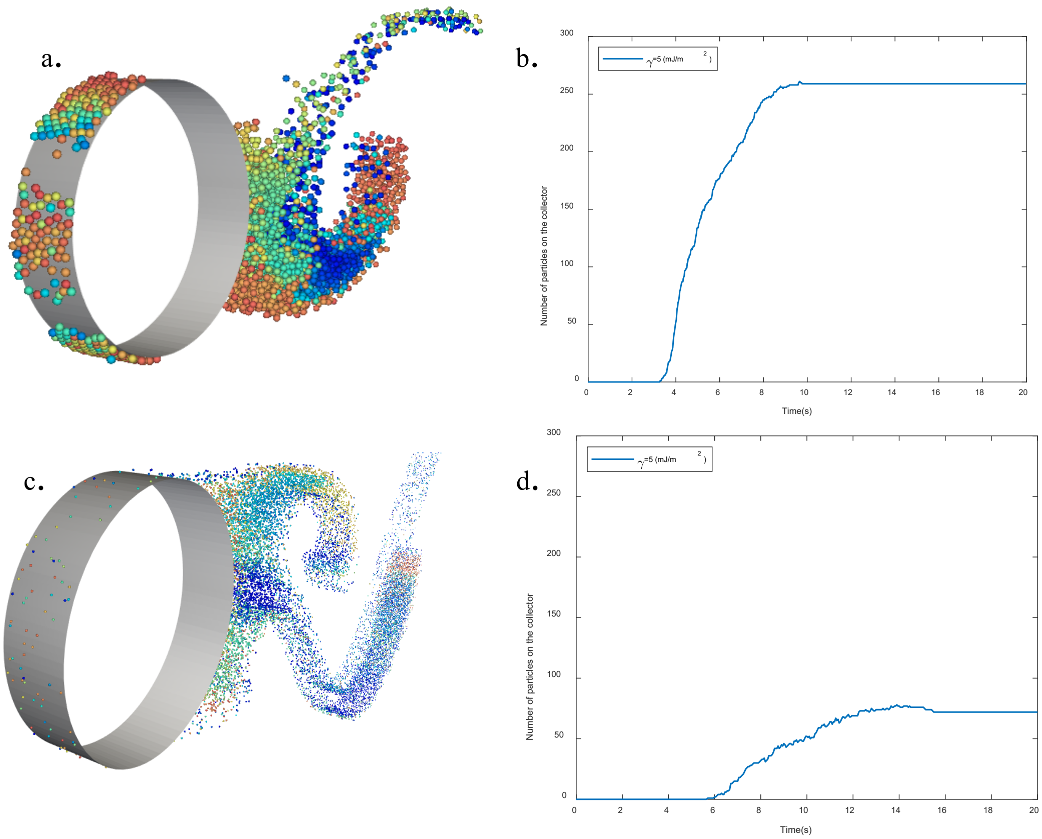

Figure 2.7. Snapshot of final particle distribution (a, c) on the collector (20 sec of simulation time) in the DEM model with perfect attachment (left images) and total particle attachment over time (right panels) for (a, b) $Re_c = 115$, $r_p = 0.031$, $\gamma = 5\, mJ/m^2$ and (c, d) $Re_c = 149$, $r_p = 0.008$, $\gamma = 5\, mJ/m^2$. Particles are colored by their residence time from the shortest (blue) to longest (red).

Table 2.3. The particle attachment efficiency results of CFD-DEM as a function of dimensionless surface energy ϕ. The last column is percentage of increase in relation to the case of perfect attachment efficiency.

Experiment set	Re_c	r_p	ϕ	Palmer et al. (2004)	CFD-DEM (Perfect attachment efficiency)	CFD-DEM	Percent increase relative to perfect attachment
1	38	0.031	51.8	0.21 ∓ 0.03	0.27	0.19	-29.6
2	38	0.031	20700			0.89	231.1
3	38	0.031	51800			0.79	192
4	68	0.031	51.8	0.35 ∓ 0.05	0.31	0.177	-34.4
5	68	0.031	20700			0.548	102.9
6	68	0.031	51800			0.546	102.2
7	115	0.031	51.8	0.48 ∓ 0.07	0.49	0.058	-88
8	115	0.031	20700			0.62	26.5
9	115	0.031	51800			0.66	34.7
10	76	0.015	51.8	0.094 ∓ 0.014	0.12	0.07	-41.7
11	76	0.015	20700			0.21	77.5
12	76	0.015	51800			0.22	83.3
13	137	0.015	51.8	0.14 ∓ 0.02	0.16	0.062	-61.2
14	137	0.015	20700			0.28	74.3
15	137	0.015	51800			0.27	70.6
16	239	0.015	51.8	0.19 ∓ 0.03	0.212	0.059	-72.2
17	239	0.015	20700			0.352	66.04
18	239	0.015	51800			0.27	54.2
19	149	0.008	51.8	0.032 ∓ 0.005	0.052	0.063	21.1
20	149	0.008	20700			0.064	23.07

21	149	0.008	51800			0.068	31
22	279	0.008	51.8		0.071	0.049	-30.9
23	279	0.008	20700	0.05 ∓ 0.008		0.096	34.8
24	279	0.008	51800			0.076	7.04
25	486	0.008	51.8	0.077 ∓ 0.011	0.084	0.037	-55.9
26	486	0.008	20700			0.011	30.9
27	486	0.008	51800			0.084	0

Marine environments including saltmarsh platforms are exposed to bacterial and microbial attachment, and biofilm formation. The initial attachment of these bacteria is followed by release of extracellular polymeric substances (EPS) acting as adhesives (Callow and Fletcher, 1994). As Fig. 2.9 suggests, the surface energy $\phi \cong 500$ of these biofilms leads to attachment of the suspending particles. On the other hand, it is expected that intercepted sediment particles contain organic materials which act as substrates for further microbial colonization. Microorganisms utilize these organics and produce EPS, heightening biofilm adhesiveness, which, in turn, enhances particle attachment. Hence, any indication of biofilm formation on the saltmarsh stems may indicate that the use of formulas in the literature developed for perfect attachment assumption may be justified, although these formulas might underpredict the attachment efficiency in some cases. Seasonality also brings formation and destruction of biofilms on the stems which induce variation in the attachment efficiency of particles as well.

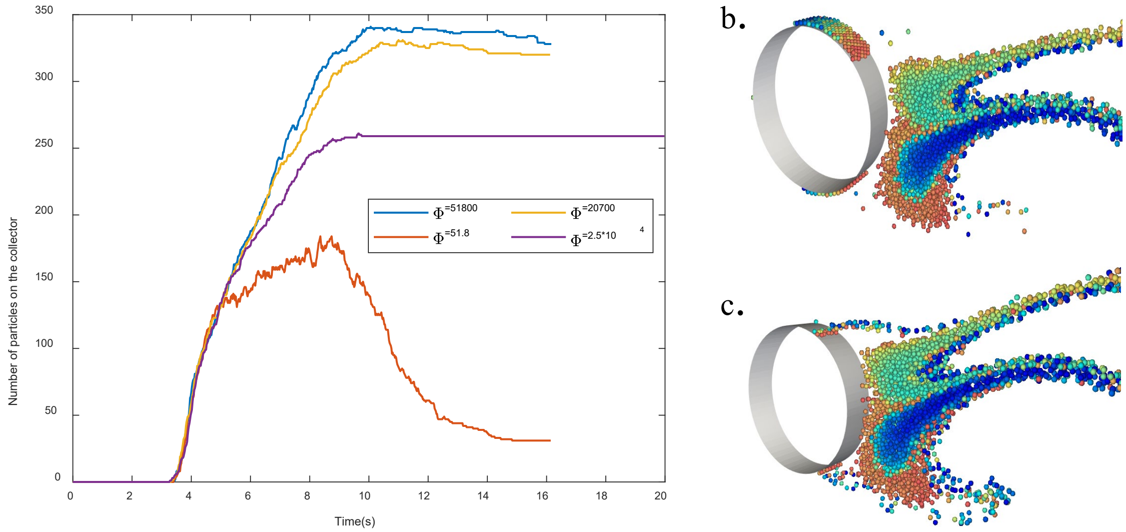

Fig. 2.8. a) Total particle attachment over time in terms of number of deposited particles on the collector for Rec=115 and $r_p = 0.031$ for different dimensionless surface energy values ϕ (Table 2.33, experiment set 7-9) and perfect attachment (Table 2.2, experiment set 3). Final configuration of particles on the collector from downstream wake viewpoint are shown for ϕ =20700 (b) and ϕ =51.8 (c). Particles are colored by their residence time from the shortest (blue) to longest (red).

To best knowledge of authors, there has not been a systematic investigation quantifying the surface energy of biofilms in marine aquatic environments, although its significance has been emphasized in geomorphology of saltmarsh platforms in terms of adding resistance to erosion of particles on the bed (Brooks et al., 2021). This research indicates that quantifying the surface energy of biofilms in the environment would be warranted to ensure that the perfect attachment assumption is robust.

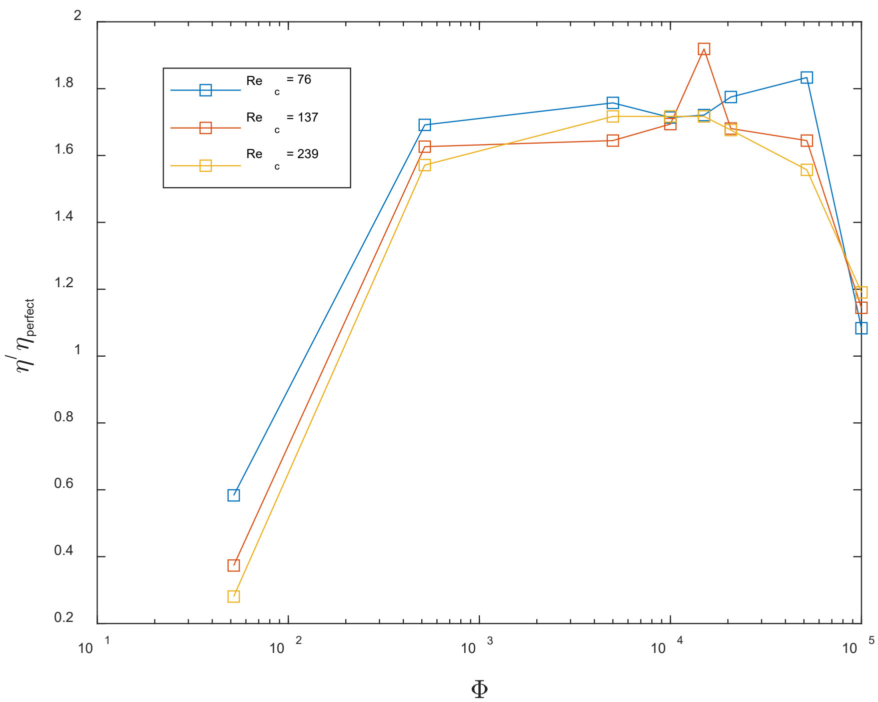

Figure 2.9. The variation of attachment efficiency η with respect to the perfect attachment efficiency, $\eta_{perfect}$ (Table 2.3, column 6) versus the dimensionless surface energy (ϕ) for simulations with Reynolds number (Re_c) = 76, 137, and 239 and particle relative size $r_p = 0.015$.

The CFD-DEM methodology presented here can be extended to more complex configuration of collectors as well as particle properties. Saltmarsh species are usually found to be colonized and depending on the proximity of stems and their arrangement, the flow hydrodynamics may be substantially different from that around a single stem. Changes in vortex shedding frequency with plant density were observed to affect the particle attachment behavior in the group of cylinders (Purich, 2007). While laboratory experiments are limited in non-intrusive examination of the flow field and particle suspension, the CFD-DEM technique presented here lift these restrictions and give better ideas with more versatility in terms of configuration of plants, their density, and flexibility. In addition, the simulated behavior of particles may undergo changes under the influence of other particles and the environments, including particle size gradation, charging under effect of salinity (electrostatic forces), buoyancy under effect of stratification, flocculation under particle-particle interactions, turbophoresis due to turbulence effect, and thermophoresis due to heat gradients. These factors may affect the behavior of particles and ultimately their attachment efficiency on a collector which needs further exploration.

Conclusion

Direct interception of particles by vegetation stems like saltmarsh has been observed in field studies as an important contributor to removal of suspended particles from body of water (Stump, 1984). The numerical studies of the particle attachment on a vegetation have been mainly with the assumption of particle adhering to the surface of the collector or stem and remain attached upon their first collision with the collector (e.g., Espinosa et al., 2012;2013). This paper first showed the applicability of Eulerian-Lagrangian numerical models in prediction of particle capture by a single stem represented as a cylinder. The discrete phase model (DPM) was able to reproduce particle capture efficiency with the perfect attachment assumption, but it was not able to simulate the interaction of the collector surface and particles in a realistic way. On the other hand, the discrete element model (DEM) lifted the assumption inherent in DPM by simulating surface energy and adhesiveness of the collector.

Results of the DEM model showed clearly that the particle attachment efficiency was controlled by the surface energy of the collector. The competition between adhesive forces and destabilizing forces determined the fate of the attached particles. For very high surface energies, the results from the DEM model showed good agreement with laboratory observations when the collector was greased (perfect attachment assumption). When surface energy was low, the particles adhered to the surface of the collector, rolled, or slid on the surface, and accumulated near boundary separation lines on the collector, resulting in higher attachment efficiencies than values obtained under perfect attachment assumption.

These model results indicate that the minimum surface energy needed by the adhesive texture of biofilms can be on the order of ϕ=500 to keep the particles on the collector. For larger surface energies, the attachment efficiency can amount to 1.8 times higher than that obtained through perfect attachment assumption as figure 2.9 shows.

Further numerical model experiments using CFD-DEM model with adhesive forces on the collector could unravel complexities associated with a patch of vegetation, because the interaction of neighboring stems can induce change of behavior of particles that might be different from a single collector. This research is currently being undertaken.

Chapter 3: CFD-DEM modeling of particle capturing by cylindrical stems in a vegetation patch

Abstract

This chapter investigates the capture efficiency of suspended particles by a patch of emergent vegetation, modeled using Computational Fluid Dynamics (CFD) coupled with the Discrete Element Method (DEM). Two arrangements of cylindrical stems, or collectors, were assumed: a regular triangular arrangement and a random arrangement, which better represents natural saltmarsh settings. For each arrangement, three vegetation densities were examined: low density (solid volume fraction λ=0.035), intermediate density (λ=0.075), and high density (λ=0.15). The CFD-DEM model included a high surface energy for collectors to ensure particles remained attached upon their first collision. Results for Reynolds numbers in the range $38 \leq Re_c \leq 600$ and a single particle size indicated that the patch averaged capture efficiency increases with vegetation density. Furthermore, capture efficiency for each density peaked at a specific Reynolds number, beyond which efficiency changed minimally, suggesting a saturation effect of the collectors. Unlike single-collector scenarios where no rear-side deposition was observed, the collectors within the patch were able to draw particles and facilitate attachment to their rear side, which accounted for up to 35% of total deposited particles on collectors.

Introduction

Nature-based solutions have emerged as effective methods to both preserve ecosystems and mitigate the impacts of coastal habitat degradation caused by human activities and sea level rise. Saltmarsh platforms, positioned as buffer zones between land and ocean, play a critical role in this protective function. It is well established that vegetation patches reduce flow velocity by increasing bed roughness, thereby enhancing particle deposition through gravitational settling (Elliot, 2000). Additionally, vegetation stems and leaves can capture suspended particles in the flow via direct interception; particles attach to these components upon contact. Field studies, such as those by Stumpf (1983) in the Delaware estuary and by Li and Young (2009) in the Yangtze River delta saltmarsh platform, have identified this process as a significant mechanism for the removal of suspended particles. However, limited research has examined how factors like vegetation geometry, planting density, and spacing from a nearby collector influence the effectiveness of vegetation stems in direct particle interception. This research aims to fill this gap by systematically investigating these parameters to better understand and optimize particle capture in vegetative environments.

There are two primary mechanisms for particle capture on vegetative stems (Palmer et al., 2004). In *direct interception*, very fine particles tend to follow the flow streamlines closely and can come into contact with the vegetation if they are sufficiently close to the surface of collector. In contrast, *inertial impaction* occurs when particles deviate from the flow streamlines due to their inertia, leading them to directly impact the vegetation surface. The distinction between these processes is often expressed in terms of the Stokes number. The Stokes number St is defined as the ratio of particle relaxation time $\hat{\tau}_p = \rho^+ D_p^2/18\nu$ to a fluid time scale $\hat{\tau}_f = D_c/2U_\infty$. Here, D_p is the particle diameter, D_c is collector diameter, U_∞ is the approaching velocity far upstream of the collector, and ν is the kinematic viscosity of the fluid (Haugen and Kragset, 2010; Michaleides, et al. 2023). For $St \ll 1$, the particle has enough time to respond to changes in fluid velocity and follow the streamlines, but for $St \gg 1$ the particles deviate from the streamlines due to their additional inertia relative to the flow (Michaelides, et al. 2023). Using numerical modeling, Haugen and Kragset (2010) showed that particles adhere to the surface of a collector through direct interception for $St < 0.1$ while for $St > 0.1$, the main mechanism was inertial impaction. Particles suspending in aquatic environments such as flow through saltmarsh stems have very small Stokes numbers and follow the flow streamlines, therefore the main mechanism of adherence to the surface of the collector or vegetation stem is through direct interception (Palmer et al., 2004; Spinosa et al., 2011), the focus of this study.

The particle attachment efficiency η, i.e., the number of particles intercepted by the collector divided by the total number of the particles released from a window of length equal to the diameter of the collector (Figure 3.1) has been shown to be dependent on dimensionless variables including the particle size ratio $r_p = R_p/R_c$, the particle density ratio $\rho^+ = \rho_p/\rho$, the collector Reynolds number $Re_c = (\rho U_\infty D_c)/\mu$, and the Peclet number $Pe = U_\infty D_c/\Gamma_p$, where R_p is the particle radius, R_c is the collector radius, ρ_p is the particle density, ρ is the fluid density, U_∞ is the approaching flow velocity far upstream of the collector, D_c is the diameter of the collector, and Γ_p is the diffusivity of the particles (Palmer et al., 2004). Laboratory experiments by Palmer et al. (2004) showed that particle capture efficiency can be described by two major variables of relative particle size r_p and collector Reynolds number Re_c, and its amount is increasing with both variables. Using direct numerical simulation (DNS), Spinosa et al. (2012, 2013) extended studies of Palmer et al. (2004) up to $Re_c = 1000$. Their results confirmed that capture efficiency is directly correlated with collector Reynolds number and particle relative size as observed by Palmer et al. (2004).

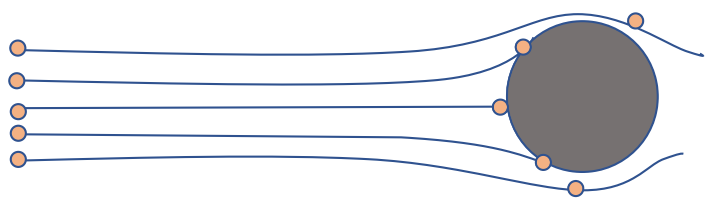

Figure 3.1. Schematic representation of an idealized vegetative stem (dark gray circle) acting as a collector, with direct interception of particles (orange circles) adhering to the collector's surface. Blue lines indicate flow streamlines around the collector. Adapted from Palmer et al. (2004), with modifications by Khademishamami et al. (under review).

While Palmer et al. (2004) and Spinosa et al. (2012, 2013) focused on particle capture by single collector, other studies have explored particle capture using multiple collectors arranged to represent vegetative stems. Purich (2006) examined how density of stems affects capture efficiency through laboratory experiments. To ensure particles adhered to the collector upon first contact, he coated the stems with grease, a technique also used by Palmer et al. (2004) in their laboratory experiments for a single collector, and also assumed by Spinosa et al. (2012) in their DNS simulations of particle capture by a single collector.

Purich (2006) utilized sediment with properties consistent with those in the studies by Palmer et al. (2004), ensuring similar specific density and relative particle size (particle diameter relative to collector diameter). He explored three solid volume fractions or vegetation densities, defined as the ratio of total volume of cylindrical shaped collector to the total volume occupied by the vegetation stems. His findings showed that capture efficiency did not show a direct correlation with collector Reynolds numbers above approximately 200. Unlike Palmer et al. (2004), who observed increased capture efficiency with Reynolds number for a single collector, Purich's results indicated no such trend for grouped cylindrical stems. With respect to vegetation volume fraction, his experiments showed that an intermediate density of stems achieved the highest capture efficiency, while the densest arrangement resulted in the lowest capture efficiency at a fixed Reynolds number (Figure 3.2a). He attributed this pattern to high-speed rotational eddies, caused by an increased vortex shedding frequency, which was most pronounced at intermediate densities.

Fauria et al. (2015) conducted experiments on low and high vegetation stem densities using natural, bladed vegetation. In a set of high-density experiments, biofilm was allowed to grow naturally on the stems to enhance their adhesive properties. Their results showed that particle capture efficiency was higher for low-density vegetation than for high-density vegetation and was lower than the efficiency predicted by the single-collector formula from Palmer et al. (2004). Consistent with the findings of Purich (2006), Fauria et al. concluded that capture efficiency decreased as approaching velocity, or collector Reynolds number, increased. They attributed this decline to particle resuspension after initial deposition on the stems at higher Reynolds numbers (Figure 3.2b).

While the laboratory experiments of Purich (2006) and Fauria et al. (2015) demonstrated the significance of stem density on capture efficiency, numerical studies focusing on particle attachment to groups of collectors in aquatic environments have received limited attention. A validated numerical model could offer valuable insights into various natural scenarios, such as the effects of particle size distribution, collector flexibility, particle aggregation, and complex flow properties, including unsteadiness from waves and stratification. Numerical modeling also enables non-intrusive visualization of flow and particle dynamics. For instance, Purich (2006) used an Acoustic Doppler Velocimeter (ADV) for flow measurements, but this intrusive instrument is affected by proximity to walls or stems, potentially causing artificial blockage and dispersion effects near collectors.

The objective of this research is to apply a high-resolution computational fluid dynamics (CFD) model coupled with a Discrete Element Method (DEM) to investigate factors influencing particles capture efficiency within a patch of cylindrical collectors resembling vegetation stems. The DEM is a Lagrangian particle trajectory model that incorporates a comprehensive force balance on individual particles, accounting for fluid flow, particle-particle interactions, and particle-collector interactions. In this DEM framework, the degree of particle adhesion to the collector is governed by a balance of adhesive forces that resist erosion upon attachment, as well as dominant forces that may promote particle resuspension or erosion from the collector surface. With this major advantage of the CFD-DEM framework, the degree of adhesion of the collector can play role effectively without any assumptions by the user, therefore allowing for a systematic exploration of the processes that contribute to particle attachment, retention, and resuspension from collector surfaces.

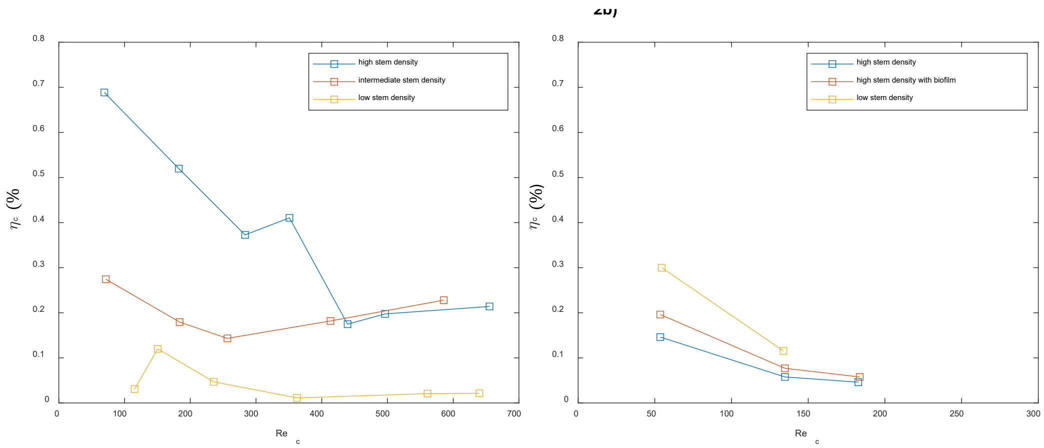

Figure 3.2**.** Attachment efficiency for vegetation stems as observed in two sets of experiments: (a) Purich (2006), which examined particle attachment efficiency across high, intermediate, and low stem densities; and (b) Fauria et al. (2015), which explored attachment efficiency for low and high stem densities, including tests with biofilm-coated stems for enhanced adhesion.

Materials and Methods

The numerical model framework employed an Eulerian-Lagrangian approach. For this CFD-DEM setup, two commercial software packages, Ansys Fluent and Ansys Rocky, were integrated to solve the Eulerian and Lagrangian fields, respectively. A one-way coupling approach was used here i.e. it was assumed that only the flow field affected the particle motion, and any effect from particles on flow momentum and turbulence was neglected. A detailed description of the governing equations in the CFD-DEM model implemented here was elaborated in chapter 2.

The model domain consisted of vegetative stems arranged in either regular or random spacing with a fixed diameter. First, Unsteady flow simulation was conducted to reach a stationary state in terms of boundary layer development and flow establishment. Then, the flow field data including velocity components, and turbulence quantities such as kinetic energy and dissipation rate were recorded every 0.02s to be exported to the DEM software. In the next stage, the flow field and geometry were exported to the DEM software, and simulation was setup for each experiment.

The attachment efficiency in the CFD-DEM framework for a collector inside the patch can be expected to be a function of below dimensionless variables:

$$\eta = f\left(\frac{\rho_p}{\rho}, Re_c, \frac{R_p}{R_c}, \gamma/\left(\rho_p {U_0}^2 R^*\right), E^*/\left(\rho_p {U_0}^2\right)\ , \lambda\right) \tag{3.1}$$

where

- $\frac{\rho_p}{\rho}$ is the specific density of the particle, with ρ_p density of particles, and ρ density of water.
- Re_c is the collector Reynolds number, which can be defined as $Re_c = U_0 D_c/\nu$ with U_0 being the approaching velocity far upstream the vegetation patch.
- $\phi = \gamma/\left(\rho_p {U_0}^2 R^*\right)$ is the dimensionless surface energy, with γ as the surface energy of the collector (See chapter for 2 for definition).

- $E^*/(\rho_p {U_0}^2)$ is the dimensionless modulus of elasticity, with E^* being the effective modulus of elasticity of particle and collector (See chapter 2 for definition)
- λ is the vegetation density which is defined here as the volume occupied by the collectors divided by the total volume spanning the vegetation stems.

The collectors were cylindrical, each with a diameter of $D_c = 10mm$. Following the experimental setup of Purich (2006), we used particles with a relative size of $r_p = 0.03$ and a specific density of s=1.03. Two configurations of collector arrangements were modeled: a regular triangular configuration and a randomized arrangement of collectors. For each arrangement, three stem densities were tested—high, intermediate, and low—corresponding to the densities used by Purich (2006). Collector Reynolds numbers Re_c were selected to range from 38 to 600, aligned with the experimental ranges in Palmer et al. (2004) and Purich (2006).

Regular arrangement of collectors

The regular arrangement of the collectors is shown in figure 3.3a. The patch of vegetation consists of 44 collectors in equilateral triangular arrangement. The dimension l which connects the center of collectors is $2.5D_c$, $3.5D_c$ and $5D_c$ which give patch volume fraction λ of 0.15, 0.075, and 0.035 respectively. There are four rows of collectors and eleven columns to ensure that the length of the patch is enough to have intermediate collectors not affected by upstream and downstream free flow regions. The geometry is three dimensional as required by CFD-DEM method, but for an economic mesh, it is only 3.5 mm in spanwise direction with one cell in that direction. The upstream boundary or inlet is 10 collector diameters far from the first column of collectors. The outlet is placed 35 collector diameters from the last column of collectors to minimize backflow as much as possible. Periodic boundary conditions were chosen for all spanwise boundaries. A structured hexahedral mesh was created using ICEM-CFD software with an O-grid mesh refinement in the vicinity of the collectors for resolving the boundary layer. The first element near the cylinder wall was placed 0.005mm from the cylinder surface as experience from single collector experiments gave suitable results for the boundary layer resolution and particle attachment results with this first layer distance from the collector surface (see chapter 2 for more details).

Random arrangement of collectors

In addition to the regular arrangement of collectors, a random configuration was tested across three volume fractions similar to the regular arrangement. To generate the random arrangement, a MATLAB script was used to disperse collectors of 10 mm diameter within a specified rectangular domain as the total volume spanning the vegetation domain. The script required inputs for the target volume fraction and rectangle dimensions enclosing the collectors. Using MATLAB's rand() function, the center coordinates of the collectors were assigned, ensuring that each generated circle did not overlap with neighboring circles. The code executed a loop to verify that the minimum center-to-center distance between adjacent circles was 14 mm to allow an achievable mesh implementation technique between the gaps of neighboring stems. To prevent circles from protruding through the domain boundaries, the minimum distance from any edge of the rectangle to the center of the nearest circle was set at 10 mm. The resulting circle configurations were exported as STL files into SpaceClaim CAD software for meshing preparation. Upstream and downstream flow regions were added to the patch, forming a 2D computational domain. Figure 3.4 shows the generated surface in SpaceClaim from the exported STL file for the three vegetation densities.

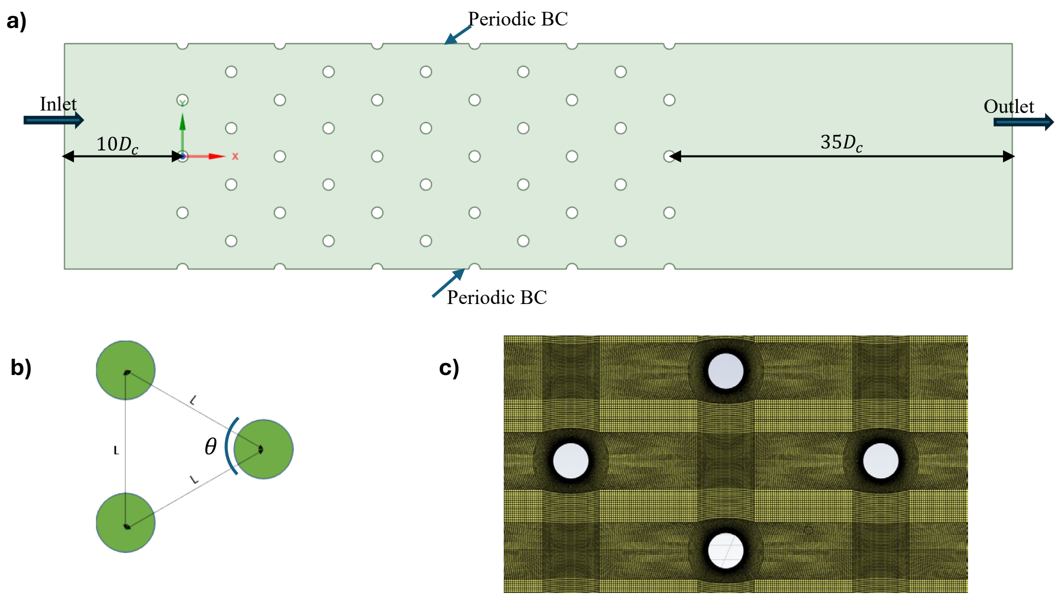

Figure 3.3 (a) Model domain geometry with boundary conditions (BC) for regularly spaced collectors. (b) Configuration of vegetation stems with collector diameter D_c and spacing L (center-to-center distance between collectors). Three spacing distances were examined: L=25 mm ($\lambda = 0.15$), L=35 mm ($\lambda = 0.075$), and L=50 mm ($\lambda = 0.035$) (c) Hexahedral mesh elements with O-grid refinement near collectors to capture boundary layer details.

For meshing of the random geometry, automatic mesh generation was performed using Ansys Meshing software, as manual O-grid generation in ICEM-CFD was challenging given the proximity and misalignment of randomly distributed circles. Near-wall mesh refinement captured the steep gradients adjacent to the collector walls. The 2D mesh was then extruded by

3.5 mm in the lateral direction, with a single cell in that direction, creating a quasi-3D domain suitable for CFD-DEM modeling.

Range of variables in the simulations

To simulate ideal attachment conditions, a high surface energy γ was set for the collectors to ensure particles adhered upon their first collision with the collector. Table 3.1 summarizes the variables used in the CFD-DEM model. Between 270,000 and 500,000 particles were released depending on the Reynolds number to have an approximately equal mass flux of particles into the domain for all experiments. The average concentration of particles with the sediment size of 0.3 mm diameter and a density of 1030 kg/m^3 used in this study was 16 g/l, which is higher than the values typically observed under normal flow conditions in saltmarshes. Fleri et al. (2019) reported a maximum sediment concentration of 0.2 g/l in Poplar Island, a microtidal Chesapeake estuary in Maryland, USA. Similarly, measurements by Sun et al. (2024) in a tidal creek of the Yangtze Delta showed sediment concentrations reaching up to 8 g/l. However, it is expected that significantly higher sediment concentrations can occur on a saltmarsh platform during flooding situations, driven by resuspension caused by wave and wind effects (Friedrichs and Perry, 2001). Thus, the assumed concentration in this study may be more representative of storm conditions, where a peak flux of particles is transported into the saltmarsh via tidal creeks. Several computational and physical considerations also justify the use of higher particle concentrations in these simulations. First, very low concentrations could result in insufficient particles numbers in the domain for a meaningful statistical analysis or for accurately capturing trends in attachment efficiency. Second, the mass flux of the particles may play a more important role as capture efficiency is defined as flux of particles deposited on the collector divided by the total flux of particles moving towards the collector. Third, the high concentration of particles remains within the limits of one-way coupling between fluid and sediment phases, which means the effect of the particles on fluid momentum is negligible. The volume fraction of sediments in the computational cells is around 2%, well below the 10% threshold for one-way coupling (Michaelides et al., 2022).

As mentioned in the previous section, the experiments consisted of two stages. In the first stage, the flow field in the CFD model was run to reach a stationary state. After reaching this stage, another run of the flow field was performed to record the flow variables such as velocity components and turbulence quantities to be used by the DEM package. These flow variables were exported at 0.02s intervals to be read by the Rocky DEM software for particle analysis. While running the simulations in the latter stage, the force components of drag and lift on the collectors were recorded as well. In the DEM software, particles were released from a perpendicular plane to flow direction set 50mm upstream of the first collector. A 20-second injection duration was applied, allowing sufficient time for particle transport to reach equilibrium within the domain. After particles exited the domain, the number of particles attached to each collector was counted, and the attachment efficiency for the patch was calculated as the ratio of total number of captured particles to the total particles released from an upstream vertical window, matching the domain size.

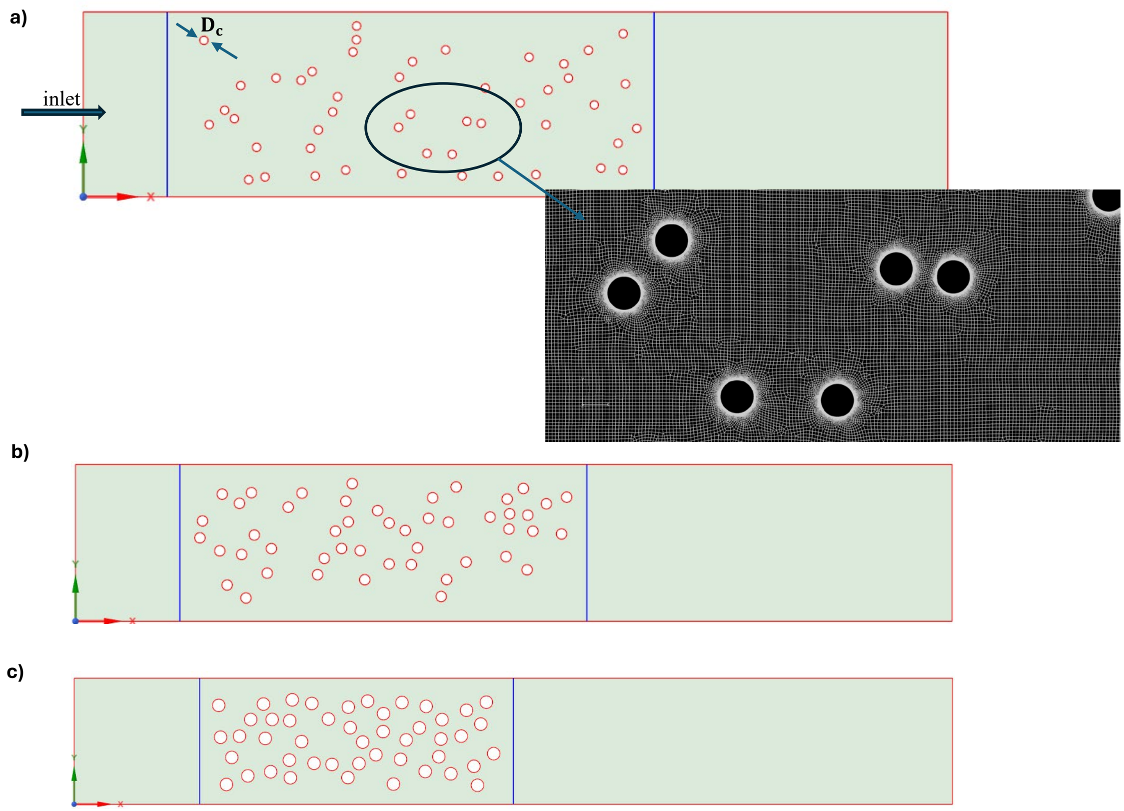

Figure 3.4. The numerical domain for random arrangement of collectors with stem density of a) $\lambda = 0.035$ b) $\lambda = 0.075$ and c) $\lambda = 0.15$. The total number of collectors were fixed as 48 collectors, similar to the regular arrangement. The lateral size of each domain was 3.5 mm with only one cell. The mesh consisted of 750,000 Hex-dominated elements with refinement near the wall regions. The domain size containing vegetation elements changes for reaching the desired volume fraction.

Table 3.1. Variables in the numerical model and their range of variation. The collector Reynolds number has been expressed based on the uniform flow velocity at the entrance U_∞ and collector diameter D_c . Relative particle size is the particle radius divided by collector radius which is fixed as 0.03. The volume fraction λ is the volume occupied by the collectors divided by the total volume in the collector region. γ is the surface energy of the collector defined in equation 3.1.

Collector Reynolds number $Re_c = (\rho U_\infty D_c)/\mu$	**Configuration**	**Particle relative size** $r_p = R_p/R_c$	**Volume fraction** λ	**Surface energy** $\gamma(\frac{mJ}{m^2})$
38 **38** **38**	Regular – low Regular - med Regular - high	0.03 0.03 0.03	0.035 0.075 0.15	11 11 11
68	Regular	0.03	0.035 0.075 0.15	32
115 **115**	Regular Random	0.03	0.035 0.075 0.15	50
279 **279**	Regular Random	0.03	0.035 0.075 0.15	290
486 **486**	Regular Random	0.03	0.035 0.075 0.15	890
600 **600**	Regular Random	0.03	0.035 0.075 0.15	1350

Results and Discussion

Fluid flow verification

The range of Reynolds numbers across all experiments suggested that vortex shedding was present for majority of experimental cases except the $\mathrm{Re}_c = 38$ case. The alternately shed vortices move downstream, transporting particles suspended in the flow and potentially guiding them toward downstream collectors. Vortex shedding frequency was quantified by calculating the Strouhal number $Str = fD_c/U_\infty$ where f is the dominant frequency, D_c is the collector diameter, and U_∞ is the upstream approaching velocity to the patch. The Strouhal number was derived from the power spectral density of the fluctuating lift force on the cylinders.

For the drag coefficient, the viscous and pressure components of the drag force were recorded throughout the simulation and subsequently averaged over time to obtain a time-averaged drag force for each cylinder. The time-averaged drag coefficient, C_D was then computed using the formula $F_D = 1/2\, C_D \rho A_{fc} {U_\infty}^2$, where A_{fc} is the frontal area of the collector, calculated as $W_c D_c$ with W_c representing the domain width.

Vortex shedding frequency

The large eddy simulation data from Stoesser et al. (2010) was used to qualitatively compare Strouhal number (Str) values for regular arrangement of the collectors. Stoesser et al. studied average and instantaneous flow fields around emergent cylinders arranged in a triangular configuration. Unlike our setup with an upstream free flow field, their model simulated an infinite domain fully vegetated with stems, implementing periodic boundary conditions that intersected with the cylinders. Their cylinders were arranged in a staggered pattern but differently compared to the equilateral arrangement in our case. Additionally, their domain included the channel bed, where bed-related drag contributed slightly to the total drag, though this contribution is typically minor relative to pressure drag in dense collector arrangements.

Stoesser et al. used three vegetation densities (volume fraction of stems) in their model: 0.251, 0.063, and 0.015. As illustrated in Figure 3.5, the Strouhal numbers observed in our experiments align with the general trends in Stoesser et al.'s LES simulations. Our results indicate that Strouhal number increases with vegetation density for a fixed Reynolds number, suggesting that vortex shedding frequency is positively correlated with the density of vegetation.

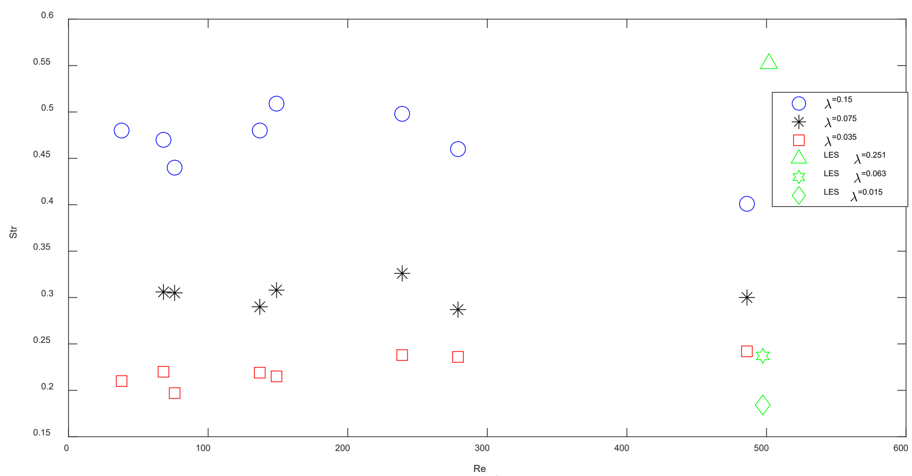

Figure 3.5. Strouhal number (Str) for three vegetation densities in the current numerical model with a regular arrangement of collectors, compared with results from the LES study by Stoesser et al. (2010). The plot illustrates the increasing trend in Strouhal number with vegetation density, supporting the observed correlation between vortex shedding frequency and vegetation density.

In contrast to the regular arrangement, where Strouhal (Str) number values were observed to remain uniform across the patch due to identical spacing, the random arrangement of collectors showed variability in Str values, influenced by proximity to neighboring collectors. This irregularity is qualitatively evident in the vorticity contours (see figure 3.6), which reveal the complexity of vortex patterns shed from cylinders. In the regular arrangement, the wake pattern is predictable, aligned with the consistent placement of collectors. However, in the random arrangement, some collectors could get submerged in the wakes of upstream cylinders, impacting their vortex shedding behavior. Additionally, lateral proximity to neighboring collectors promotes wake interference, contributing to irregularities in vortex shedding dynamics.

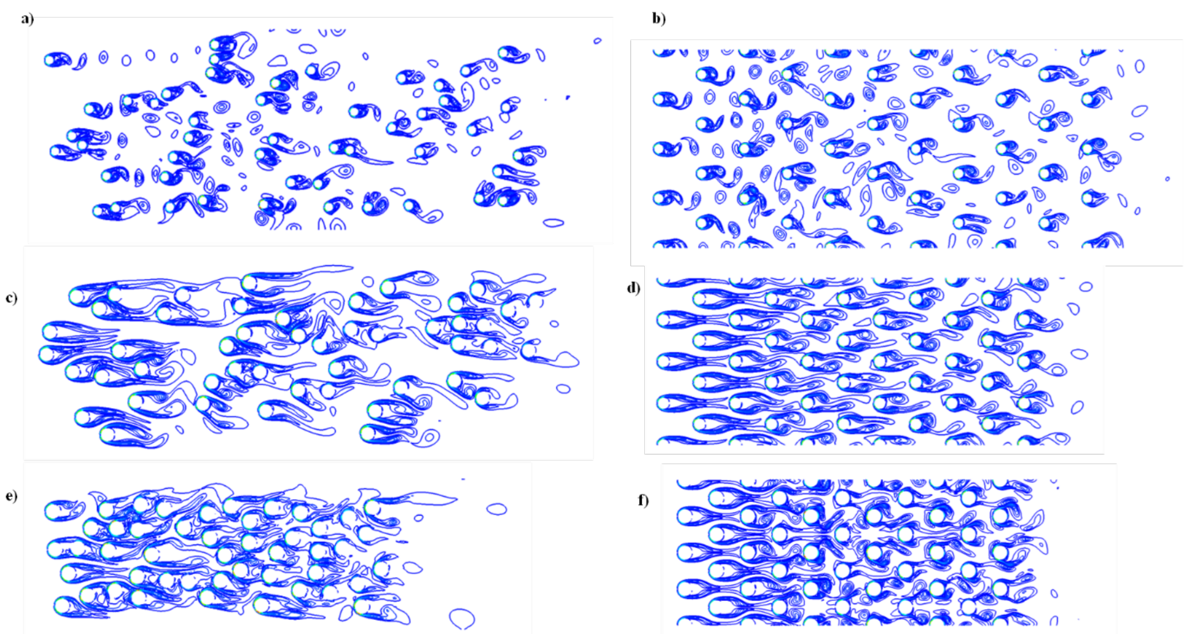

Figure 3.6. Vorticity magnitude contours for different configurations: a) random (λ = 0.035) b) regular (λ = 0.035); c) random (λ = 0.075) ; d) regular (λ = 0.075); e) random (λ = 0.15), and f) regular (λ = 0.15)

Figures 3.7a, 3.7c, and 7e display the variation of Strouhal number (Str) along the x-axis of collectors in random arrangements at three vegetation densities (λ = 0.035, 0.075, 0.15) and Reynolds numbers (Re_c = 115, 279, and 600). The x-coordinates correspond to the center of each collector, providing a spatial perspective on Str distribution. Figures 3.7b, 3.7d, and 3.7f present corresponding boxplots, illustrating central tendencies and variability across vegetation densities and Reynolds numbers.

In random configurations, Strouhal variability is particularly pronounced at low vegetation density (λ = 0.035), with high fluctuation seen especially at lower Reynolds numbers. This trend suggests that sparse arrangements allow for more irregular vortex shedding patterns, influenced by local flow anomalies and interactions with neighboring collectors. As density increases, vortex shedding stabilizes, likely due to wake interference from neighboring collectors, creating more consistent flow conditions. For lower density arrangements, Strouhal medians show minimal sensitivity to Reynolds number, indicating stability in vortex shedding frequency despite flow variations. At intermediate density (λ = 0.075), a slight increase in median Str is observed from Re_c = 115 to Re_c = 279, stabilizing at Re_c = 600. In the highest density (λ = 0.15), the Strouhal numbers are consistent across Reynolds numbers, suggesting that high-density arrangements promote stable vortex shedding. Outliers in the boxplots, more frequent at lower Reynolds numbers, indicate local flow disturbances and variability in shedding frequencies. Fewer outliers at Re_c = 600 suggest a stabilization of flow patterns with increased Reynolds number. Like regular arrangement, the plots here also shows that the median Str values are the highest for highest vegetation density.

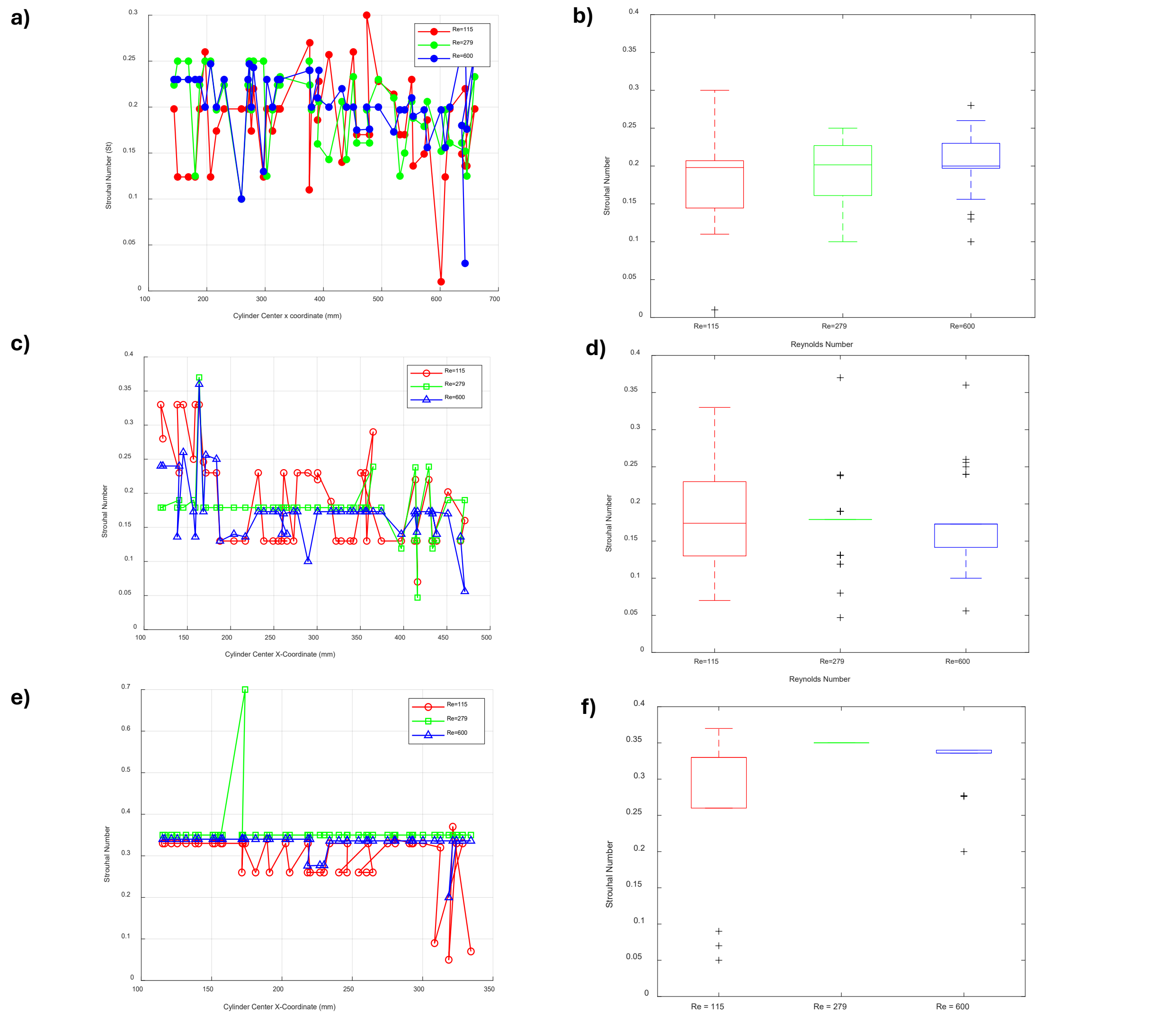

Figure 3.7. Strouhal number distributions for Reynolds numbers Re_c=115, 279, and 600 at vegetation densities (a,b) λ =0.035; (c,d) λ = 0.075; and (e,f) λ = 0.15, represented by red (Re_c=115), green (Re_c=279), and blue (Re_c=600) box plots, respectively. The central line within each box represents the median Strouhal number, while box height spans the interquartile range (IQR), capturing the middle 50% of values. Whiskers extend to the minimum and maximum values within 1.5 times the IQR, with color-matched outliers indicating values beyond this range.

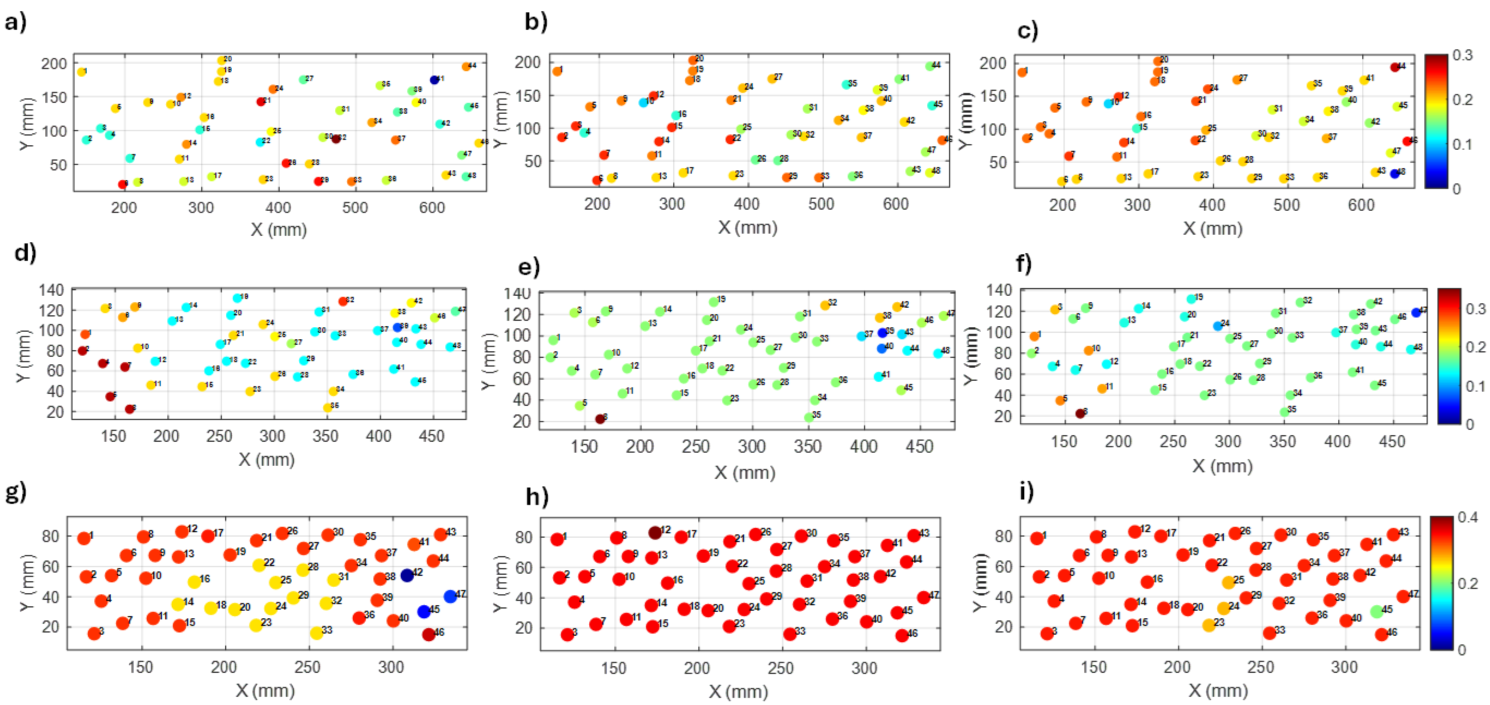

Figure 3.8. Variability of Strouhal number across different vegetation densities and Reynolds numbers. Panels indicate: (a) Re_c=115, λ =0.035 (b) Re_c=279, λ =0.035 (c) Re_c=600, λ =0.035 (d) Re_c=115, λ =0.075; (e) Re_c=279, λ =0.075 (f) Re_c=600, λ =0.075 (g) Re_c=115, λ =0.15; (h) Re_c=279, λ =0.15; and (i) Re_c=600, λ =0.15.

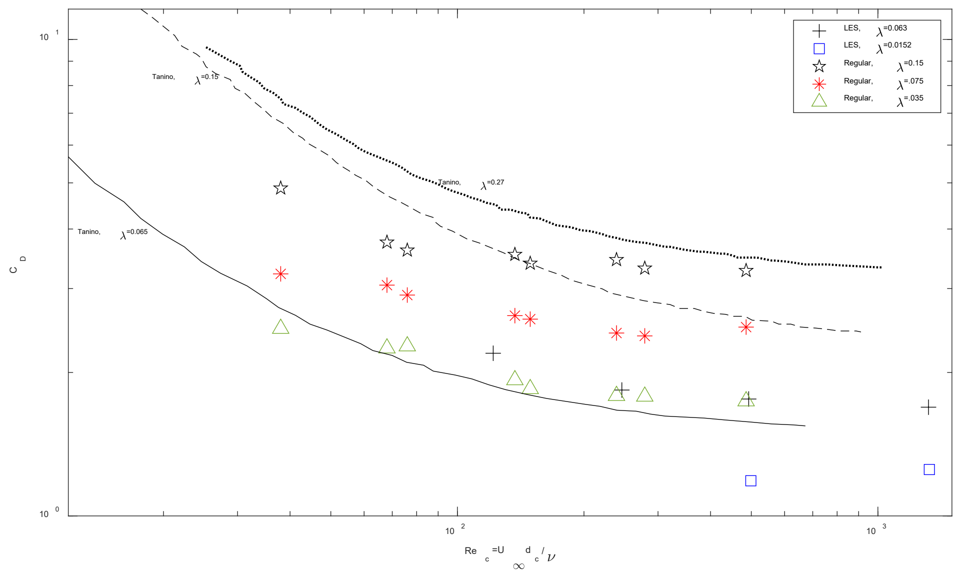

Figure 3.9. Comparison of the average drag coefficient $\bar{C}_D$ versus Re_c from the current numerical model and the large eddy simulation (LES) results of Stoesser et al. (2010), and Tanino (2008) for different vegetation densities λ.

To further illustrate the spatial variability of Strouhal numbers in random arrangements, a contour plot (Figure 3.8) visualizes Str variation across the collector domain. This representation underscores the influence of collector proximity and arrangement on vortex shedding, as demonstrated by Purich (2006), who identified shedding frequency as a critical factor in particle attachment. The contour plots reveal that particle capture efficiency may fluctuate based on spatial arrangement and density, with higher vegetation density probably producing a more uniform distribution of particles across the collectors.

Drag coefficient

The patch-averaged drag coefficient was calculated and compared with literature values from large eddy simulations of emergent vegetation (Stoesser et al., 2010) and laboratory data (Tanino, 2008) and is shown in Figure 3.9. Our results align with the trend seen in LES and laboratory data, indicating that drag coefficient increases with vegetation density. However, discrepancies in values between our model and those from Stoesser et al. and Tanino may be attributed to factors such as the exclusion of bed drag in our model, the three-dimensional flow considerations in Stoesser's LES model, and assumptions within our two-equation model, including isotropic turbulence and model constants.

DEM results for particle capture efficiency

In calculation of the attachment efficiency, either patch-averaged quantity, or attachment efficiency of a single collector inside the patch can be addressed. For practical applications, such as saltmarsh restoration, patch efficiency can be more informative since understanding particle removal from the patch edge to its interior aids in broader-scale modeling and informs restoration design decisions. This way, also the combined effects of turbulence, collector proximity, and positioning within the patch are taken into account with a spatial avaraging. As will be explained subsequently, the spatial variability of the flow hydrodynamics make the sampling of a collector for computation of single collector attachment efficiency much difficult.

The patch efficiency was calculated by summing the total number of particles deposited on the collectors inside the patch divided by the total number of particles released from the upstream vertical plane of equal size the CFD solution domain.

Particle capture efficiency of a single collector

To examine the performance of the DEM model in predicting the attachment efficiency of particles on groups of collectors, first the applicability of the model was tested for a single collector and verified with the laboratory experiments of Palmer et al. (2004). For a single cylinder, a surface energy of $\gamma = 5\ {}^{mJ}/_{m^2}$ made the particles attach to the collector surface upon their first impact for the highest Reynolds number i.e. Re_c= 486 which was the highest Reynolds number in Palmer et al. (2004) laboratory experiments. Comparison of results from the DEM model and experiments of Palmer et al. (2004) was reported in chapter 2. The overall agreement with the experiments was satisfactory, indicating that the DEM technique with JKR model could be reliable for subsequent analysis of particle attachment to a collector inside a patch.

Particle capture efficiency of regularly arranged collectors

The patch efficiency for a regular arrangement of collectors was calculated and plotted (Figure 3.10). Based on this data, for λ =0.15, the attachment efficiency tends to increase with Reynolds number initially, reaching a maximum around Re_c = 279, and then decreases slightly for higher Reynolds numbers. For λ =0.075 and λ =0.035, the attachment efficiency also increases with Re_c, but the trend is less pronounced, and efficiency stabilizes after Re_c = 115. The attachment efficiency is higher for λ =0.15 compared to λ =0.075 and λ =0.035 at all Reynolds numbers. This suggests that smaller spacing leads to better particle capture, which could be due to increased interaction and turbulence effects between the collectors. According to the results, the maximum capture efficiency is not exceeding 2.5% for the patch with regulary arranged collectors. The observation that the attachment efficiency does not increase with Reynolds number can be due to reaching to a satuarion point above which no particles can get deposited.

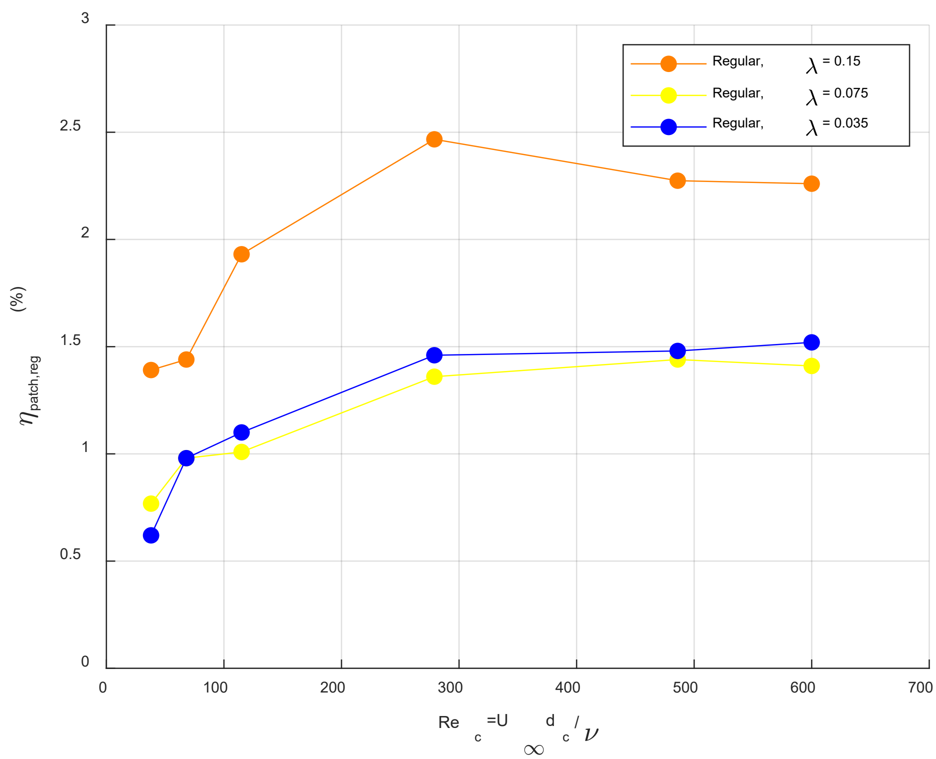

Figure 3.10. Variation of patch capture efficiency for relative particle size of dr=0.03 and regular arrangement of collector with λ =0.15 (Orange), λ =0.075 (Yellow), and λ =0.035 (Blue) with collector Reynolds number (Re_c).

In a regular arrangement of collectors, as shown in Figure 3.11, the flow can converge toward a downstream collector, directing particles toward it and enhancing their likelihood of attachment. Even-numbered columns (C4r2 and C6r2 in Figure 3.12) were observed to receive more particles than Odd-numbered columns (C5r2 and C7r2 in Figure 3.12) as a result of this process. This shows the significance of mean flow path in bringing the particles close to collectors. It was also observed that vortices emanating from upstream collectors can carry the particles and bring them closer to downstream collectors as can be seen in figure 3.12b. Therefore, the highest vortex shedding frequency in the highest vegetation density can be an influencing factor for more attachment of the particles.

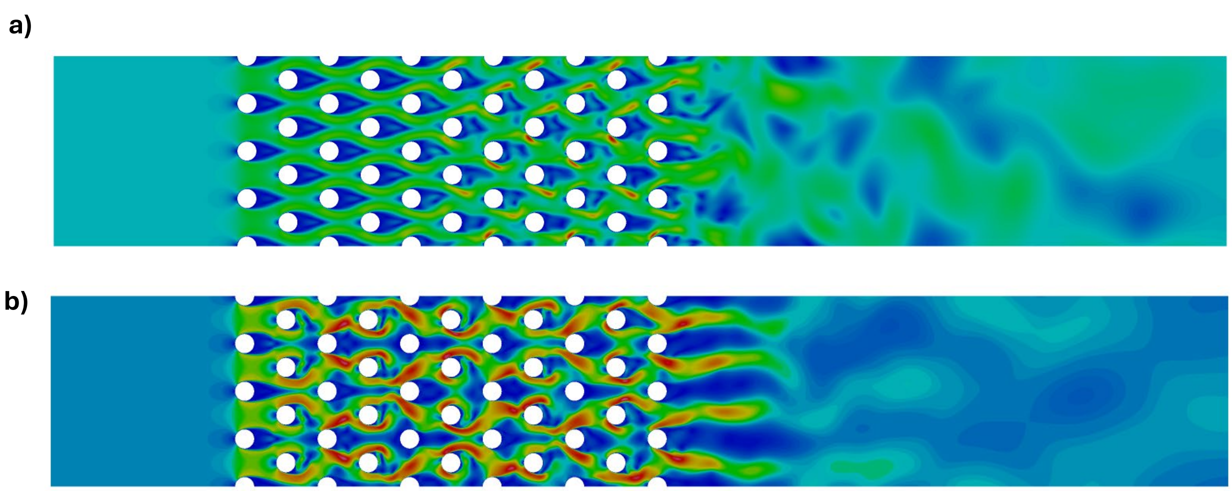

Figure 3.11. Velocity contours showing a schematic of the flow pattern for two Reynolds numbers of (a) Re_c=115 and (b) Re_c=486 for λ =0.15.

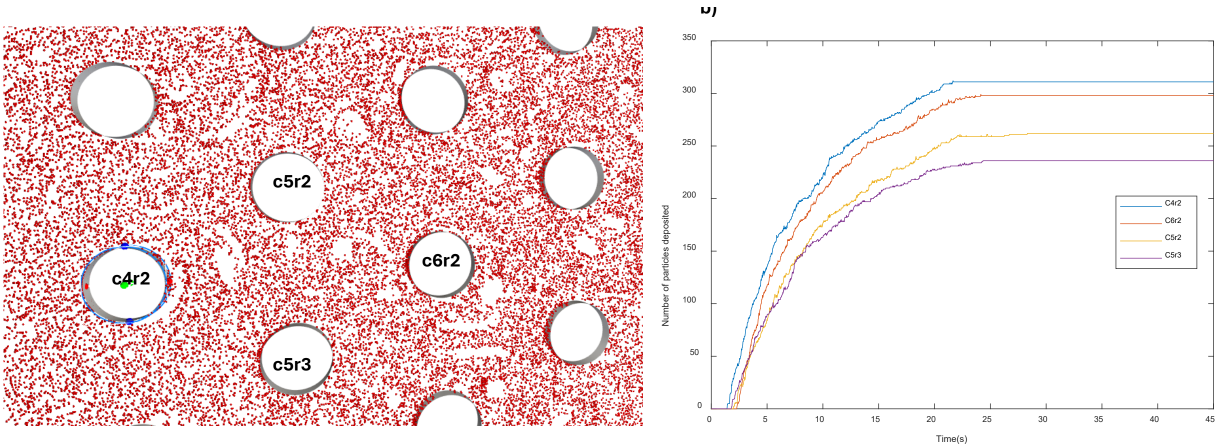

Figure 3.12 . A snapshot of particle trajectories in λ =0.15 and Re_c =486. The vortices eamanating from an upstream collector can transport the particles and bring them near collectors on the downstream lateral ones or the collector in line with an upstream one.

Particle were deposited in the back of the collectors in regular arragnement of collectors as well. The percentage of particles attached to the back of the collectors relative to total number of particles deposited on the collecotors was calculated and is shown in Fig. 3.13 for regular arrangement of collectors. As this figure shows, the spacing with λ =0.15 consistently has higher back efficiency compared to λ =0.075 mm and λ =0.035, especially at higher Reynolds numbers. The smaller spacing (λ =0.15) leads to more interaction between the wakes of adjacent collectors, which can create recirculation zones that are favorable for particle deposition. Across all the collector spacings, the back efficiency generally increases with the Reynolds number. The increase in back efficiency with Reynolds number indicates that higher flow rates enhance the likelihood of particles being carried into the wake region of the collectors, where attachment occurs. For L = 25 mm, the back efficiency seems to reach a plateaue at high Reynolds numbers

(Re_c =486 and Re_c = 600). This saturation behavior suggests that at high Reynolds numbers, the particle capture efficiency at the back reaches a limit, for another saturation phase of the collector.

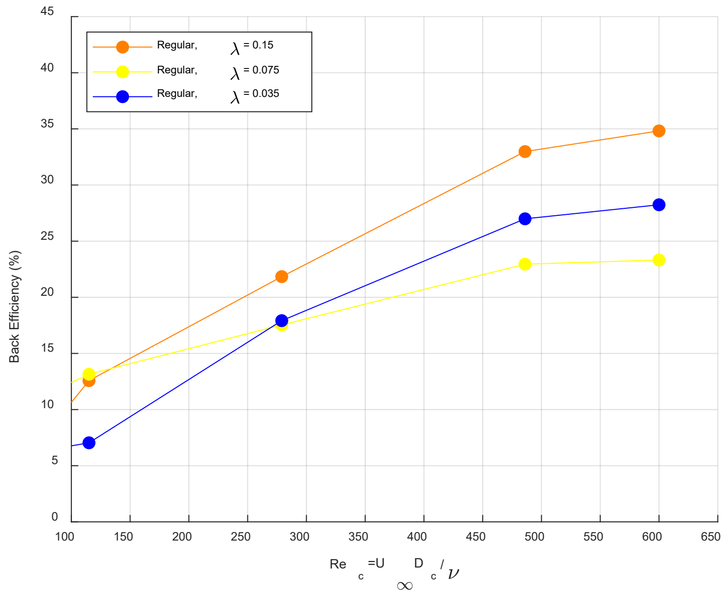

Figure 3.13. The back efficiency of the collectors in the regular arrangement. The back efficiency is here defined as the total number of particles deposited in the back of collectors across the patch divided by the total number of particles captured by the collectors. Results are for different vegetation densities L=25mm (λ =0.15) , L=35mm (λ =0.075) and, L=50mm (λ =0.035).

Particle capture efficiency of randomly arranged collectors

The patch efficiency was also calculated for random arrangement of collectors for different densities and Reynolds numbers, and is shown in figure 3.14 . As in the case of regular arrangement, the numerical results show that the highest vegetation density shows the highest attachment efficiency. Across all densities λ, we observe that attachment efficiency generally increases with the Reynolds number.

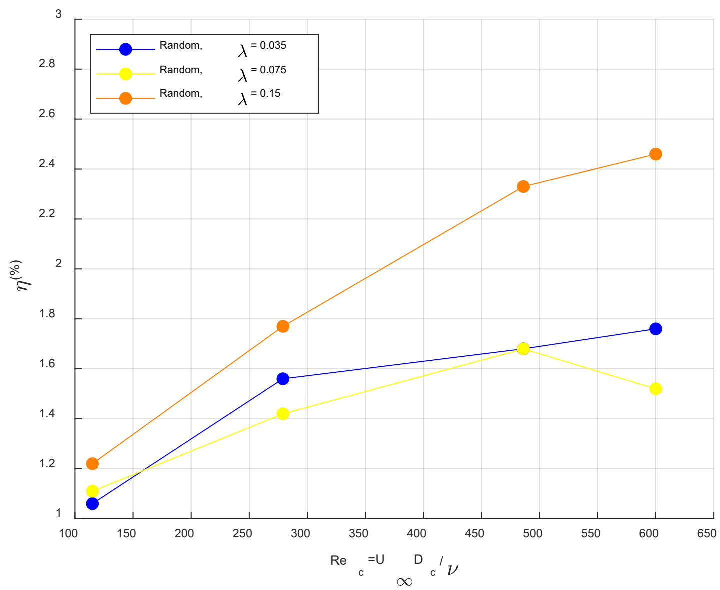

Figure 3.14. Variation of patch capture efficiency for random arrangement of collectors for density of λ =0.15 (Orange), λ =0.075 (Yellow), and λ =0.035 (Blue) with collector Reynolds number (Re_c).

As variation of back efficiency shows in figure 3.14, for low-density configurations (λ =0.03), the attachment efficiency starts at a lower baseline (1.06 at Re_c=115) and increases to about 1.76 at Re_c=600. For intermediate density (λ =0.065), there is a similar increase in efficiency but slightly higher at each Reynolds number compared to the low-density case. The higher density may offer a greater collective surface area for capturing particles, hence the slightly improved efficiency. For high-density configurations (λ =0.15), the attachment efficiency reaches its highest value, from 1.22 at Re_c=115 to 2.46 at Re_c=600. For each density, the increase in attachment efficiency between the highest two Reynolds numbers (Re_c =486 and Re_c =600) is relatively small compared to lower Reynolds number increments. This could suggest a plateauing effect, where beyond a certain Reynolds number, further increases in flow velocity contribute minimally to additional particle capture. The plateauing effect was observed for a smaller Reynolds number for regular arrangement scenario.

For the random arrangement of collectors, spatial variations in particle deposition on individual collectors were observed within the patch. This variation was influenced by factors such as the proximity of a collector to others, the wake structure, and preferential flow paths. Figure 3.15 (please see the end of the chapter for this figure) shows the flow field for an intermediate Reynolds number of $Re_c = 279$ (Fig. 3.15a), along with the spatial distribution of deposited particle counts across collectors in the patch (Fig. 3.15b) and the deposition rate for selected collectors (Fig. 3.15c). As shown, some collectors, like collector 32, are located within the wake of an upstream collector, resulting in fewer particles deposited compared to collectors that are more isolated or have adequate spacing from upstream collectors.

Figure 3.16 illustrates the same Reynolds number of $Re_c = 279$ at the highest vegetation density λ =0.15 (please see the end of the chapter for this figure). Here, particle distribution on the collectors appears more uniform, and the flow field suggests that higher vegetation density promotes more distinct preferential flow paths within the patch (Fig. 3.16a). These paths can cause particles to impact collectors at varying angles, leading to deposition on different sides of the collectors in different regions of the domain.

Purich, in his laboratory experiments with randomly arranged collectors, attributed the discrepancy in the capture efficiency of stems to the Strouhal number (Str). In his experiments, the highest Str values were observed for intermediate vegetation densities. However, the current numerical model indicates that the highest Str values were obtained for the highest vegetation density, for both regular and random arrangements of collectors, consistent with the findings of Stoesser et al. (2010).

Our particle capture efficiency results similarly show that the highest vegetation density corresponds to the highest patch-averaged efficiency, suggesting a positive correlation between the Strouhal number and patch-averaged capture efficiency. Additionally, as shown in Figure 3.8, there is greater variation in Str values between collectors within the patch for lower Reynolds numbers and lower vegetation densities. This variation is further examined in Figure 3.17, which plots Str variations alongside variations in the number of particles deposited on collectors for λ =0.035 and $Re_c = 115$. The figure demonstrates that fluctuations in Str are often in phase with the distribution of particle deposition on collectors. For the same patch, as the Reynolds number increases, the variations in Str between collectors decrease, and the particle deposition becomes more uniformly distributed. This suggests that the vortex shedding frequency, reflected in the Strouhal number, is a significant influencing factor in particle distribution within the patch, particularly as vegetation density increases.

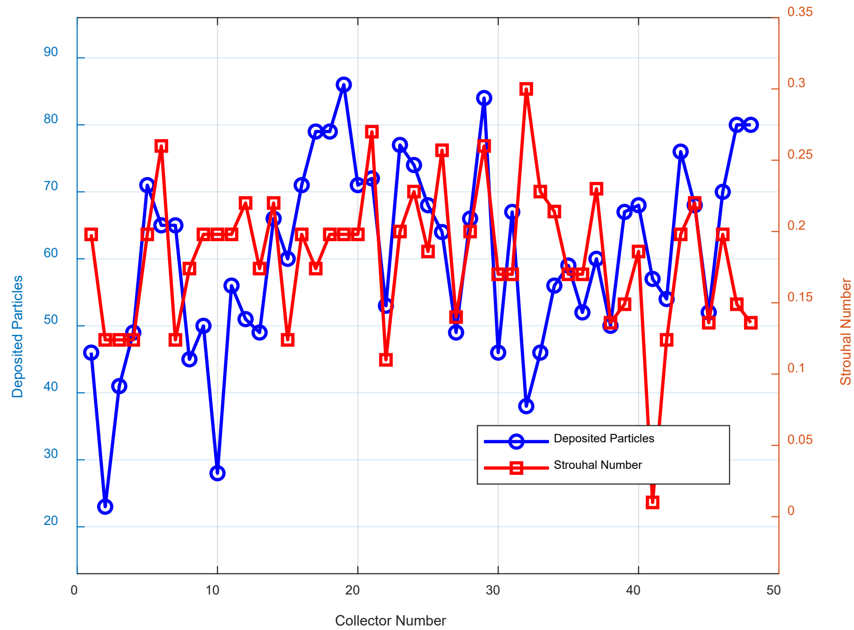

Figure 3.17. Variation of number of particles deposited on 48 collectors within the patch (Blue line) with λ =0.035 and $Re_c = 115$ and the corresponding variations in Strouhal numbers across collectors (Red line).

Similar to the regular arrangement case, particles could get deposited at the rear side of the collectors in random configuration as well. Figure 3.18 illustrates the percentage of particles deposited on the back of collectors within the patch, relative to the total number deposited on collectors, for each stem density in the random configuration of collectors. As shown in the figure, the percentage of particles attached to the rear of the collectors rises with increasing Reynolds number until it is nearing a plateau with an equilibrium state, where the back of each collector stabilizes in its capacity to capture particles regardless of further increases in Reynolds number. Moreover, higher vegetation density appears more effective at guiding particles to the rear of collectors, enhancing their attachment.

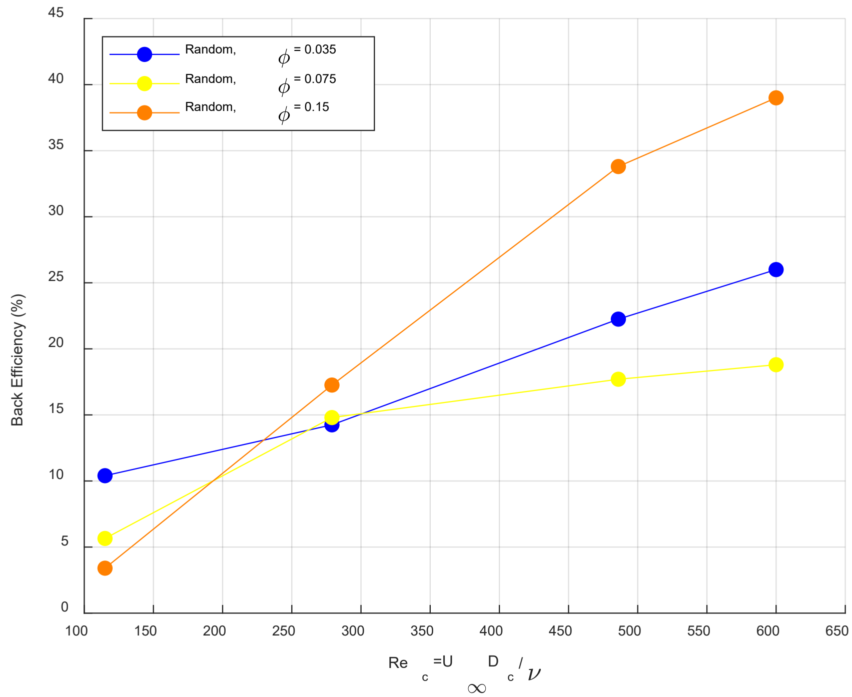

Figure 3.18. The back efficiency of the collectors in the random arrangement. The back efficiency is here defined as the total number of particles deposited in the back of collectors across the patch divided by the total number of particles captured by the collectors. Results are for high stem density (λ =0.15) , intermediate density (λ =0.075) and, low density (λ =0.035).

Purich (2006) calculated the capture efficiency of a collector within a patch using a formula derived from Palmer et al. (2004) for single-collector efficiency in an infinite domain. To sample particles on collectors, he placed four equally spaced dowels in a row across the channel width. He used the following formula to calculate attachment efficiency on each sampling dowel:

$$\frac{dN_c}{dt} = \eta P u D_c W_c \tag{3.2}$$

Where N_c is the number of particles captured during time t on the collector, η capture efficiency, P number of particles in unit volume, u approaching velocity to the collector, D_c collector diameter, and W_c collector width. He assumed that P is fixed during time t and equal to the initial number of particles in his experimental flume. He also assumed that u is fixed equal to average flow velocity. However, considering the complexity of the flow field shown in Figures 3.14 and 3.15, this formula may be less applicable when particle impacts on the collector from different angles. Additionally, spatial variation in particle concentration within the patch raises questions about the reliability of using equally spaced dowels for sampling in such a dynamic system.

Fauria et al. (2015) also used a similar formula as 4.2 by assuming that the time rate of concentration in a system including the stems is balanced with the rate of the concentration lost to the collectors or stems inside the system, rate of settling of the particles on the ground, and re-entrainment of the particles back to the system from stems. This balance also assumes that particle in the whole patch start accumulating particles with the same rate. Our simulations showed that particle capture rate depends on the position inside the patch, and also particle relative size, so that some collectors may get filled with the capacity of receiving particles faster than other collectors.

For our own specific problem of particles entering a patch of vegetation, it was assumed that a patch-level efficiency provides a smooth representation of this variation, offering practical insights into particle capturing mechanisms within a saltmarsh patch.

Conclusion

This chapter presented an analysis of particle attachment within a patch of emergent vegetation using CFD-DEM techniques, considering both regular and random arrangements of cylindrical collectors. The study showed that patch-averaged particle capture efficiency was highest for the densest case ($\lambda = 0.15$). This enhanced efficiency likely results from the close proximity of collectors, which not only increases available surface area for attachment but also induces higher vortex shedding frequency, enhancing particle mixing and transport within the flow. The maximum capture efficiency observed was 2.5% for both regular and random arrangements.

There was also rear attachment of the particles which was significant for the higher vegetation and Reynolds number. This can also be due to stable vortices, high vortex shedding frequency, and lateral proximity of collectors for guiding the particles at the wake of collectors by combined these effect making them prone to be pulled back by the eddies for deposition on the rear side of the collector. The maximum back efficiency i.e. percentage of particles deposited at the rear side to total particles deposited on collectors were around 35% for both regular and random arrangement scenarios.

The insights from this chapter underline the impact of vegetation density on sediment capture and suggest that denser vegetation patches may optimize particle retention, particularly under turbulent flow conditions. Future studies could explore additional environmental factors such as unsteady flow conditions, variable particle sizes, and variable adhesion properties of collector surface. The latter could be indicative of correlation between patch efficiency and different stages of biofilm formation on the collectors.

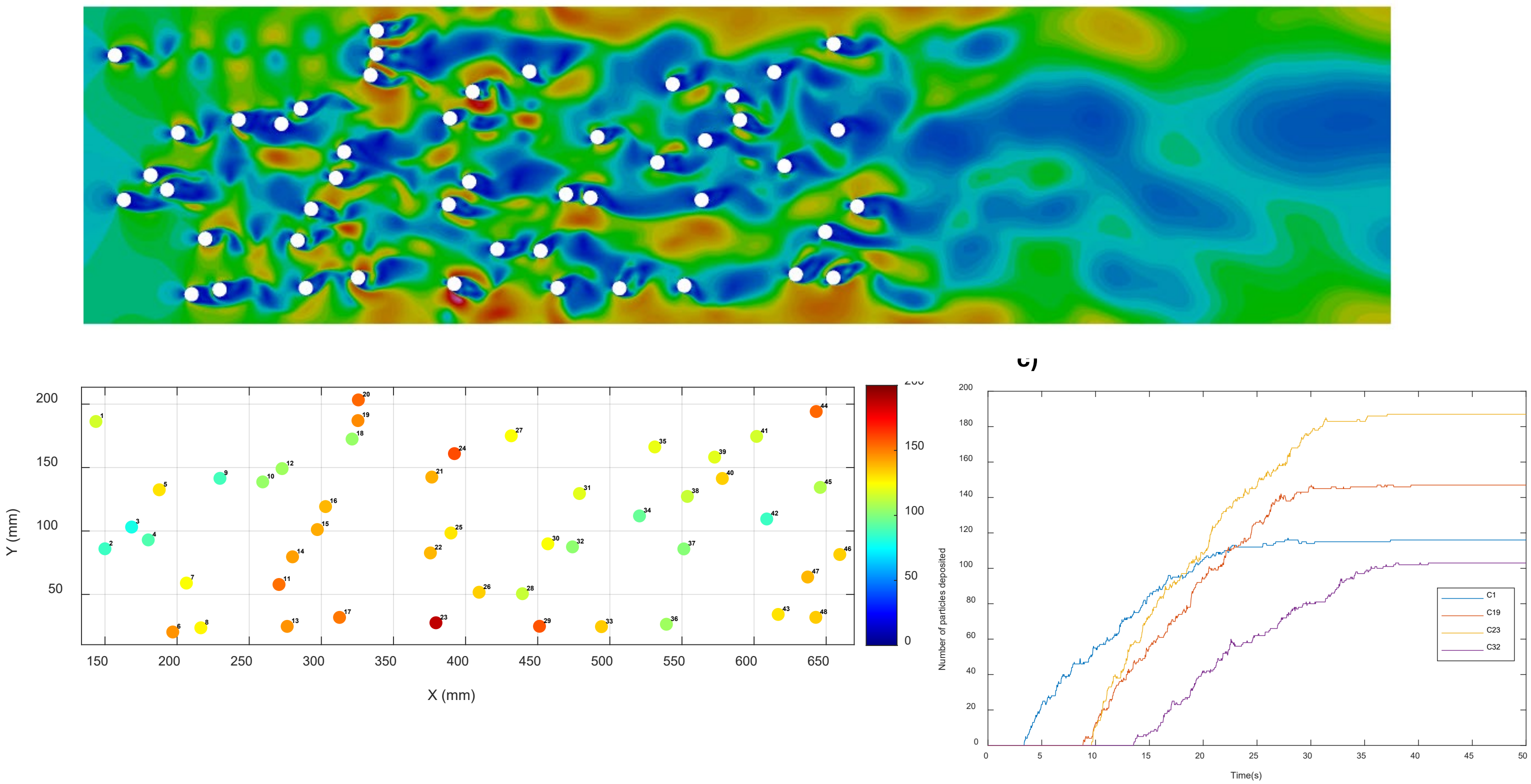

Fig. 3.15**.** Flow field (a), spatial variation of collector attachment efficiency represented by the contour plot of particle count on collectors (b), and time variation of particle attachment to selected collectors (c). The vegetation density is λ =0.035, and the Reynolds number is $Re_c = 279$. In plot (b), numbers indicate collector positions within the domain, while the legend in (c) corresponds to these collector numbers.

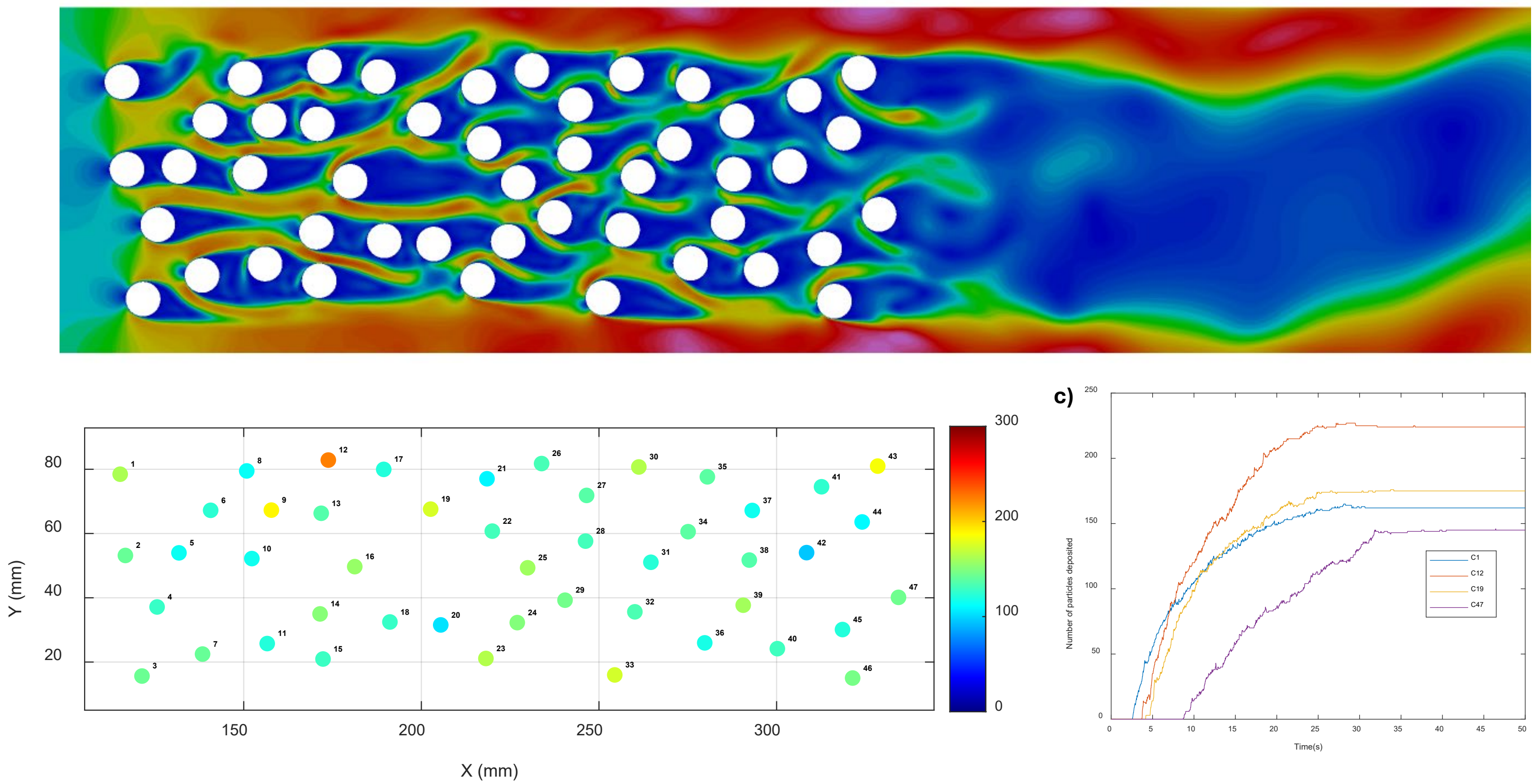

Fig. 3.16. Flow field (a), spatial variation of collector attachment efficiency represented by the contour plot of particle count on collectors (b), and time variation of particle attachment to selected collectors (c). The vegetation density is λ =0.15, and the Reynolds is $Re_c = 279$. In plot (b), numbers indicate collector positions within the domain, while the legend in (c) corresponds to these collector numbers.

Chapter 4: Laboratory observations on fine sand winnowing from an immobile rough substrate

Abstract

Introduction of fine sand into gravel-bed rivers has surged tremendously as a result of human activities. The ecological concerns for river habitats have called for suitable management strategies for cleaning these particles from gravel bed rivers. This paper is concerned with determining movement threshold of fine sand initially entrapped in the spaces between large immobile elements resembling a coarse riverine substrate with flow depths comparable to non-erodible element sizes. Static equilibrium condition was reached during an experimental run by maintaining a zero-supply condition for sand. It was assumed that the flow condition corresponding to this sand level was representative of critical conditions for onset of sand motion. A nonlinear regression curve was fitted between the level of the sand and associated critical shear stress. The flow field measurements using an ultrasonic Doppler profiler delineate main features of the shallow flow over large roughness elements such as sharp velocity gradients near the crest of the immobile elements, and also a deviation of instantaneous velocity probability density function from normal distribution very close to the sand level.

Introduction

An increase in frequency of natural catastrophes such as wild fires and floods, and direct human activities such as road construction, urbanization and agriculture have introduced large amounts of sand into rivers. This has led ecological consequences for river habitats to an alarming level; Among the impacted habitats are spawning salmonids which usually choose coarse bed rivers as their nesting sites (Leonardson, 2010); The local flow conditions, clean gravel, and shape of the redd (depression created by female salmon using tail and body) drive water through the nest, supplying dissolved oxygen and removing metabolic wastes. The sealing of pores of the coarse gravel elements due to sand intrusion reduces the permeability of the redd, and subsequent filling with finer particles lead to oxygen depletion for embryos. Wood and Armitage (1997) reported that a decline in solved oxygen due to coal mining resulted in one hundred percent death of salmon embryos in south Wales. Also, fine sediment was considered a major cause of the severe reduction of trout salmons in UK chalk streams (Accorny and Sear, 1999). Releasing an artificial flood from dam reservoirs is a strategy for removal of the fine sand. Usually, there are two methods of flushing; one is "surface based" in which the sand is only removed without entraining the gravel underneath; The other type is "subsurface flushing" that is intended to pull out sand from deeper bed, and this is usually accompanied with destroying the structure of the bed.

The process of entrainment of sand from interstices of an immobile substrate into the flow requires consideration of several contrasting processes (Grams and Wilcock, 2007); First, the surface area of the bed available for entrainment is reduced for the sand fraction. Second, when the sand particles lie in the interstices of gravels, they are shielded by the protruded elements against flow impingement on bed; and third, the turbulent wakes around the immobile elements give rise to local erosion of the sand. Limiting the discussion to surface flushing and bedload transport only, we need to find the minimum discharge which would be necessary to mobilize fine sand at a certain level below the crest of the gravel elements. Usually, there are two approaches for formulating a bedload transport equation; The first is a deterministic approach in which the rate of transport of the particles is expressed as a function of excess shear stress. In this approach, particles are assumed to get into motion when the time-averaged bed shear stress exceeds a particular value called critical bed shear stress. This is usually derived from the Shields diagram. The second group of formulations of bedload transport rate is through a stochastic expression of the instantaneous forces on individual or ensemble of particles. Einstein was the first to pioneer a probabilistic method for prediction of bedload transport rate (Dey, 2014).

Deterministic bedload transport formulas such as Meyer Peter and Mueller (1948) are still widely used for their practicality and ease of parameterization. Since they have been only devised for particles of uniform size on the bed, they need to be modified to be applicable to a non-uniform mixture of particles. Therefore, deterministic sediment mixture transport formulas have been formulated based on modification of Shield's critical shear stress to compensate for the more energy needed by the flow to move particles hidden in the lee side of larger particles. A modification of Mayer-Peter formula using a hiding function for bedload transport rate of fraction D_s in a mixture of particles on bed surface reads as (Kleinhans and Van Rijn, 2002):

$$\phi_{b,s} = p_s \alpha \left(\theta'_s - \theta_{cr,s,corrected}\right)^{1.5} \tag{4.1}$$

$$\theta_{cr,s,corrected} = \xi_s \theta_{cr,D_s,Shields} \tag{4.2}$$

where $\phi_{b,s}$ is a dimensionless bedload transport rate ($q_{b,s} = \rho_s \Phi_{b,s}.\sqrt{(s-1)g}D_s^{1.5}$), p_s surface fraction of sand D_s, θ'_s grain shear stress for D_s, $\theta_{cr,s,corrected}$ corrected dimensionless critical bed shear stress for grain size D_s, ξ_s hiding factor for size fraction D_s, and $\theta'_s = \tau'_s/(\rho_s - \rho)gD_s$ dimensionless grain shear stress for the sand. Several hiding factors have been introduced in the literature; among them the theoretical formula of Egiazarrof (1967), and empirical formulas by Parker et al. (1982), and Wilcock and Crowe (2003). Parker (2008) brings a full account of various hiding factors and their calculation procedure. The hiding factor provided by these researchers usually belongs to cases where all surface particles are moving together, are in the same size order, and their sizes are small fraction of total flow depth. There might be specific situations that do not meet these assumptions. For example, downstream dams, the river bed comprises of elements that may remain immobile, and their interstices are frequently filled and depleted by fine sand. Partial transport formulas are needed for these sediment mixtures. Also, in mountainous regions, the flow depth is in the order of size of the underlying elements. In this condition, the logarithmic velocity profile may not be valid (Yager et al., 2007), and different resistance laws have been used by researchers like Bathurst (1985). Kuhnle et al. (2013) examined the viability of a two-fraction mixture sediment transport rate formula proposed by Wilcock and Kenworthy (2002) to quantify the fine sand transport rate through and over immobile elements with large size discrepancy. Compared to experimental results, they concluded that Wilcock and Kenworthy's formula overpredicts and underpredicts experimental observation depending on the level of the sand below the crest of immobile elements. They attributed this discrepancy to larger values of reference shear stress in formula proposed by Wilcock and Kenworthy (2003) with respect to their observations. The reference shear stress is used in mixture transport formula as a replicate for critical shear stress, and is the bed shear stress for a very small discharge of the sediment that can be measured in a mixture transport experiment.

The study of sand erosion affected by non-erodible elements have been pursued both by aeolian and fluvial hydraulics researchers. Lyles et al. (1974) examined the effect of standing crops on protecting underlying soli from erosion. Using cylindrical and spherical non-erodible elements with various planting densities, they performed wind tunnel experiments to observe the sand erosion initially filling spaces between elements up to their height. A free stream velocity higher than the threshold velocity of the sand particles started the erosion, and it proceeded until a very low rate of sand could be measured exiting the tunnel. The stabilization of the sand surface was the result of appearance of the elements and their absorption of flow momentum which resulted in less momentum flux towards the sand surface, and ultimately stoppage of the erosion process under the imposed flow magnitude. Using a logarithmic velocity law, they calculate bed shear stress of the stabilized surface, namely the critical shear stress. They obtained a non-dimensional shear velocity that could be expressed as a linear or power law function of geometrical characteristics of the roughness elements i.e. the ratio of the height of the element to distance between them, and also number of elements per unit area. The same approach in obtaining the critical shear stress for the sand movement under effect of cubic non-erodible elements was done by Iversen et al. (1991). They performed their experiment in a wind tunnel under different concentration of roughness elements and concluded that power law can describe the variation of critical shear stress with the concentration of the elements. Ruapach et al. (1993) proposed a theoretical criterion for onset of motion of sand particles under effect of non-erodible elements based on his theoretical derivation for partitioning of total drag into form and skin components (Raupach, 1992).

In fluvial hydraulic, Yager et al. (2007) examined the bedload transport of natural sediment affected by presence of boulders in a steep channel with shallow flow depth resembling one in mountainous regions. They developed a theory for partitioning of the drag based on geometrical characteristics of spherical immobile elements. Implementing the part of the drag on the intervening surface into a conventional bedload transport formula such as Fernandez Luque and Van Beek (1976), they computed the equilibrium bedload transport rate for the mobile phase. They validated their experiments in a flume with immobile phase consisting of spheres of 30mm, and mobile particles of fine gravel with 3.7mm diameters. Their theoretical formula could predict the experimental observations with good accuracy with a maximum order of magnitude discrepancy with experimental data in some experiments. Grams and Wilcock (2007) performed experiments to propose a formula for entrainment into suspension of fine sediment initially trapped in the voids of an immobile substrate composed of diagonal arrangement of hemispherical elements. Their dimensional and experimental observations showed that the elevation of the sand below the immobile element crest should be directly considered in an equilibrium entrainment function of such flows, and implemented that as an adjustment factor in the entrainment function of Garcia and Parker (1991). Kuhnle et al. (2013) conducted flume experiments for the quantification of equilibrium bedload transport of fine sand moving through and above immobile natural gravel elements. They surmised that the shear stress on the surface of mean sand level can be calculated as a linear fraction of the total be shear stress on the crest of the immobile phase:

$$\tau_{*s} = A(z_s) \times \tau_b \tag{4.3}$$

The proportionality factor namely $A(z_s)$ was named as roughness geometry function from Nikora et al. (2001, 2007). It can be calculated as:

$$A(z_s) = \frac{A_s(z=z_s)}{A_s(z=z_s)+A_g(z=z_s)} \quad (4.4)$$

where $A_s(z = z_s)$ and $A_g(z = z_s)$ are the planar areas of the bed covered by sand and gravel respectively. In fact, the roughness geometry function is equal to the cumulative probability distribution of bed fluctuations whose importance in the quantification of sediment mixture transport has been brought by Parker (2008) and the references therein. Kuhnle et al. (2013) assumed that the roughness geometry function can be used effectively as a scale factor for the the distribution of total shear stress below gravel crest. They proposed a formula to estimate the fine sand transport rate from their experimental observations:

$$\phi_{b,s} = \frac{q_{b,s}}{[(s-1)gD_s]^{0.5}\rho_s D_s} = 2.29 \times 10^{-5}[A(z_s)]^{2.14}\left(\frac{\tau_b}{\tau_{cs}}\right)^{3.49} \quad (4.5)$$

τ_b is the total bed shear stress, τ_{cs} is the critical shields stress for the sand when covering the crest of the gravels, D_s is the diameter of fine sand, ρ_s is the mass density of the fine sand, and $A(z_s)$ is the roughness geometry function at the mean sand level calculated from equation 4. Kuhnle et al. (2014) extended their experiments to equilibrium fine sand bedload transport over larger cobble bed and concluded that the general format of the formula (4.5) could be preserved, but the exponents need to be changed to fit their new observations. In another investigation, Kuhnle et el. (2016) sought the maximum erosion depth of sand from interstices of immobile gravel elements. The sand in each experiment initially filled the voids of larger elements up to their crest, and no sediment was supplied into the channel. The erosion of the sand continued until no sand was running out of the flume anymore. They estimated the shear velocity of the new sand level with the formula (4.3) and assumed that the erosion of the sand proceeds until the shear velocity in the gravel was equal to the fall velocity of the sand times a constant. By calibrating this constant from experimental data, they could calculate the maximum clean out depth from the combination of formula (4.3) and inverse of cumulative probability distribution of the bed fluctuations. Stradiotti et al. (2020) proposed another formula with assuming that the maximum erosion depth is a power law function of excess shear stress (existing bed shear stress at the crest level minus critical bed shear stress at the crest level). The constant coefficients of their formula were found from experimental data of non-equilibrium entrainment of sand into suspension.

The common feature of all the above reported investigations is inclusion of roughness characteristics of the immobile phase into the transport rate of the mobile phase. The effect of the arrangement and proximity of the obstacles is a controlling factor in trailing vortices, hence mass and momentum transfer in the bed region (Iversen et al., 1991). One of the factors that need more attention in sediment transport in fluvial environments is the relative submergence or the depth of fluid divided by size of the immobile element. All the mentioned investigations were dedicated to flows with high relative submergence, whereas for mountainous rivers, the depth of the flow may be in the order of magnitude of grain size. The significance of relative submergence, and its effect on flow hydrodynamics has been elucidated by Nikora et al. (2001,2007). According to Nikora (2001), the flow over a rough substrate can be divided into several subregions along the vertical and depending on the degree of perturbation of flow by roughness elements, these subregions may or may not exist. Spatially averaging of the Reynolds Averaged Navier Stokes (RANS) equations, they derived a new set of equations which include new terms of form induced stresses and pressure drag in the momentum equations. Spatial averaging is performed in two steps. First, the Navier stokes equations that fully describe the motion of flow over rough bed are averaged in time which is conventionally called Reynolds-average Navier Stokes equations (RANS), and in the next step, the time averaged variables are averaged spatially on a very thin plane parallel to the bed. This plane will be continuous above the crest elements, and disconnected below the gravel crest. According to Nikora et al. (2001), four subregions can be recognized: An interfacial subregion between roughness crests and troughs; a form induced sublayer in which form induced stresses have appreciable significance; a logarithmic region where form induced stresses start to vanish and a typical overlap region similar to that in hydraulically smooth flows develops; and finally, an outer flow region that is affected by free stream velocity rather than near bed velocity scales. For high relative submergence flows over a rough bed, the four sublayers coexist. However, for very shallow flows, only the first two sublayers near the bed may form. Bayazit (1982) examined the threshold behavior of a sphere in a very shallow open channel flow over very rough bed and observed that the non-dimensional Shields stress parameter increased from 0.04 up to 0.12, when the relative submergence was reduced to 3.3. The effect of relative submergence on threshold shear stress of uniform and mixture particles was also investigated and proved by Shvidchenko (2000). Bayazit and Denker (1980) reported that bed load discharge for a particle on a very rough channel may reduce up to thirty times when the relative submergence fell below five. Examining the turbulence structure in an experimental flume with natural gravel bed, Mohajeri et al. (2015) examined the turbulence structure of flows with intermediate submergence ratio (7.5-10.8) and identified various flow features such as cellular secondary currents, and coherent structures exhibiting themselves as upward fluid motion in the upstream face of the gravel particles and downward motion of fluids at the lee sides of particles, respectively. In another paper, Mohajeri et al. (2016) elucidates how the sweep and ejection events from coherent structures can lead to lifting of the particles in the interstices of gravel bed elements.

This paper is aimed at

- Presenting laboratory experiments for estimation of bed shear stress for threshold of movement of sand at various levels below immobile roughness elements. Deterministic bedload transport formula should be corrected for when sand is protected by the larger elements. Little data exist in the literature for low submergence ratio flows. The experiments of Yager et al. (2007) address the problem, but the size ratio between the mobile and immobile phases is limited to around 0.1, and also all the experiments were performed for supercritical conditions.

- Presenting flow field measurements using Ultrasonic Velocity Profiler (UVP) at the critical condition of the bed. The unique property of the UVP is its non-intrusive nature. The measurements in very shallow flow depths is almost impossible with intrusive instruments such as ADV (Acoustic Doppler Velocimeter). We were able to measure the instantaneous velocity profiles whose time and spatially averaged quantities are reported here.
- Testing various drag partitioning approaches and compare them to direct numerical simulation (DNS) results from the literature.

Methodology and Materials

Our experiments were designed based on the same ideas of Lyles et al. (1974), Iversen et al. (1991), and Kuhnle et al. (2016). The immobile elements are covered to the crest by fine sand, and a flow is set in a channel. Then, erosion of the sand layer begins, and in time, the level of the sand drops below of the immobile elements crest. By maintaining a uniform flow during the erosion process, the movement of sediment proceeds to a level for which threshold condition can be assumed. The laboratory experiments were conducted 600 cm meter long, 40 cm wide, water recirculating open channel flume with Plexiglas side walls (figure 4.1). Water was pumped from an underground storage tank. A magnetic flow meter was used to control the discharge magnitude into the channel. At the entrance of the channel, a distilling tank and flow straighteners were used to guide the flow smoothly into the channel. The immobile substrate was prepared using two layers of spherical plastic balls with diameter of 50mm. An aluminum rod was used to pierce a hole in a wooden plate attached to the flume bed on one side. The steel rod was perforated through the plastic balls on its other side to keep them firm in the main channel. The pores of the first 120 cm of the flume were filled with crushed gravel particles so that it is ensured that fully developed flow condition prevailed in the working section. Because of the length of the channel, usually a tailgate was needed to establish uniform flow conditions. Uniform sand of 0.5 mm diameter was used as the transported material. Three sets of experiments were performed for three different bed slopes.

Several longitudinal sections can be identified in a typical non-equilibrium sediment transport experiment. Just downstream of the rigid apron and at the beginning of the movable bed region, a pit usually formed whose length is called a “saturation length”. A fluid vortex governs the flow field in this region. After that, an “equilibrium region” is formed in which the sediment transport rate reaches an equilibrium with the transport capacity of the imposed flow. All measurements and observations during the experiments are reported for the equilibrium region, and no attempt was made to record bed geometry or flow features in the saturation length region. Another feature of non-equilibrium sediment transport in the experiments was evidence of formation of barchan dunes. This happened at the beginning of the experiments when the sand completely filled the voids up to the crest of the spheres. Table 4.1 shows the total combination of parameters for the laboratory experiments. In this table, the flow depth H is indicating the height of the water above the crest of the elements. Average velocity is based on $U_{ave} = Q/BH$ in which Q is the total discharge measured by the flow meter, H is the water depth on the crest, and B is the width of the channel. The bed shear velocity is computed as $u_* = \sqrt{gHS_0}$ in which g is acceleration due to gravity, and S_0 is the slope of the channel at the crest of the spheres. The flow depth ranged between 13 and 78 mm giving a minimum aspect ratio (The width of the channel divided by the flow depth over crest) equal to 5.13.

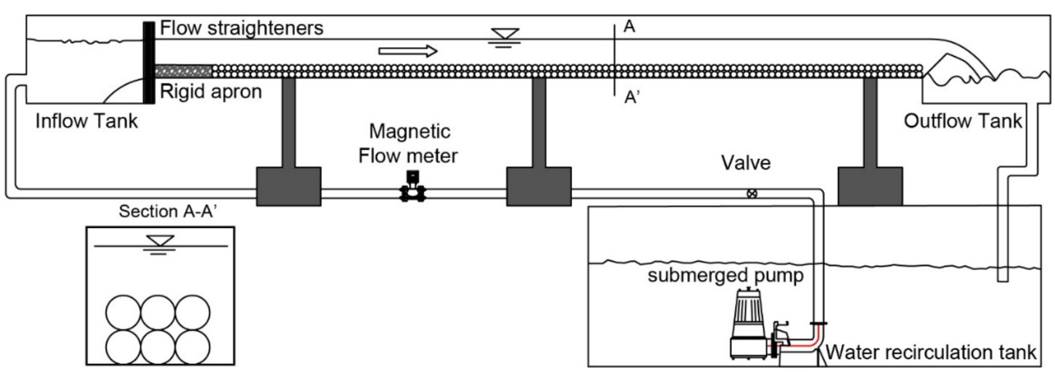

Figure 4.1. scheme of the experimental flume.

At the beginning of each experimental run, the substrate was filled up to the crest of the immobile elements. No sediment was supplied from upstream, so only sediment was transported due to bed degradation. The range of the discharges and sediment sizes were chosen to ensure that sediment particles were in frequent contact with the bed. Each series of experiments was started by setting a low steady discharge, and uniform flow was established during initial stages of the experiment by adjusting the tailgate. In a typical experiment, the sediment discharge was declining exponentially in time until it reached almost 1% of that at the beginning of the experiment. In this condition, it was assumed that the bed had reached a "static equilibrium" for which a threshold bulk shear stress can be assigned for that specific flow and geometrical conditions. After reaching the static equilibrium, the flow field was measured using an Ultrasonic Velocity Profiler (UVP), the water was allowed to drain, and the bed topography was captured using a laser scanner. These steps completed the data recording for a run. Another run of the experiment was established by the next higher discharge. This brought the sand level lower and to a new equilibrium condition. Figure 4.2 shows planar photos of the bed during the degradation stage and a typical transport rate variation during one experiment.

Results and Discussion

Bed level changes

A laser scanning of the bed was performed as the bed reached the final stage of erosion at the end of each experimental run. The area of 1000mm in 350mm was selected for scanning. The recording interval of the scanner was 1mm in longitudinal direction and 1mm in traverse direction.

Table 4.1. list of variables and their variations in experiments

$Slope$	$Q(l/s)$	$H(mm)$	$U_{ave}(m/s)$	$\tau_0(N/m^2)$
0.002	2.25	22	0.256	0.432
0.002	5.07	38	0.334	0.746
0.002	7	55	0.318	1.079
0.002	10	66	0.379	1.295
0.002	12	78	0.385	1.530
0.005	2	18	0.278	0.883
0.005	4	28	0.357	1.373
0.005	6	40	0.375	1.962
0.005	8	48	0.417	2.353
0.008	1.5	13	0.288	1.020
0.008	3.25	27.6	0.294	2.166
0.008	6.5	51.8	0.314	4.065
0.008	13.82	65	0.532	5.101

Figure 4.3 shows configuration of the bed from the laser scanner, the probability distribution function of the bed elevation, and cumulative probability distribution function or roughness geometry function. As shown in the picture, the PDF of the bed level elevation is changing from normal distribution at the beginning of the experiments when the substrate is filled up to the crest, to a bimodal distribution as the sand is eroded from the interstices. The bimodality increases as the sand level

goes down for higher discharges. The roughness geometry function experiences an inflection when crossing from one modality to the other. The slope of this transition line reduces as the bimodality increases when sand level reaches deeper depths below the crest of non-erodible elements.

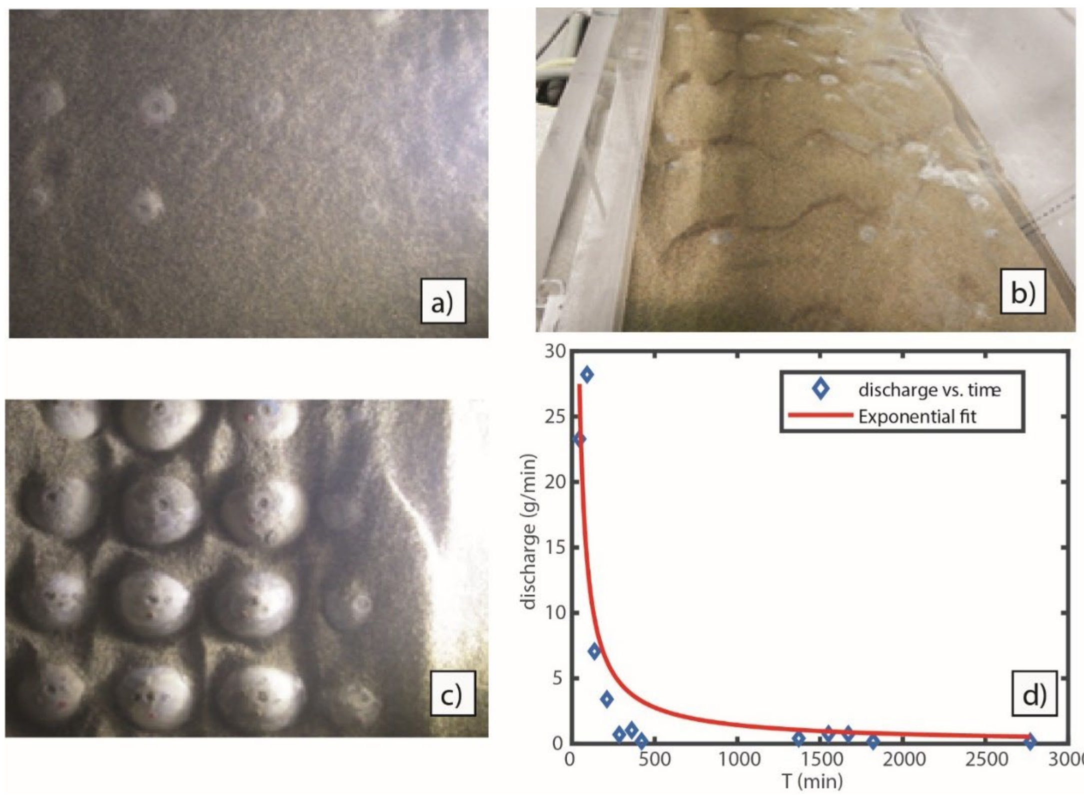

Figure 4.2. photos illustrating a typical experiment starting with sand covering the immobile elements at the beginning of the experiment (a); bed in erosion stage (b); and equilibrium stage (c); a typical variation of fine sand discharge (grams per minute) in experimental time (minutes) can be seen in (d).

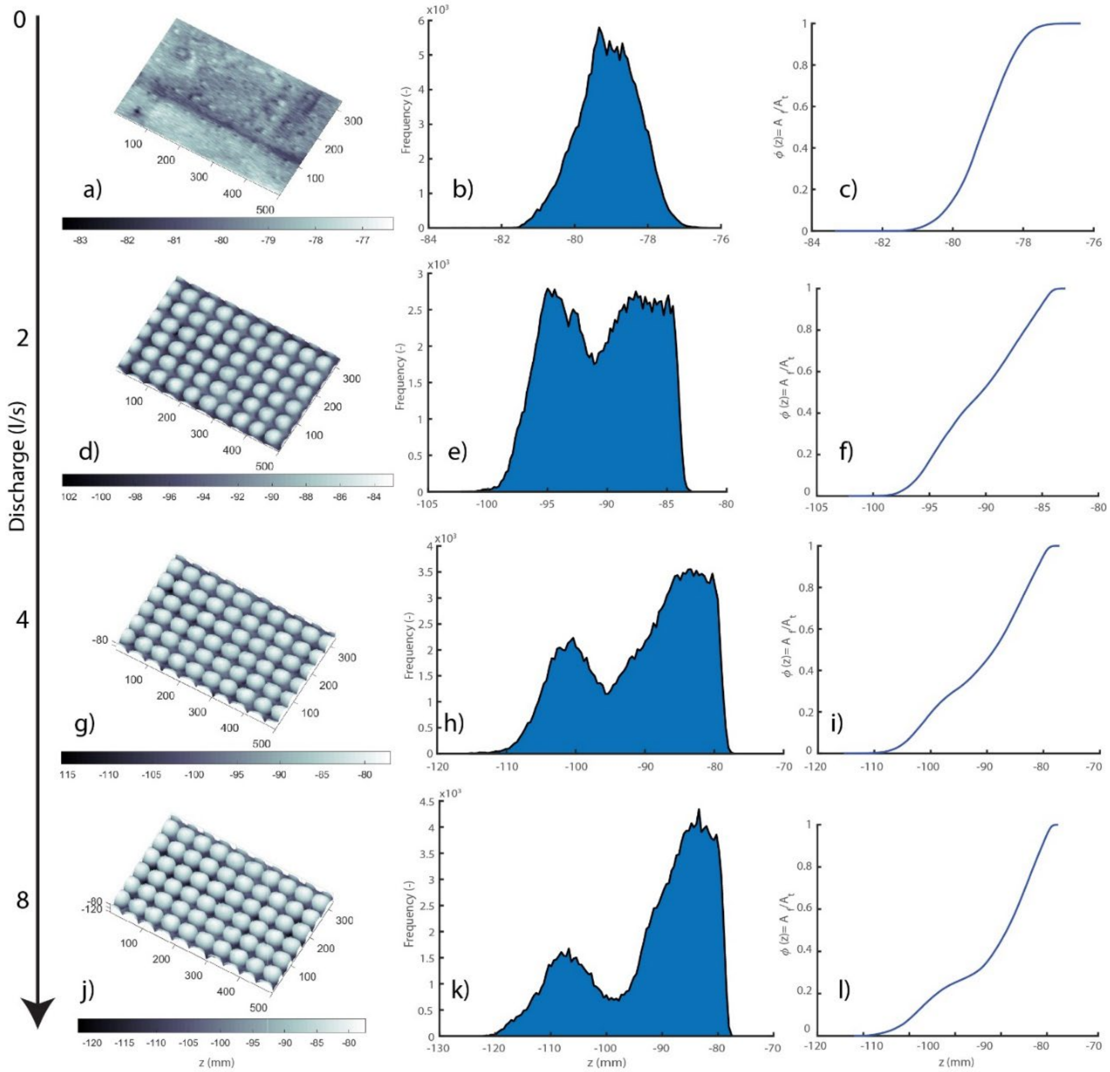

Figure 4.3. The probability density distribution of the bed elevation measured using laser scanner for the beginning of the experiments, and discharges equal to 2, 4 and 8 lit/s. (a, d, g, j) shows the profile of the bed for each discharge respectively; (b, e, h, k) show the probability distribution of bed elevation; (c, f, I, l) shows the roughness geometry function for the named discharges in static equilibrium condition. The slope of the bed is S=0.005.

Flow field measurement

One of the main challenges in the quantification of sediment transport in high gradient gravel bed rivers is dealing with shallow flow depths of the order of the size of the gravel elements. These ranges of depth happen in the roughness sublayer, and velocity distribution and friction factor are completely different from that of the same stream with much more submergence depths. Especially in the configuration of our experiments, even the minimum depth of 20mm caused an erosion depth of comparable magnitude below the crest. Therefore, besides perturbation of roughness elements into the flow depth above the crest, there is also an interaction of the surface and subsurface flow regions giving rise into a mass and momentum exchange.

An Ultrasonic Velocity Profiler (UVP) was used for recording the velocity field. UVP is able to measure the instantaneous one-dimensional velocity along a line. An ultrasound pulse is emitted from a transducer into the liquid, and the same transducer receives the echoes which originate from tracer particles suspended in the fluid. More details of the working principle of a UVP can be found in Takeda (1995). UVP is very useful for its almost non-intrusive advantages, and also the fact that we had very shallow flow which makes applicability of other instruments such as Acoustic Doppler velocimeter (ADV) impossible. Velocity profiles were recorded on a grid comprising of nine points as shown in figure 4.4. The minimum elevation on the sand layer that could be captured varied between points due to the microtopography of sand layer. Usually, the emitted pulse from the UVP had intersections with these points on the bed with elevations above the average elevation. The recording time of the velocity data was almost four minutes to effectively produce stationary time series of velocity data. An approximate criterion $\eta u_* / \nu \geq 50$ (Bandyopadhyay, 1987) ensured that all the measurements are in fully rough, turbulent flow conditions. η is the vel of the sand below crest, and u_* is the bed shear velocity.

Figure 4.4 shows the time-averaged velocity profile for three different sets of experiments i.e. Q=4l/s, Q=6l/s, and Q=8 l/s for a constant bed slope of S=0.005. The vertical axis shows the elevation from the crest of the spheres (mm) and the horizontal axis shows the time averaged longitudinal velocity (mm/s). In all three discharges and above the crest, there is a sharp gradient in velocity profile on the crest of the sphere following a segment with lower gradient. Below the crest, the velocity distribution can be both linear (Q=4l/s) and exponential (Q=6l/s, Q=8l/s). This substantiates the role of fluid flow below the crest which must be considered for quantification of mass and momentum transport in integrated shallow water equations and sediment conservation equation.

Figure 4.5 shows the spatially averaged flow velocity above crest for the three discharges whose local velocity distributions were reported in figure 4.5. Recently, spatially averaged representations of the flow field equations have been proven useful for flows with heterogeneous beds. Rooted in porous media research, they have found their path toward flow over rough surfaces in hydraulics (Nikora et al., 2001). Flow field statistics near the bed have important implications for sediment transport formulations. Usually, the probability density function of near bed flow variables such as instantaneous velocity distribution and instantaneous bed shear stress distribution are used in formulating the pickup probability of bedload formulas, and threshold criterion analysis. Figure 4.6 shows the PDF of instantaneous streamwise velocity component for different regions of the flow along the beam of the UVP. As figure 6 shows, in most of the flow depth, the normal PDF prevails. However very close to the bed, the PDF is deviating from normal distribution, and a stable distribution could be fit to the PDF curve. This must be considered in stochastic formulation of above threshold bedload transport formulas.

Critical shear stress

The pattern of sand erosion around and between the immobile elements was not uniform, so measurements of the erosion depth bellow the crest was averaged spatially in rows between elements. The spatially averaged erosion depth below the crest is plotted against the dimensionless bed shear stress $\theta_{critical} = \tau_{critical}/[(\rho_s - \rho)gd_s]$ in figure 7. On the vertical axis, the level of the sand below the crest η is non-dimensionalized with the non-erodible phase diameter D_g. The variations could be fitted with a Michaelis-Menten equation

$$\frac{\eta}{D_g} = \frac{a\theta_{excess}}{b+\theta_{excess}} \tag{4.6}$$

where $\theta_{excess} = \left(\theta_{critical} - \theta_{critical,surface}\right)$, $\theta_{critical}$ the dimensionless critical shear stress at sand level, $\theta_{critical,surface}$ dimensionless critical shear stress of the sand at the level of the crest of the non-erodible phase which was estimated using Shields diagram, $a = 0.989$, and $b = 0.06207$.

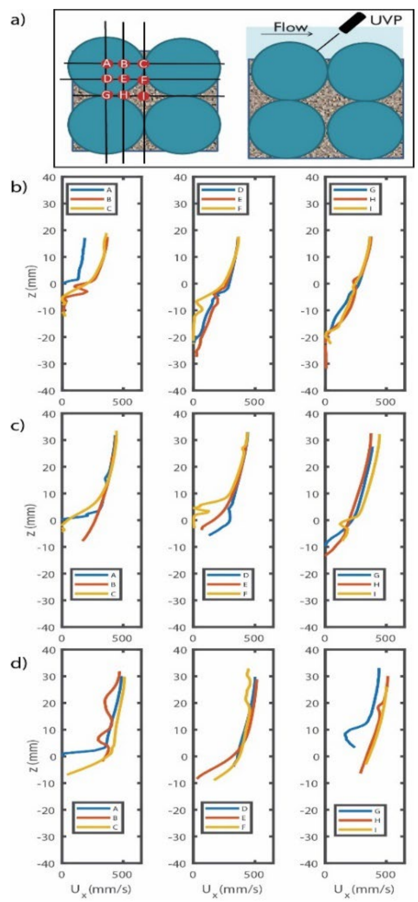

Figure 4.4. Time averaged velocity profiles for S=0.005 and three discharges of 4 l/s, 6 l/s, and 8 l/s (a, b, c, respectively); The grid for velocity measurement and points of recording profile of velocity is shown in (a).

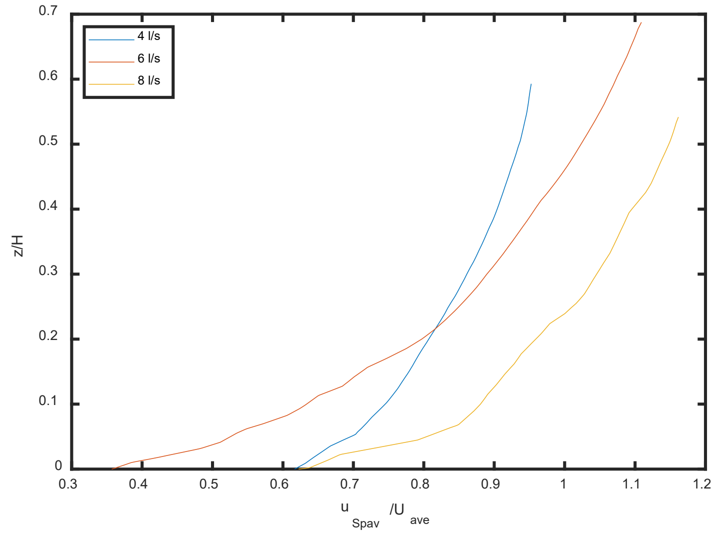

Figure 4.5. Spatially averaged flow velocity above the crest for Q=4, 6, 8 l/s and S=0.005. The horizontal axis shows the velocity magnitude nondimensionalized with cross sectional average velocity; the vertical axis shows the elevation nondimensionalized with flow depth over crest of the spheres.

Drag partitioning approaches

There is still much debate about the partitioning of the drag in complex rough wall flows. Various researchers have approached the problem of drag partitioning on rough substrates ranging from direct analysis of the governing equations (Nikora et al., 2019), and simple theoretical expressions validated by experiments (Raupach, 1992) to direct measurements of forces in the laboratory experiments (Wooding et al., 1973). The total drag τ_b can be divided into pressure drag term τ_R on roughness elements plus a skin drag term τ_s on the intervening surface between elements. The geometry, arrangement, proximity, and planar concentration of obstacles contribute to this distribution.

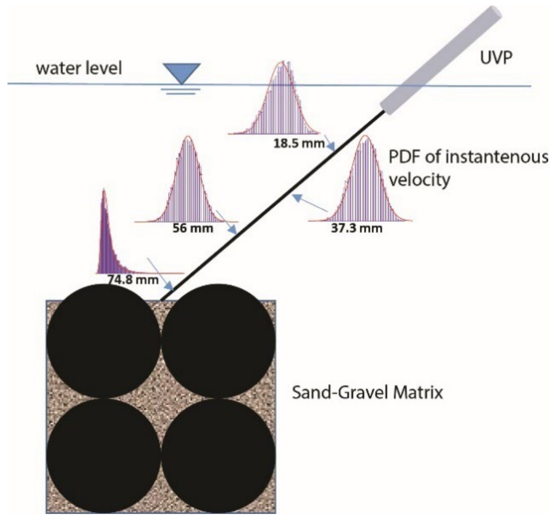

Figure 4.6. PDF of instantaneous velocity for the case of Q=6 l/s, H=40 mm, S=0.005, the total aligned distance of the tip of the probe to the sand bed is 76 mm (The numbers indicate distance from the probe).

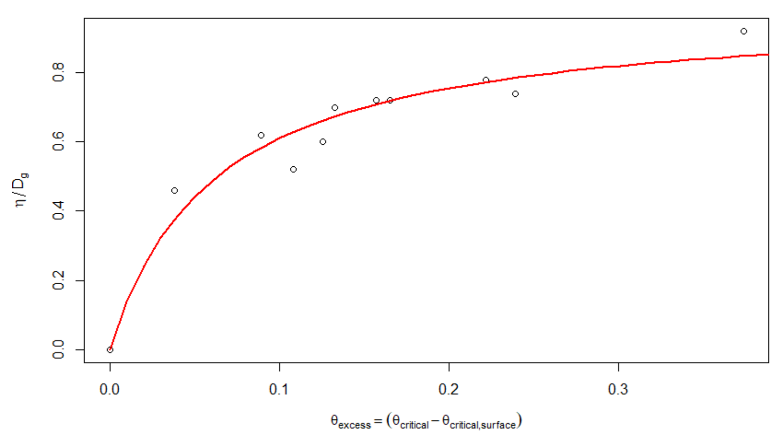

Figure 4.7. Non-dimensional critical shear stress versus non-dimensional sand level below crest. The red curve approximates this variation with a Michaelis-Menten equation ($\boldsymbol{R^2 = 0.97}$).

There are several drag partitioning approaches in the literature formulated for regular arrangements of cylinders, cubes, and spheres. These approaches for drag partitioning have been mostly formulated based on roughness density of the surface elements i.e. the total surface area of the elements projected on a vertical plane divided by the total horizontal surface area.

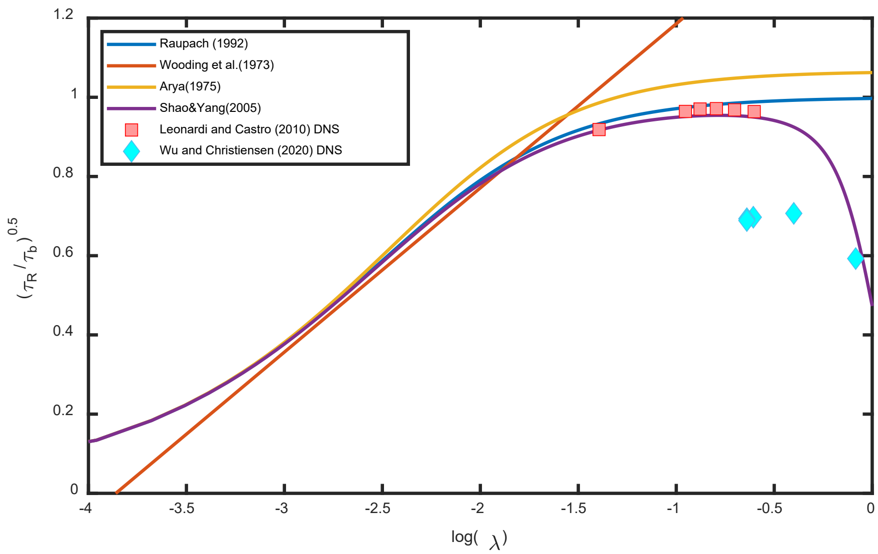

Figure 4.8. comparison of several drag partitioning approaches as a function of surface roughness density

Figure 4.8 shows the ratio of pressure drag τ_R to total drag as a function of roughness density (frontal area per unit ground area) for drag partitioning methods developed by Wooding et al. (1973), Arya (1975), Raupach (1992), and Shao and Yang (2005). All these approaches have been developed in meteorological community, and all except that of Shao and Yang (2005) consider a sparse distribution of the elements. For comparison, we have also included the relevant parameter from direct numerical simulations of Leonardi and Castro (2010) and Wu et al. (2020). As it is seen in the figure, the methods of Raupach (1992), and Shao and Yang (2005) are closer to the DNS data of Leonardi and Castro (2010) but departs from that of Wu et al. (2020), probably due to different obstacle shapes (cubes against hemispheres), Reynolds numbers, and flow regime (fully rough and transitionally rough). We could not assess the applicability of these drag partitioning approaches to our experiments. The drag partitioning of Kuhnle et al. (2013,2015) considers a multiplication of roughness geometry function $A(z_s) = \frac{A_s(z=z_s)}{A_s(z=z_s)+A_g(z=z_s)}$ and total wall stress to compute the shear at the sand level. This might be effective in cases where $A(z_s)$ at the mean sand level is a decreasing function of elevation but, for example, if the immobile roughness elements are cubes, this formula gives a fixed shear stress for all levels of the sand, or it only works for spherical elements to some certain depth. The range of Reynolds number $Re = \frac{U_{ave}h}{\nu}$ in our experiments lies between 3500 and 34000 (U_{ave} is the cross-sectional average velocity, h is the flow depth, and ν is the kinematic viscosity). The lower margin belongs to sand levels near the crest, and higher Reynolds numbers to deeper sand levels. This might result in a friction dominated flow for all our experiments, or at least for lower Reynolds numbers. This can only be clarified by conducting high resolution numerical modelling using DNS or LES (large eddy simulation) with considering all the bed undulations, because they contribute to form and skin drag. The recorded bathymetry can be input to the model, and velocity profile data captured by the Doppler profiler can be used for verification of the models.

Conclusion

The paper aims to understand the hydrodynamics and sediment transport phenomenon at the interface of immobile gravel substrate and the overlying shallow fluid flow. Several shortcomings of the previous approaches were discussed here:

- Most sediment transport formulas neglect the effect of relative submergence and concentration of the immobile phase of the bed materials. There are several deterministic and stochastic approaches for sediment transport calculations which neglect these aspects. Regarding stochastic approaches, most of them are based on normal PDF instantaneous velocity distributions while our preliminary observations show that there is deviation from Gaussian PDF for near bed velocities (Figure 4.6).
- We performed experiments to contribute to data for threshold behavior of the fine sand for implementing deterministic bedload transport formulas. A nonlinear regression curve fitted to the threshold shear stress data (Figure 4.7).
- Most of the drag partitioning approaches in the literature are devoted to sparse roughness densities, and they were shown to contradict with results

from Direct Numerical Simulation (DNS). A drag partitioning methodology based on physics of depth limited water flow on rough substrates is needed. A high-resolution numerical simulation which can adequately consider the bed undulations, and compatible with the recorded velocities is envisaged for our future research.

Chapter 5: Conclusion

Summary of findings of thesis chapters

This thesis investigated the complex dynamics of particle attachment and sediment entrainment in aquatic environments, focusing on interactions between sediment particles, flow, and rough substrates, such as vegetation stems and immobile gravel beds. Through computational and experimental studies, this research provides valuable insights into sediment transport processes that are critical for the design and management of marine and riverine ecosystems, particularly in restoration projects.

In **Chapter 2**, we examined the mechanisms governing the attachment efficiency of suspended particles to a single vegetation stem using a CFD-DEM model. By treating the stem as a cylindrical collector in a flow field, this study quantified how particles attach to the stem through direct interception, considering both perfect attachment and varying degrees of adhesive forces. These findings highlighted the sensitivity of particle attachment to factors such as Reynolds number, particle size, and surface adhesion, providing a baseline for understanding sediment retention on individual vegetation elements.

The findings of this chapter suggest that while a very high surface energy on the collector keeps particles in place upon their first collision, a slightly lower surface energy may enhance particle attachment efficiency. This is achieved by allowing particles to roll and slide on the collector’s surface, ultimately accumulating near the separation line of the collector's boundary layer. This implies that an initial formation of biofilms on vegetation stems could provide enough adhesive force to capture particles. The gradual accumulation of particles could, in turn, facilitate further biofilm growth, enhancing the stems' ability to intercept additional particles.

Chapter 3 expanded the work in chapter two to a patch of vegetation, simulating particle attachment to groups of collectors in both regular and random arrangements, with varying vegetation densities. The study revealed that stem density and spatial arrangement significantly influence capturing efficiency across the patch. In particular, higher densities showed increased particle capture efficiency when computed as a patch averaged efficiency. The random arrangement, designed to mimic natural saltmarsh configurations, exhibited varied capture efficiency among individual collectors due to wake interactions and proximity effects, underscoring the importance of considering patch structure in restoration design. Unlike a single collector, when collectors are grouped, they can intercept particles more effectively on their rear sides. Our results indicate that this back-side capture efficiency increases with both vegetation density and Reynolds number.

Chapter 4 focused on the experimental study of fine sand winnowing from the interstices of immobile rough substrates, analogous to oyster beds or gravel beds supporting salmonid spawning grounds. This study established criteria for the hydrodynamic conditions necessary to entrain fine particles while leaving the larger substrate elements intact. The findings provide guidelines for designing flushing flows that can clear excessive sediment deposits without disrupting the structural integrity of essential habitats.

Suggestions for further research

Marine environments are highly complex, with numerous variables influencing particle transport, including variations in particle shapes and densities—from larvae to sediment particles. These particles interact significantly with their surroundings, attach to various substrates, and play a crucial role in restoration design. The application of Computational Fluid Dynamics (CFD) coupled with the Discrete Element Model (DEM) has led to substantial breakthroughs in understanding these processes in industrial settings and has recently gained momentum in studying particle aggregation and cohesive sediment transport in marine environments. Several enhancements could be made to the models presented in this thesis to improve particle capture predictions on vegetation. These recommendations are as follows:

- **Particle Shape and Density**: Microplastics, a major concern in marine pollution, exist in various shapes and densities that influence their movement and buoyancy. Saltmarshes and vegetative buffer zones have potential for trapping these particles, making it crucial to quantify their deposition and entrainment rates for accurate budget analysis and for designing bioretention sites to capture microplastics before they reach open waters. Microplastics can appear in different forms, including slender bodies, cylindrical shapes, and flexible fibers. Most current studies on particle capture focus on spherical particles, so it is essential to extend this research to quantify the attachment rates of particles with diverse shapes and behaviors.

- **Vegetation Branching and Biomass Influence**: Observations from field studies indicate that the biomass distribution of saltmarsh vegetation, especially branching, significantly impacts particle trapping efficiency. The vertical profile of vegetation due to branching could be further investigated using the CFD-DEM model. Field measurements by Li and Yang suggest that particle deposition is more prominent at branch joints than along the main stems, an area not yet explored in depth through numerical modeling or laboratory flume experiments. CFD-DEM with adhesive force modeling offers the potential to simulate how particles are drawn toward joints, interact with each other and the plant surfaces, and enhance deposition rates. Recirculation zones formed around joints may create low-velocity areas that promote particle attachment, providing a valuable insight into improving particle capture in restoration applications.

- **Flow unsteadiness due to waves**: An important application of research on particle attachment lies in biofouling on marine renewable energy structures like turbines and wave energy converters. These structures provide hard substrates that attract colonization by marine organisms, with wave-driven flow unsteadiness playing a key role in transporting particles or organisms into proximity and enhancing attachment. Studying particle capture under wavy flow conditions can improve biofouling estimates, and CFD-DEM models with adhesive forces can offer valuable insights. Additionally, wave-induced mixing influences particle attachment on natural collectors like saltmarsh stems and filter feeders such as bivalves, impacting ecosystem dynamics and sediment budgets.
- **Collector flexibility.** Vegetation stems naturally bend under flow, and this reconfiguration alters both the flow field and the drag force acting on them. Particle behavior near flexible stems is influenced by this mutual interaction, with stem curvature potentially affecting the trajectories, deposition, and attachment efficiency. Additionally, in submerged canopies like submerged aquatic vegetation (SAV), stem bending can create shear layers between the canopy and the free fluid region above, impacting particle movement within this shear layer. Using CFD-DEM modeling to

simulate these interactions can provide valuable insights into particle behavior in flexible canopies, enhancing our understanding of sediment and pollutant dynamics in marine ecosystems.

- **Higher resolution CFD models.** In this research, a two-equation turbulence model based on the Boussinesq hypothesis was employed. However, bluff body flows, such as those around groups of cylinders, are complex and often require higher-resolution models, such as Large Eddy Simulation (LES) or Direct Numerical Simulation (DNS), which can capture energetic eddies and finer flow details across varying time and length scales. At Reynolds numbers exceedingly approximately 190, three-dimensional flow structures start to appear in flow around a cylinder (Espinosa et al., 2012). For the CFD-DEM model in this study, only one cell was used in the lateral direction, while capturing true three-dimensionality would ideally require a lateral domain length at least twice the collector diameter. Although this simplification did not affect results for single-collector efficiency, it may have influenced findings for groups of collectors. This assumption could explain the discrepancies in drag coefficient values compared to the LES results of Stoesser et al. (2010) and Tanino (2008). Integrating LES or DNS in future studies could improve accuracy, especially for collective drag and capture efficiency analyses in denser patches.

Bibliography

Acornley, R.M. and Sear, D.A., 1999. Sediment transport and siltation of brown trout (Salmo trutta L.) spawning gravels in chalk streams. *Hydrological processes*, *13*(3), pp.447-458.

Arya, S.P.S., 1975. A drag partition theory for determining the large-scale roughness parameter and wind stress on the Arctic pack ice. *Journal of Geophysical Research*, *80*(24), pp.3447-3454.

Barbier, E.B., Hacker, S.D., Kennedy, C., Koch, E.W., Stier, A.C. and Silliman, B.R., 2011. The value of estuarine and coastal ecosystem services. *Ecological monographs*, *81*(2), pp.169-193.

Bathurst, J.C., 1985. Flow resistance estimation in mountain rivers. *Journal of Hydraulic Engineering*, *111*(4), pp.625-643.

Bayazit, M. and Denker, H., 1980. Stochastic Analysis of Bed-Load Motion in Very Rough Channels. In *Proceedings* (pp. 347-359).

Bayazit, M., 2020. Flow structure and sediment transport mechanics in steep channels. In *Mechanics of sediment transport* (pp. 197-206). CRC Press.

Bandyopadhyay, P.R., 1987. Rough-wall turbulent boundary layers in the transition regime. *Journal of Fluid Mechanics*, *180*, pp.231-266.

Brooks, H., Möller, I., Carr, S., Chirol, C., Christie, E., Evans, B., Spencer, K.L., Spencer, T. and Royse, K., 2021. Resistance of salt marsh substrates to near-instantaneous hydrodynamic forcing. *Earth Surface Processes and Landforms*, *46*(1), pp.67-88.

Callow, M.E. and Fletcher, R.L., 1994. The influence of low surface energy materials on bioadhesion—a review. *International biodeterioration & biodegradation*, *34*(3-4), pp.333-348.

Dey, S., 2014. *Fluvial hydrodynamics*.

Droppo, I.G., 2001. Rethinking what constitutes suspended sediment. *Hydrological processes*, *15*(9), pp.1551-1564.

Egiazaroff, I.V., 1965. Calculation of nonuniform sediment concentrations. *Journal of the Hydraulics Division*, *91*(4), pp.225-247.

Donatelli, C., Ganju, N.K., Kalra, T.S., Fagherazzi, S. and Leonardi, N., 2019. Changes in hydrodynamics and wave energy as a result of seagrass decline along the shoreline of a microtidal back-barrier estuary. *Adv. Water Resour*.

Elliott, A.H., 2000. Settling fine sediment in a channel with emergent vegetation. *Journal of Hydraulic Engineering*, *126*(8), pp.570-577.

Espinosa-Gayosso, A., Ghisalberti, M., Ivey, G.N. and Jones, N.L., 2012. Particle capture and low-Reynolds-number flow around a circular cylinder. *Journal of Fluid mechanics*, *710*, pp.362-378.

Espinosa-Gayosso, A., Ghisalberti, M., Ivey, G.N. and Jones, N.L., 2013. Particle capture by a circular cylinder in the vortex-shedding regime. *Journal of Fluid Mechanics*, *733*, pp.171-188.

Fagherazzi, S., Mariotti, G., Leonardi, N., Canestrelli, A., Nardin, W. and Kearney, W.S., 2020. Salt marsh dynamics in a period of accelerated sea level rise. *Journal of Geophysical Research: Earth Surface*, *125*(8), p.e2019JF005200.

Fernandez Luque, R. and Van Beek, R., 1976. Erosion and transport of bed-load sediment. *Journal of hydraulic research*, *14*(2), pp.127-144.

Fauria, K.E., Kerwin, R.E., Nover, D. and Schladow, S.G., 2015. Suspended particle capture by synthetic vegetation in a laboratory flume. *Water Resources Research*, *51*(11), pp.9112-9126.

Fleri, J.R., Lera, S., Gerevini, A., Staver, L. and Nardin, W., 2019. Empirical observations and numerical modelling of tides, channel morphology, and vegetative effects on accretion in a restored tidal marsh. *Earth Surface Processes and Landforms*, *44*(11), pp.2223-2235.

Fredsoe, J. and Sumer, B.M., 2006. *Hydrodynamics around cylindrical structures (revised edition)* (Vol. 26). World Scientific.

Friedrichs, C.T. and Perry, J.E., 2001. Tidal salt marsh morphodynamics: a synthesis. *Journal of Coastal Research*, pp.7-37.

Garcia, M. and Parker, G., 1991. Entrainment of bed sediment into suspension. *Journal of Hydraulic Engineering*, *117*(4), pp.414-435.

Grams, P.E. and Wilcock, P.R., 2007. Equilibrium entrainment of fine sediment over a coarse immobile bed. *Water Resources Research*, *43*(10).

Giuliani, S. and Bellucci, L.G., 2019. Salt marshes: their role in our society and threats posed to their existence. In *World seas: An environmental evaluation* (pp. 79-101). Academic Press.

Iversen, J.D., Wang, W.P., Rasmussen, K.R., Mikkelsen, H.E., Hasiuk, J.F. and Leach, R.N., 1990. The effect of a roughness element on local saltation transport. *Journal of Wind Engineering and Industrial Aerodynamics*, *36*, pp.845-854.

Haugen, N.E.L. and Kragset, S., 2010. Particle impaction on a cylinder in a crossflow as function of Stokes and Reynolds numbers. *Journal of Fluid Mechanics*, *661*, pp.239-261.

Henderson, R.D., 1995. Details of the drag curve near the onset of vortex shedding. *Physics of Fluids*, *7*(9), pp.2102-2104.

Henry, C., Minier, J.P. and Lefèvre, G., 2012. Towards a description of particulate fouling: From single particle deposition to clogging. *Advances in colloid and interface science*, *185*, pp.34-76.

Henry, C. and Minier, J.P., 2014. Progress in particle resuspension from rough surfaces by turbulent flows. *Progress in Energy and Combustion Science*, *45*, pp.1-53.

Henry, C., 2017. Surface forces and their application to particle deposition and resuspension. *Particles in Wall-Bounded Turbulent Flows: Deposition, Re-Suspension and Agglomeration*, pp.209-261.

Johnson, K.L., Kendall, K. and Roberts, A., 1971. Surface energy and the contact of elastic solids. *Proceedings of the royal society of London. A. mathematical and physical sciences*, *324*(1558), pp.301-313.

Karim, M. F., Holly, F. M., and Kennedy, J. F., "Bed Armoring Procedures in IALLUVIAL and Application to the Missouri River," Iowa Institute of Hydraulic Research, Report No. 269, The Univ. of Iowa, Iowa City, Iowa, Dec, 1983.

Kleinhans, M.G. and Van Rijn, L.C., 2002. Stochastic prediction of sediment transport in sand-gravel bed rivers. *Journal of hydraulic engineering*, *128*(4), pp.412-425.

Kuhnle, R.A., Wren, D.G., Langendoen, E.J. and Rigby, J.R., 2013. Sand transport over an immobile gravel substrate. *Journal of Hydraulic Engineering*, *139*(2), pp.167-176.

Kuhnle, R.A., Wren, D.G. and Langendoen, E.J., 2016. Erosion of sand from a gravel bed. *Journal of Hydraulic Engineering*, *142*(2), p.04015052.

Li, H. and Yang, S.L., 2009. Trapping effect of tidal marsh vegetation on suspended sediment, Yangtze Delta. *Journal of coastal research*, *25*(4), pp.915-924.

Lei, J. and Nepf, H., 2019. Blade dynamics in combining waves and current. *Journal of Fluids and Structures*, *87*, pp.137-149.

Li, S.Q. and Marshall, J.S., 2007. Discrete element simulation of micro-particle deposition on a cylindrical fiber in an array. *Journal of Aerosol Science*, *38*(10), pp.1031-1046.

Leonardson, R., 2011. *Exchange off fine sediments with gravel riverbeds*. University of California, Berkeley.

Leonardi, S. and Castro, I.P., 2010. Channel flow over large cube roughness: a direct numerical simulation study. *Journal of Fluid Mechanics*, *651*, pp.519-539.

Lyles, L., Schrandt, R.L. and Schmeidler, N.F., 1974. How aerodynamic roughness elements control sand movement. *TRANSACTIONS of the ASAE*, *17*(1), pp.134-0139.

McIlwraith, H.K., Lindeque, P.K., Miliou, A., Tolhurst, T.J. and Cole, M., 2024. Microplastic shape influences fate in vegetated wetlands. *Environmental Pollution*, *345*, p.123492.

Meyer-Peter, E., 1948. Mu® eller, R., 1948. Formulas for bedload transport. In *Proc. IAHS Symp.'Erosion and sediment transport measurements', IAHS Publ* (No. 133).

McSherry, R., Zampiron, A., Marusic, I. and Falconer, R.A., 2019. Friction factor decomposition for rough-wall flows: theoretical background and application to open-channel flows. *Journal of Fluid Mechanics*, *872*, pp.626-664.

Michaelides, E.E., Sommerfeld, M. and van Wachem, B., 2022. *Multiphase flows with droplets and particles*. CRC Press.

Morris, J.T., Sundareshwar, P.V., Nietch, C.T., Kjerfve, B. and Cahoon, D.R., 2002. Responses of coastal wetlands to rising sea level. *Ecology*, *83*(10), pp.2869-2877.

Morris, R.L., Konlechner, T.M., Ghisalberti, M. and Swearer, S.E., 2018. From grey to green: Efficacy of eco-engineering solutions for nature-based coastal defence. *Global change biology*, *24*(5), pp.1827-1842.

Mudd, S.M., D'Alpaos, A. and Morris, J.T., 2010. How does vegetation affect sedimentation on tidal marshes? Investigating particle capture and hydrodynamic controls on biologically mediated sedimentation. *Journal of Geophysical Research: Earth Surface*, *115*(F3).

Mudd, S.M., Fagherazzi, S., Morris, J.T. and Furbish, D.J., 2004. Flow, sedimentation, and biomass production on a vegetated salt marsh in South Carolina: toward a predictive model of marsh morphologic and ecologic evolution. *The ecogeomorphology of tidal marshes*, *59*, pp.165-188.

Nikora, V., Goring, D., McEwan, I. and Griffiths, G., 2001. Spatially averaged open-channel flow over rough bed. *Journal of Hydraulic engineering*, *127*(2), pp.123-133.

Nikora, V., McEwan, I., McLean, S., Coleman, S., Pokrajac, D. and Walters, R., 2007. Double-averaging concept for rough-bed open-channel and overland flows: Theoretical background. *Journal of Hydraulic Engineering*, *133*(8), pp.873-883.

Noe, G.B., Harvey, J.W. and Saiers, J.E., 2007. Characterization of suspended particles in Everglades wetlands. *Limnology and Oceanography*, *52*(3), pp.1166-1178.

Palmer, M.R., Nepf, H.M., Pettersson, T.J. and Ackerman, J.D., 2004. Observations of particle capture on a cylindrical collector: Implications for particle accumulation and removal in aquatic systems. *Limnology and Oceanography*, *49*(1), pp.76-85.

Parker, G., Klingeman, P.C. and McLean, D.G., 1982. Bedload and size distribution in paved gravel-bed streams. *Journal of the Hydraulics Division*, *108*(4), pp.544-571.

Parker, G., 2008. Transport of gravel and sediment mixtures. *Sedimentation engineering*, pp.165-251.

Purich, A., 2006. The capture of suspended particles by aquatic vegetation. *University of Western Australia*, pp.1-97.

Raupach, M., 1992. Drag and drag partition on rough surfaces. *Boundary-Layer Meteorology*, *60*(4), pp.375-395.

Raupach, M.R., Gillette, D.A. and Leys, J.F., 1993. The effect of roughness elements on wind erosion threshold. *Journal of Geophysical Research: Atmospheres*, *98*(D2), pp.3023-3029.

Shvidchenko, A.B. and Pender, G., 2000. Flume study of the effect of relative depth on the incipient motion of coarse uniform sediments. *Water Resources Research*, *36*(2), pp.619-628.

Shao, Y. and Yang, Y., 2005. A scheme for drag partition over rough surfaces. *Atmospheric Environment*, *39*(38), pp.7351-7361.

Stradiotti, G., Righetti, M., Tarekegn, T.H., Wharton, G. and Toffolon, M., 2020. New Conceptual Framework for the Erosion of Fine Sediment from a Gravel Matrix Based on Experimental Analysis. *Journal of Hydraulic Engineering*, *146*(9), p04020061.

Stumpf, R.P., 1983. The process of sedimentation on the surface of a salt marsh. *Estuarine, Coastal and Shelf Science*, *17*(5), pp.495-508.

Takeda, Y., 1995. Velocity profile measurement by ultrasonic Doppler method. *Experimental thermal and fluid science*, *10*(4), pp.444-453.

Tritton, D.J., 1959. Experiments on the flow past a circular cylinder at low Reynolds numbers. *Journal of Fluid Mechanics*, *6*(4), pp.547-567.

Wen, C.Y., Yeh, C.L., Wang, M.J. and Lin, C.Y., 2004. On the drag of two-dimensional flow about a circular cylinder. *Physics of Fluids*, *16*(10), pp.3828-3831.

Wilcock, P.R. and Kenworthy, S.T., 2002. A two-fraction model for the transport of sand/gravel mixtures. *Water Resources Research*, *38*(10), pp.12-1.

Wilcock, P. and Crowe, J.C., 2003. A surface-based transport model for sand and gravel. *Hydraulic Engineering*, *129*(2), p.120.

Wood, P.J. and Armitage, P.D., 1997. Biological effects of fine sediment in the lotic environment. *Environmental management*, *21*(2), pp.203-217.

Wooding, R.A., Bradley, E.F. and Marshall, J.K., 1973. Drag due to regular arrays of roughness elements of varying geometry. *Boundary-Layer Meteorology*, *5*(3), pp.285-308.

Wren, D.G., Kuhnle, R.A., Langendoen, E.J. and Rigby, J.R., 2014. Turbulent flow and sand transport over a cobble bed in a laboratory flume. *Journal of Hydraulic Engineering*, *140*(4), p.04014001.

Wu, S., Christensen, K.T. and Pantano, C., 2020. A study of wall shear stress in turbulent channel flow with hemispherical roughness. *Journal of Fluid Mechanics*, *885*.

Yager, E.M., Kirchner, J.W. and Dietrich, W.E., 2007. Calculating bed load transport in steep boulder bed channels. *Water Resources Research*, *43*(7).

Yu, M., Yu, X. and Balachandar, S., 2022. Particle nonresolved DNS-DEM study of flocculation dynamics of cohesive sediment in homogeneous isotropic turbulence. *Water Resources Research*, *58*(6), p. e2021WR030402.